Investigation of damage detection methods for laminated composite materials using full field digital image correlation

By: Crown James Qambela

A dissertation submitted in partial fulfillment of the requirements of the degree

Master of Engineering

In the Department of Mechanical and Aeronautical Engineering

Faculty of Engineering, the Built Environment and Information Technology

University of Pretoria

2020

Investigation of damage detection methods for laminated composite materials using full field digital image correlation

Author: Crown James Qambela
Supervisor: Prof P.S. Heyns and Dr H.M. Inglis
Department: Department of Mechanical and Aeronautical Engineering
Degree: Master of Engineering

Abstract

The aeronautical industry is among many which have focused on material with a high strength to weight ratios in order to accomplish as much efficiency as possible during flight. Among material of high strength to weight ratios are composite materials (Matthews and Rawlings, 1999).

A composite material is defined by Lee (1989) as the combination of two or more materials of different characteristics (composition or form) which remain bonded together. This yields a material which essentially has all the beneficial attributes of its parent materials and little of their shortcomings. In the aeronautical field composite materials are used to construct components such as airplane wings spoilers and panels, vertical and horizontal stabilizers etc. (Baker et al., 2004).

The wide use and range of composites has led to the development of various techniques for damage detection. One of the common types of damage which composites experience is barely visible impact damage, which can be caused by dropped objects during construction or maintenance. Laminated composites, unlike isotropic materials such as steel, show essentially no yielding prior to complete failure. This makes it crucial to assess them for damage before use.

This research presents an investigation into the possibility of damage detection in laminated composites by making use of full field digital image correlation (DIC). The technique is often employed to assess the structural deformation characteristics of components under various loading conditions, which can then be correlated with finite element assessments. In this research three experimental methods are explored in terms of their performance in detecting barely visible impact damage: 1) modal analysis, 2) full field DIC under static loading, 3) full field DIC under dynamic loading. Modal analysis results showed no noticeable shifts in natural frequencies between an undamaged and damaged carbon/epoxy woven laminated composite, when damage was induced via static point load application at the center of the specimen.

Full field DIC under dynamic loading namely, drop impact tests designed to induce no addition damage, revealed no change in peak out-of-plane displacements between an undamaged and damaged specimen. The technique proved effective only when severe visible damage was induced, which falls out of the scope of the research.

Prior to full field DIC testing under static loading a number of experimental exercises were performed to check the accuracy of the method when measuring rigid body motion and out-of-plane displacements. The acquired results were compared to independent measurements obtained using a micrometer for rigid body motion and an eddy current probe for out-of-plane displacements.

The method of full field DIC under static loading condition showed significant reduction in stiffness between the undamaged and damaged composite, with increases in out-of-plane peak displacement and von Mises strain fields. The success of full field DIC under static loading paved the way forward for the investigation of damage detection in laminated composites under various impact energies (i.e. centered impact and off-center impact) resulting in barely visible impact damage.

The finding revealed an increase in compliance of the impacted laminated composite due to the damage. The barely visible damage can be detected using full field DIC only when the loading or excitation is located around the damaged region. There was no noticeable change in out-of-plane displacement fields of the specimens that were subjected to centered impact and off-center impact. Significant changes in von Mises strain fields exist between the undamaged and damaged laminated composites with centered impact.

Acknowledgements

I would like to give thanks to the following individuals and organization for the tireless efforts in assisting towards the completion of this dissertation:

Supervisors: Prof Heyns and Dr Inglis for the guidance and motivation in carrying out acceptable experimental work and documentation.

Denel Aeronautics and the THRIP program for funding the research.

The Sasol labs: George Breitenbach, Dr Abrie Oberholster, Johann Clarke and Herman Booysen for tireless assistance in experimentations, experimental setups and entrusting me with lab equipment.

TANDM: For training in MSC Marc and Mentat basic nonlinear finite element analysis

Table of Contents

Abstract ii

Acknowledgements iv

Nomenclature viii

Chapter 1: Introduction and literature review 1

1.1 Introduction 1

1.2 Literature review 2

1.2.1 Laminated composites 2

1.2.2 Damage in laminated composite 3

1.2.3 Commonly used damage detection techniques 11

1.2.4 Research based experimental techniques 12

1.3 Conclusion to literature review 20

1.4 Project plan and flow diagram 21

1.5 Project contribution 23

1.6 Overview of preliminary experiments for damage detection in laminated composites 24

1.7 Description of laminated composites for preliminary experiments 25

Chapter 2: Preliminary investigation of the capabilities of experimental modal analysis for damage detection in laminated composites 26

2.1 Theory of modal analysis 26

2.2 Experimental setup for contact modal analysis 27

2.3 Experimental setup for non-contact modal analysis 28

2.4 Contact modal analysis results of undamaged composite 29

2.5 Non-contact modal analysis results of undamaged composite 31

2.6 Comparison of undamaged and damaged composite modal results 33

Chapter 3: Theory and evaluation of full field DIC 34

3.1 The theory of full field DIC 34

3.1.1 Photogrammetry 34

3.1.2 Stereo imaging 37

3.1.4 Principles of DIC 38

3.1.5 Full field DIC arrangement 40

3.2 Procedure of the ARAMIS GOM DIC system camera calibration 42

3.3 DIC rigid body motion experimental setup and camera calibration 44

3.4 Results of full field DIC and micrometer for rigid body motion accuracy tests 46
3.5 Full field DIC out-of-plane displacement experimental setup and calibration: comparison with eddy current probe 49
3.5.1 Theory of eddy current probe 49
3.5.2 Calibration of the eddy current probe 49
3.6 Results of full field DIC and eddy current probe for out-of-plane deformation accuracy tests 52
Chapter 4: Preliminary investigation of full field DIC for damage detection in laminated composites 54
4.1 Full field DIC experimental setup for static loading conditions 54
4.2 Calibration of the 200 kg load cell 55
4.3 Results of full field DIC damage detection in laminated composites under static loading 56
4.3.1 Results of damage detection for loads applied via 30mm spherical ball 57
4.3.2 Results of damage detection for load applied via 24 mm rounded piston 59
4.4 Full field DIC experimental setup and camera calibration for damage detection in laminated composites under dynamic loading 61
4.5 Results of full field DIC damage detection in laminated composites under dynamic loading 63
4.6 Discussion of Preliminary investigations of damage detection in laminated composites using experimental modal analysis and full field DIC 67
Chapter 5: Barely visible impact damage detection in laminated composites using full field DIC under static loading conditions 68
5.1 Overview 68
5.2 Description of laminated composites 69
5.3 Plan for the experiments 70
5.4 Experimental setup for drop impact tests and full field DIC 70
5.4.1 Drop impact test apparatus 70
5.4.2 Experimental setup for full field DIC 71
5.5 Experimental results of damage detection in laminated composites using full field DIC under static loading 72
5.5.1 Variations in full field DIC measurements between repeated test, recalibrating of the cameras and dismantling of the specimens. 73
5.5.2 Full field DIC results of laminated composites subjected to centered impact 75

5.5.3 Full field DIC of laminated composites subjected to off-centered impact 80
Chapter 6: Conclusions and recommendations 83
6.1 Conclusions 83
6.2 Future work and recommendations 83
References 85
Appendices 89

Nomenclature

Abbreviations	Descriptions
FEA	Finite Element Analysis
FEM	Finite Element Model
CAI	Compression After Impact
TAI	Tension After Impact
PMC	Polymer Matrix Composite
EMA	Experimental Modal Analysis
FE	Finite Element
FOSM	First Order Second Moment
FRF	Frequency Response Function
IRS	Improved Reduced System
µs	Microsecond
FPF	First Ply Failure
LPF	Last Ply Failure
NDT	Non Destructive Testing
BVID	Barely Visible Impact Damage
BVD	Barely Visible Damage
m/s	Meters per second
NDUI	Non Destructive Ultrasonic Image
E	Young's modulus
J	Joule
kg	Kilogram
DIC	Digital Image Correlation
N	Newton
V	Volt

Chapter 1: Introduction and literature review

1.1 Introduction

Laminated composite materials have become very popular in many industries such as the aeronautical and automotive sectors due to their high strength to weight ratio. Laminated composites have a complex composition which often present a challenge in examining them for underlying damage which unlike metal give very little warning before complete failure. This makes structural monitoring techniques with the ability to detect delamination, fiber and matrix failure important when it comes to laminated composites.

There is a lot of research in mechanical engineering focused on methods of detecting damage in mechanical components. Damage alters the mechanical behaviour of manufactured parts by compromising either the stiffness or mass of the component. This change presents an opportunity to use a variety of methods to detect the damage by evaluating the response of the subject to experimental disturbances.

This research focuses on damage in laminated composite materials. Of primary focus is Barely Visible Impact Damage (BVID) which is commonly encountered in laminated composites. This type of damage results in cracks within the matrix which serves to hold the fibers together and transmit forces throughout the material. Failure of the fibers can also occur when the impact energy is severe enough. BVID in a sense is a ticking time bomb, it slowly degrades the material's ability to carry the stresses for which it was designed for as the cracks in the matrix propagate. The best means thus far to deal with BVID is to detect it and examine the remaining strength, and to design for full replacement before complete failure which like glass occurs without warning.

This research explores as a first step various techniques based on available equipment to try and detect barely visible damage in laminated composites. The results from this first step informed the decision of the most effective technique for further experimentation. The methods explored are modal analysis, full field Digital Image Correlation (DIC) under dynamic and static loading conditions. The results of interest in modal analysis are noticeable shifts in the natural frequency values as a result of barely visible damage. Of interest from the full field DIC results are changes in out-of-plane displacements, von Mises strain fields and loss of stiffness due to the damage.

The literature study looks into laminated composites of different constituents and how their composition affects their mechanical properties and overall strength. It describes the different types of damage mechanisms they exhibit under various loading conditions. In the literature study common methods that are used for damage detection are discussed along with research based experimental techniques.

Included in a separate section (section 3.1) is literature on the theory full field DIC, and how it has been implemented to examine deformation data so as to inform the approach of data capturing for this research.

1.2 Literature review

In the literature review the variety, manufacturing and application of laminated composites are discussed. The literature gives insight of what laminated composites are, how their composition and changes in their composition (i.e. damage) affect their mechanical behaviour. The literature covers various damage mechanisms and techniques that have been used to detect damage in laminated composites. This includes common practices and researched based methods.

1.2.1 Laminated composites

A composite describes any material that consists of two or more constituents bounded together to function as a single component. Laminated composites have two major components i.e. the matrix and the reinforcements. The matrix in many cases is formed from epoxy resin and serves as an adhesive (Figure 1). The reinforcements are the fibers of materials such as carbon or glass. Laminated composites can be produced by hand layup or automatic fiber placement (Jareteg et al., 2014). When the composite is manufactured by hand the fibers are laid up in the desired orientation and liquid resin is added to surround the fibers and spaces between them. The mixture is then left to cure and harden forming the composite. Laminated composite manufacturing by automatic fiber placement uses fabrics which have been pre-impregnated with resin knows as prepreg fabrics or plies. The application of heat and pressure bind the fabrics together.

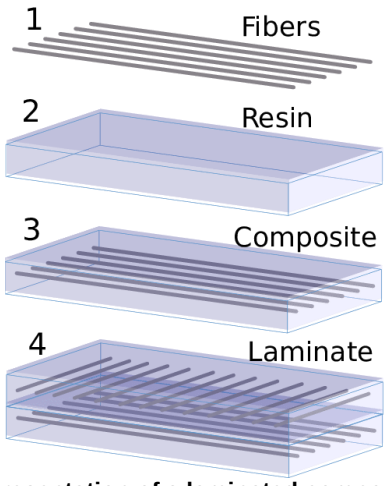

Figure 1: Schematic representation of a laminated composite (Jareteg et al., 2014)

Laminated composites have over the years acquired recognition for their mechanical performance. Today they can be found in many industries such the automotive, aeronautical and aerospace industries. Their popularity is because of their high strength to weight ratios, and their high stiffness to weight ratios (Park et al., 2001). A distinctive characteristic of laminated composites is that their stiffness can be augmented by manipulating the number of layers (i.e. plies), and the manner in which their fibers are orientated in each ply. Two types of plies which are commonly used in the automotive and aeronautical industries are unidirectional plies and woven fabric plies.

In a unidirectional ply all the fibers are orientated in the same direction (Figure 2(b)), whereas in a woven fabric the fibers are interlaced with one another (Figure 2(b)).

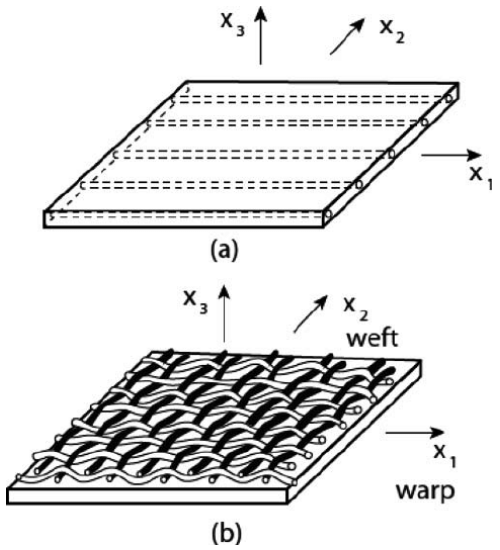

Figure 2: Orthotropic plies (a) shows a unidirectional ply, (b) shows a woven fabric ply (Carlsson et al., 2013)

A ply unit whether unidirectional or woven fabric is orthotropic in nature. Unidirectional plies bear high strength and stiffness in the direction of the fiber, and lower strength in the other directions. Woven fabric plies are more balanced bearing similar strength and stiffness in warp and weft directions (Figure 2), and only weak in strength in the through thickness direction. Laminated composites of different strength can be achieved by the addition of plies stacked with their fibers facing in different directions. Research has been done looking into the effects of the stacking sequence for various loading conditions. In the end it comes down to how strong the laminate is required to be in order to overcome the loading circumstance in question. Shabeer and Murtaza (2013) showed that an adequate balance in mechanical performance can be attained from a stacking sequence of $[0^0/90^0/+45^0/-45^0/90^0/0^0]$ (i.e. cross-ply arrangement).

1.2.2 Damage in laminated composite

Manufacturing defects

There are flaws which are introduced in composite materials during the manufacturing process which are later identified as the root cause of premature structural failure. The most common manufacturing error is the presence of voids in the matrix called porosity. The investigation of voids in the matrix of laminated composites started years ago and is still a field of active research due to the amount of unknowns about voids. There are difficulties in eliminating their formation in modern manufacturing methods due to types of resins and curing processes. The development and evolution of voids tends to differ in manufacturing processes. Among the manufacturing process of Liquid Composite Moulding (LCM), the most well know and commonly used are Resin Transfer Moulding (RTM) and Vacuum Assisted Resin Transfer Moulding (VARTM). In the manufacturing process of Liquid Transfer Moulding the composite is formed by liquid resin infiltration into the fibrous fabrics, the voids are formed when air becomes entrapped during resin flow or by the gases created from chemical reactions during curing (Mehdikhani et al., 2019).

In prepeg manufacturing techniques such as autoclave curing the source of the voids in prepeg fabrics is air entrapment during the impregnation stage (intra-lamina voids), or air entrapment during the layup stage (inter-lamina voids). Figure 3 shows porosity in the matrix caused by poorly established curing parameters and poor quality control which lead to inclusions of foreign bodies in the matrix (Ghobadi, 2017).

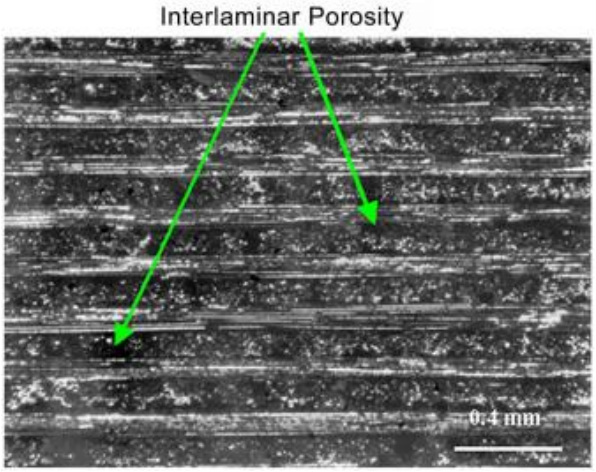

Figure 3: Porosity in laminate composite (Ghobadi, 2017)

Fatigue damage

The literature below looks into the damage mechanisms and behaviour of laminated composites under cyclic loading conditions.

The failure in laminated composites under service loading occurs as a result of a complex blend of damage modes and mechanisms. The damage controls the strength and stress the laminate can endure. Reifsnider and Talug (1980) proposed a philosophy on the nature of damage development under cyclic loading in laminated composites. The proposed philosophy is based on what is called a “characteristic damaged state” which is determined by the properties of the laminated composite. The properties include the orientation of the plies and ply stacking sequence rather than the load history. Their investigation showed that in angled ply laminated composites subjected to quasi-static loading, the first incident of degradation appears as the formation of a crack in fiber direction. This is the direction that lies in the plane that is perpendicular to the load axis. Under cyclic tension loading their work demonstrated that the number of crack in the plane perpendicular to the cyclic load increased with increasing number of cycles in angled ply laminates. It can be said that the deterioration of mechanical properties of laminated composites under cyclic loading can occur in a number of damage mechanism: matrix cracking, delamination, fiber cracking, and transverse ply cracking. The damage mechanisms can either occur simultaneously or independently during fatigue loading (Harris, 2003).

Fatigue damage mechanism in composites is complex due to the anisotropic property of the material. Thermoset composite materials, when subjected to cyclic loading tend to exhibit higher tensile resistance than compression resistance (Jollivet et al .2013). In the world of metals, fatigue can be divided into three phases: crack initiation, crack propagation and final failure (i.e. separation of the component into two or more parts).

In composites however the damage process is completely different due to the heterogeneity of the material brought about by the difference in mechanical properties of the matrix and the reinforcements. In composite materials the fatigue strength is influenced by the material's anisotropy.

An increase in anisotropy leads to a decrease in fatigue strength. The fatigue damage that manifests on the surface as well as in the bulk of the composite not only depends of the type of cyclic loading, but on the anisotropy of the material.

The fatigue damage process in composites can be classified into two phases: the 1st phase of damage occurring at low strength areas such as the matrix and the interface between the matrix and the fibers. The 2nd and final phase is fiber breakage under high cycle loading. Matrix failure is indicated by intra-laminar cracks (Figure 4(b)) which form in areas where the fibers are not oriented in the axis of the load. This kind of damage has minimal effect on the ultimate strength of the material. When the volume of these intra-laminar cracks increases beyond a certain level, the second stage of damage called translaminar failure commences (Figure 4(c)). This damage focus on areas where the axis of the stress and the orientation of the fibers coincide. In addition to intra-laminar damage in the matrix, inter-laminar (i.e. delamination) occurs in laminated composites (Figure 4(a)). In the opening mode of crack propagation the damage in the matrix grows by forming microscopic river like features (Figure 5(a)), while cusps form in the shearing mode (Figure 5(b)).

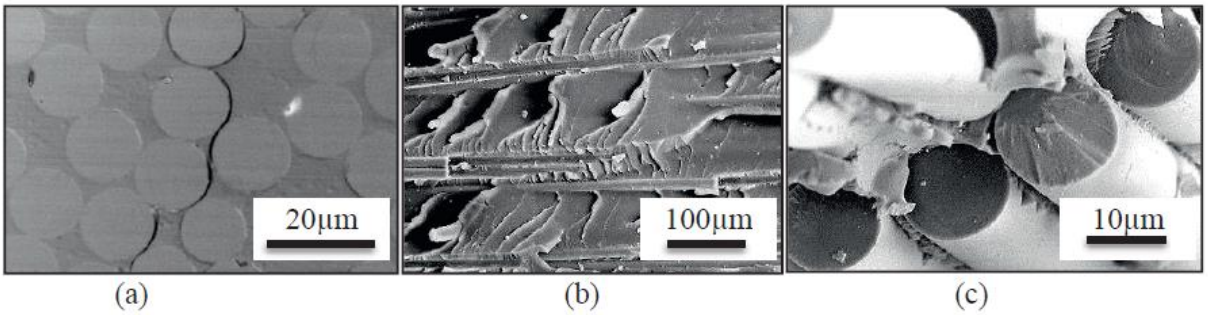

Figure 4: (a) Inter-laminar failure (b) Intra-laminar failure (c) Translaminar failure (Jollivet et al., 2013)

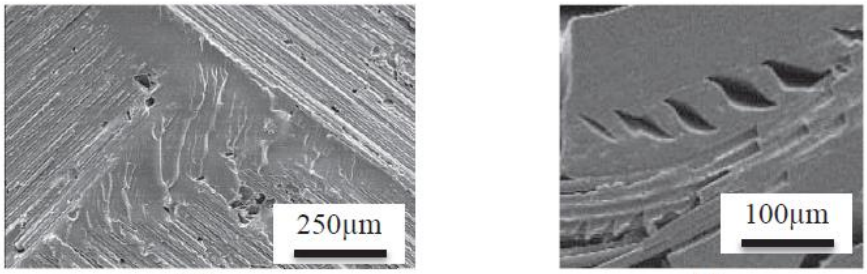

Figure 5: (a) Formation of rivers in the opening mode (b) Formation of cusps in the shearing mode (Jollivet et al., 2013)

There is research looking into the development of the theory of fatigue failure in laminated composites. The intent is to develop reliable mathematical models of predicting service life based on the concepts of solid mechanics (Revuelta and Miravete, 2002), and transverse cracking under fatigue loading (Thionnet and Renard, 1994). From the theory of fatigue for solid mechanics it was discovered that laminated composites that are loaded in an interrupted fatigue pattern (i.e. irregular loading profile) sustained significantly more cycles before failure compared to the laminates subjected to continuous cyclic loading at high and low stress levels (Movahedi-Rad et al., 2018).Their rectangular angled ply glass/epoxy laminated specimens were subject to cyclic tensile loading in both cases, the effect was more significant at higher stress levels with an average lifetime increase of about 126%.

Impact damage

Impact analysis on metallic materials is well documented in the literature. In composites however the effects of impact manifests in a complex fashion owing to the composition of the material. Of particular interest is low velocity impact damage, which tends to be barely visible and raises maintenance concerns. Impact damage has been shown to be dependent on the number of plies used in the laminate (i.e. thickness), and the impact energy (Murat and Rahman, 2017). The greater the impact energy the greater the damage, the thicker the laminate the more resistant it is to impact damage. It has been found through impact and compression testing that the predominant mechanism of failure in woven laminated composites was fiber breakage and delamination (Siow et al., 1997)

It is important to understanding how impact damage changes the mechanical behaviour of composite materials, and how their composition affects their tolerance to impact energy. The work of Malhotra and Guild (2014) documented the effects of impact loading on composite laminates at different locations of the laminated specimens. Their investigation comparing the damage tolerance when the impact energy was localized at the center, near-edge, on-edge position of the composite, as well as the effects of laminate thickness on the damage tolerance.

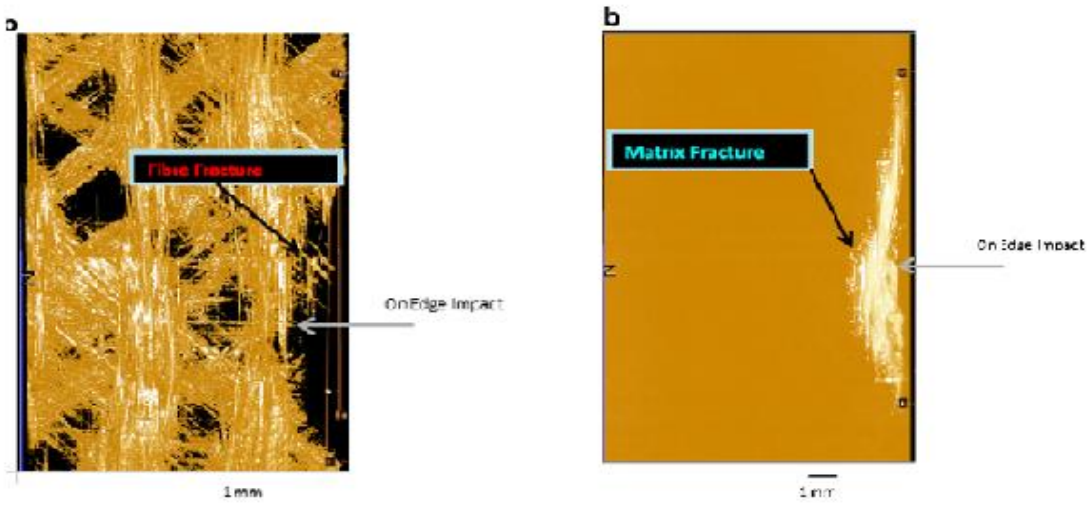

Figure 6: Fiber and matrix damage on 2 mm laminate at 4 J (Malhotra and Guild, 2014)

In their experiment, quasi-isotropic glass fiber cloth cotech EQX 1034 style 3200, non-crimped fibers and non-stitched lay-up were examined. Laminate curing time after impregnation was completed in two stages: first stage for 24 hours at room temperature and the second stage at 80 degrees Celsius for 7 hours. A ply thickness of 0.25 mm was used to form 2 mm and 4 mm thick laminates. The impact tests were carried out using a CEATIS Dartvis 6790 drop-weight impact testing apparatus. Figure 6 shows the X-Ray computed tomography images of the extent of fiber and matrix damage for on-edge impact on the 2mm thick laminate after 4 J of impact.

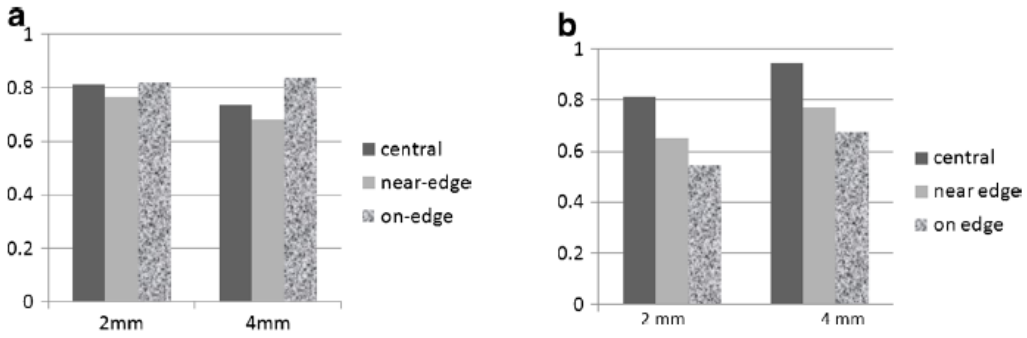

Figure 7: Effects of impact location in the (a) CAI and (b) TAI (Malhotra and Guild, 2014)

Compression After Impact test (CAI) and Tension After Impact test (TAI) results (Figure 7) revealed that the thicker laminate possessed low damage tolerance in compression, but a higher damage tolerance in tension. The thickness has very little effect on the damage tolerance for on edge impact in the CAI. At high energy impact, low damage tolerances were recorded for all three impact test positions. At both low and high impact energies the damage tolerances for the TAI were similar for all three impact test positions. A low damage tolerance is evident in the CAI test at near edge impact, high for on edge impact and significantly higher for central impact on thinner laminate (Figure 7).

The TAI on edge impact test results show low damage tolerance and high damage tolerance for central impact. The TAI shows that the damage tolerance becomes higher with increase in thickness.

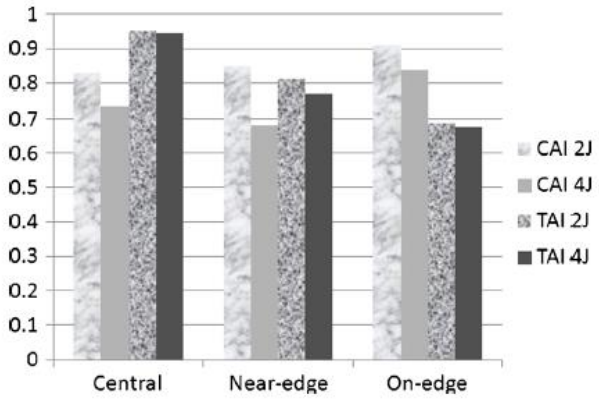

Figure 8: Effects of Impact energy in the CAI and TAI tests (Malhotra and Guild, 2014)

Tuo et al. (2019) looked into the impact resistance and damage tolerance of 2 mm thick carbon/epoxy laminated composites. They subjected their specimens to varying impact energies using an Instron impact test machine. They evaluated their tolerance by subjecting the specimens to compression tests after impact (CAI). Their C–scan results after impact showed that delamination and matrix damage were the prevailing damage modes in all their specimens (Figure 9), the size of delamination area increased with increasing impact energy.

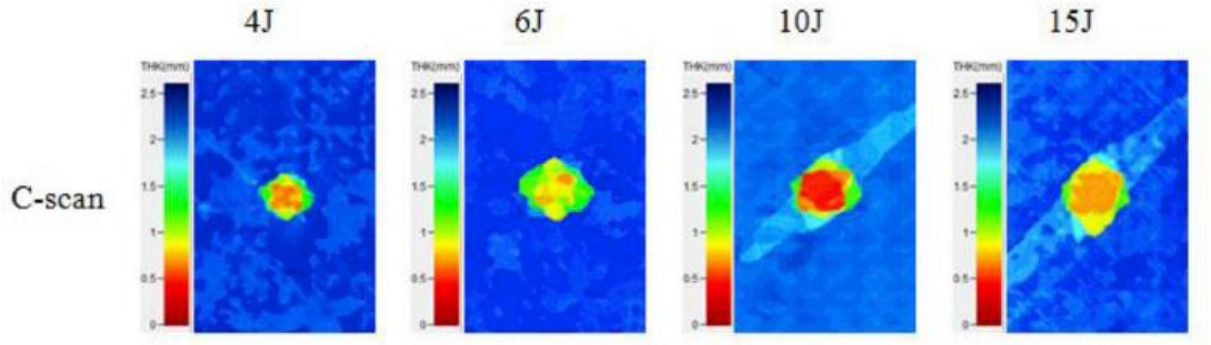

Figure 9: C-scan results showing delamination shape and size for varying impact energies (Tuo et al., 2019)

Their compression after impact tests revealed that the compressive resistance of all the specimens decreased with increasing impact energy. This was due to the fiber damage incurred after high energy impact, a significant reduction in compression after impact strength was observed (Figure 10).

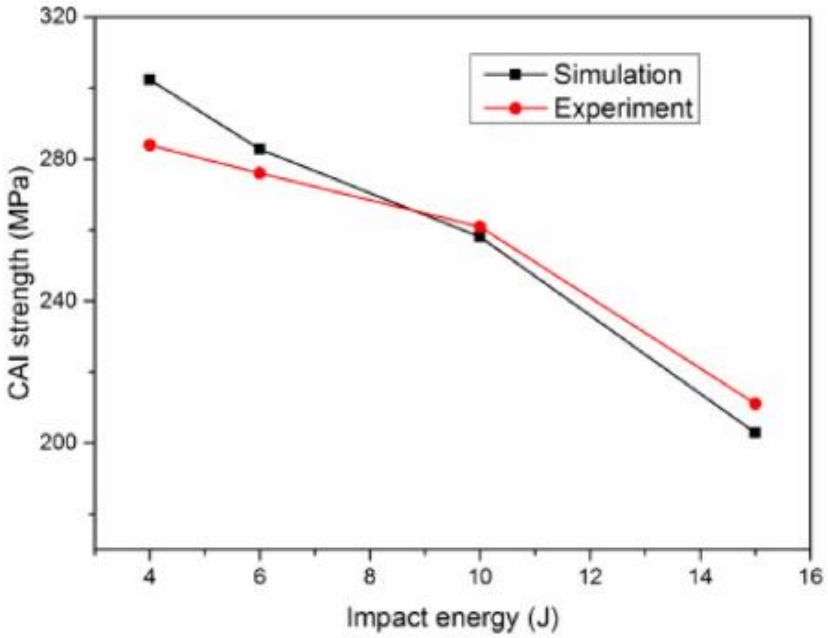

Figure 10: CAI strength results at various energies (Tuo et al., 2019)

A full field DIC system was also applied in the work of Tuo et al. (2019). Specimens were subjected to various impact energies using an Instron Dynatup 9250HV impact test machine. The laminated specimens were subjected to compressive loading using an instron 8803 test machine after the impact. Their out of plane distribution and strain fields of the impacted regions were observed using DIC. Their results showed for all impact energies that the local out-of-plane displacement started at the impacted region and became more pronounced with increasing load until complete failure along the transverse section occurred as a result of global buckling. The DIC strain fields in the x and y direction demonstrated similar results. Their work demonstrated that DIC can capture damage behaviour under progressive loading, however no comparison in behaviour with the undamaged specimens was done. Their work was focused on laminated composites of the same lay-up of (45º/0º/-45º/90º/45º/-45º/90º/0 º). The strength and mechanical behaviour of laminated composites are influenced by the ply lay-up. Sanchez-Saez et al. (2005) investigated the compression after impact strength of carbon/epoxy laminated composite of different lay-ups (i.e. quasi-isotropic, cross-ply and woven). The woven and the cross-ply laminates were 2.2 mm thick and the quasi-isotropic laminate was 1.6 mm thick. The C-scan results (Figure 11) revealed that the damage areas of the quasi-isotropic and cross-ply laminates were larger than the woven laminates.

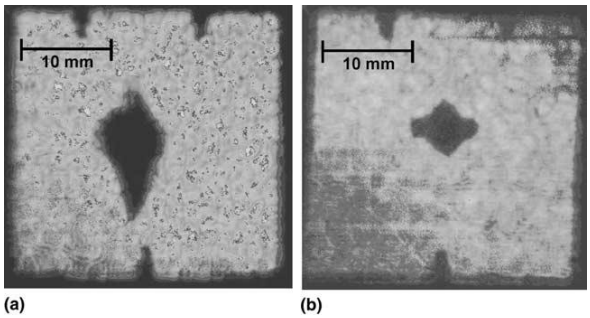

Figure 11: C-scan images after 4J of impact: (a) cross-ply laminate, (b) woven laminate (Sanchez-Saez et al., 2005)

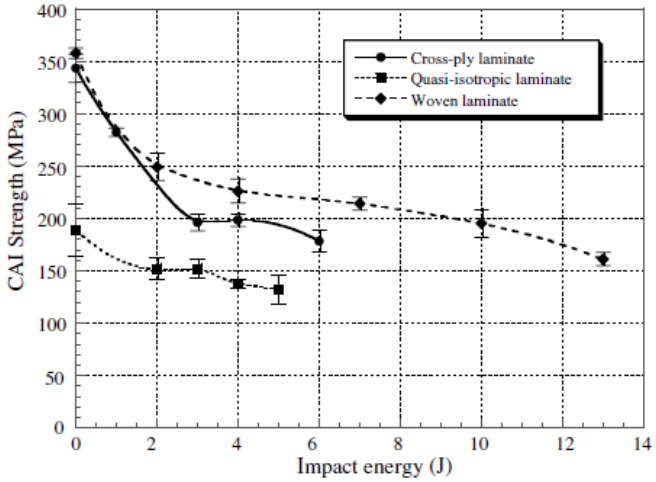

Figure 12: Average compressive residual strength values as a function of impact energy (Sanchez-Saez et al., 2005)

Their compression after impact results (Figure 12) showed that the woven laminate offered higher residual strength under all the impact energies. Due to the architecture of the fibers the laminate was able to better control shear cracking and delamination compared to the cross-ply and the quasi-isotropic lay-up, which possessed the lowest residual strength.The initial failure (matrix crackling) upon impact does not render the entire laminated composite damaged (Vaziri et al., 1996). Given that the reduction of the impact force to zero (i.e. acceleration of the impactor in the opposite direction after impact) follows a linear trend. The laminate can still carry load since other plies are still intact but to a lessened intrinsic limit. Additional impact of the same energy or lower on the exact location may not necessarily cause further matrix crackling to occur (Namala et al., 2014), there may be no further significant damage at all. For any given geometry of a laminated composite the direction of high stiffness will slow down the propagation of flexural waves developed after impact, as such delamination can be expected to first occur in the direction with the smallest modulus of elasticity.

1.2.3 Commonly used damage detection techniques

Damage in composite materials as discussed above can be a very complex in nature. It is important to look into the various contact and non-contact methods that are used to detect damage in laminated composites. The principles behind how the methods work, their advantages and limitations are discussed.

Non Destructive Testing (NDT) is more challenging for composites due to the different factors that influence the applicability of the inspection technique. Factors include the composition of the material, Thermal properties, atomic and acoustic properties. The most commonly used inspection methods in monolithic composites include radiography and vibration based techniques (Kapadia, 2007). The most common damage in laminated composites is delamination which result in air pockets, with radiographic testing the delamination can be detected so long as its orientation does not lie perpendicular to the x-ray beam (Gholizadeh, 2016).

Low voltage radiography is best suited for thin parts and gamma ray radiography is good for thick parts because the gamma rays have shorter wavelengths. With radiography even fiber wrinkles and non-uniform fiber distribution can be detected.

Thermography is based on the fact that defects tend to change the thermal conductivity of materials. This method is especially useful for detecting damage in thin parts, because defects that lie deeper under the surface of the material tend to generate less detectable heat fluctuations than defects which lie closer to the surface of the part (Gholizadeh, 2016). Defects with a diameter smaller than their depth in the part cannot be detected using thermography. Flaws such as impact damage and delamination cause a change in the thermal radiation of the material (Meyendorf et al., 2013). (Manes et al., 2018) compared the effectiveness of radiography and thermography in detecting impact damage size in aramid/epoxy laminated composites with varying number of layers. Their results showed that thermographic techniques were able to detect smaller damage sizes caused by ballistic impact than x-ray radiography (Figure 13).

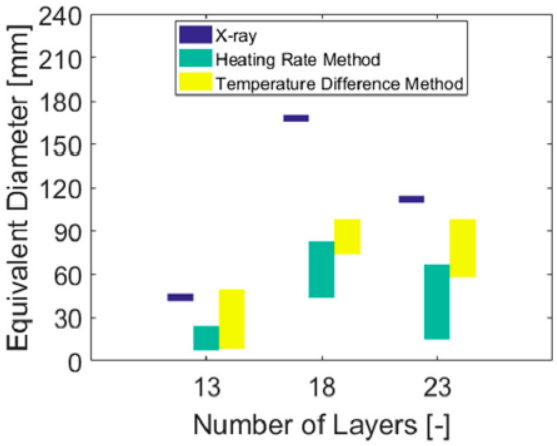

Figure 13: Comparison of the measurable values of equivalent damaged diameter for thermography and radiography (Manes et al., 2018)

Ultrasonic inspections such as pulse-echo and through-transmission use high frequency sound waves in the range of 1-50 MHz to detect internal defects such as delamination, porosity, foreign inclusion and translaminar cracks (Garney, 2006). In pulse-echo the interest is in the transit time of the wave and the loss of energy because of attenuation and wave scatter on the flaw. This makes the method useful in detecting inconsistencies in homogenous materials. Through-transmission ultrasonic testing is best for parts with complex geometries since the transmitter and receiver in this method are placed a fixed distance away from the surface of the part.

One of the most effective NDT methods is acoustic emission. It differs from other methods in that instead of supplying energy to the part, the method listens to sound generated by energy released in the object. Imperfections such as matrix cracks and fiber breakage result in stress waves which can be detected by highly sensitive piezoelectrics.

A comparative study (Kersemans et al., 2018) evaluated the capability of several non-destructive techniques used for detecting damage (i.e. hole damage and barely visible impact damage) in carbon fiber reinforced plastics (CFRP). The methods investigated were ultrasonic C-scan, local defect resonance and infrared thermography. Their results (Figure 14) demonstrated that ultrasonic C-scan performed well in detecting the damage along with the damage parameters such as size and depth. However, the method required water coupling and a long scanning procedure. The local defect resonance method demonstrated good damage detectability, but from the method defect parameters could not be extracted. From their inspections thermography proved to be the best performing method with good damage detectability within a short period of time. The defect parameters could be extracted as shallow as less than 2 mm in depth.

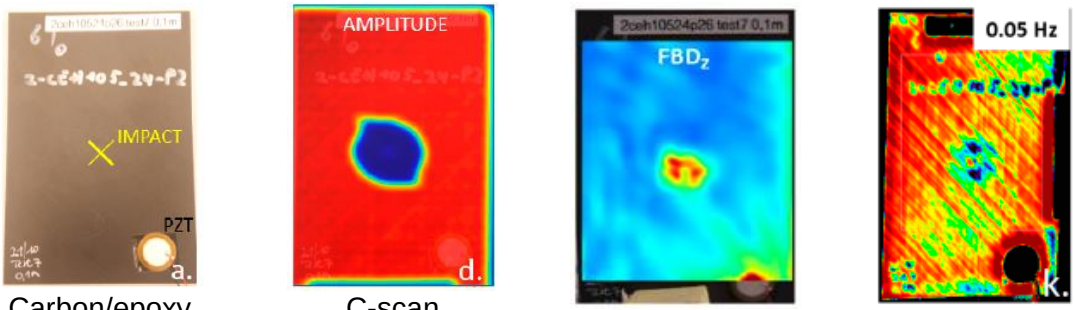

Carbon/epoxy laminate sample | C-scan | Local defect resonance | Infrared thermography

Figure 14: Barely visible impact damage images produced from ultrasonic C-scan, local defect resonance and infrared thermography (Kersemans et al., 2018)

1.2.4 Research based experimental techniques

This section looks at experimental techniques that have been derived from common methods of damage detection.

The analysis of natural frequencies (modal analysis) is another good technique for damage detection by estimating changes in mechanical properties from modal parameters. Since the natural frequencies of a system are determined by the boundary condition through the variable

lambda (λ), i.e. the eigenvalue. The characteristic equation of the structure determines the eigenvalue, which is multiplied by the ratio (IE/m) where I is the second moment of area, E is Young's modulus and m is the mass (Meirovitch, 1986). Changes in this ratio from loss of mass or stiffness leads to changes in the natural frequencies of the structure.

Figure 15 and Figure 16 show the experimental results of the work of Kessler et al. (2002). They conducted experimental modal analysis using a scanning laser vibrometer as a damage detection method on graphite/epoxy laminated composite which possessed a variety of damage mechanisms. The damage mechanisms include: 6.4 mm diameter centered hole damage caused by drilling, impact damage induced using a mallet, audible damage from compressively bending loading, compressive cyclic loading and delamination caused by cutting a slot (50 x 20 mm^2) on one side.

(All Hz)	Shape	Control	Hole	Impact	Delamination	Fatigue	Bend
Mode 1	First bending	12.5	12.5	12.5	12.5	12.5	12.5
Mode 2	Second bending	78.1	78.1	76.5	78.1	75.0	76.3
Mode 3	First torsion	157	148	147	137	146	137
Mode 4	Third bending	218	217	216	215	209	214
Mode 5	Fourth bending	423	423	423	428	413	423
Mode 6	Second torsion	461	453	453	451	428	432

Figure 15: Natural frequencies as determined from scanning laser vibrometer (Kessler et al., 2002)

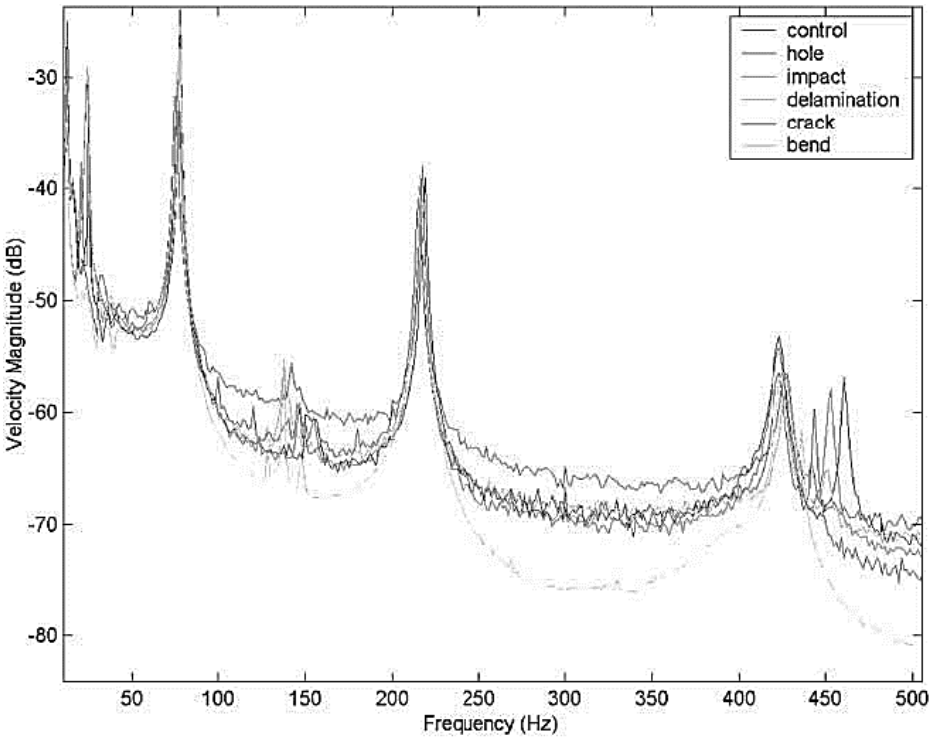

Figure 16: FRF of all specimens with various damage mechanisms (Kessler et al., 2002)

Figure 15 shows the experimental results of the scanning laser vibrometer, the results showed that reduction in stiffness and mass caused various damage mechanism resulted into a reduction in natural frequency values. The change in frequency is indiscernible at low frequencies but more distinctive at high frequencies as seen from the frequency response functions (Figure 16). Similar work has been conducted on cantilever aluminum plate-like structures with notches of different depths and sizes using the Galerkin method (Banks and Emeric, 1998). Through the use of the method the frequency response functions of their specimens also showed noticeable reduction in natural frequency values due to the notches at higher frequency ranges than a low frequencies. A dissertation by Prinsloo, (2011) showed shifts in natural frequencies obtained using a scanning laser vibrometer (non-contact setup) of a sandwich composite UAV wing due to delamination.

Some NDT techniques for Carbon Fiber Reinforced Plastics (CFRPs) are based on mathematical models for thermographic data processing from thermal excitation. (Chrysafi et al., 2017) made use of active infrared thermography and recorded the temperature of CFRP samples with delamination and cracks at known location. The thermograms of the laminates were processed in two ways: a) as two-dimensional images, b) as if each pixel was a one-dimensional signal over time. Their work demonstrated the accuracy of using the norm of the first spatial derivative of temperature as well as two dimensional wavelet transforms for crack detection. The delamination in the samples was more accurately detected by using one dimensional Fourier transforms and wavelets (Figure 17).

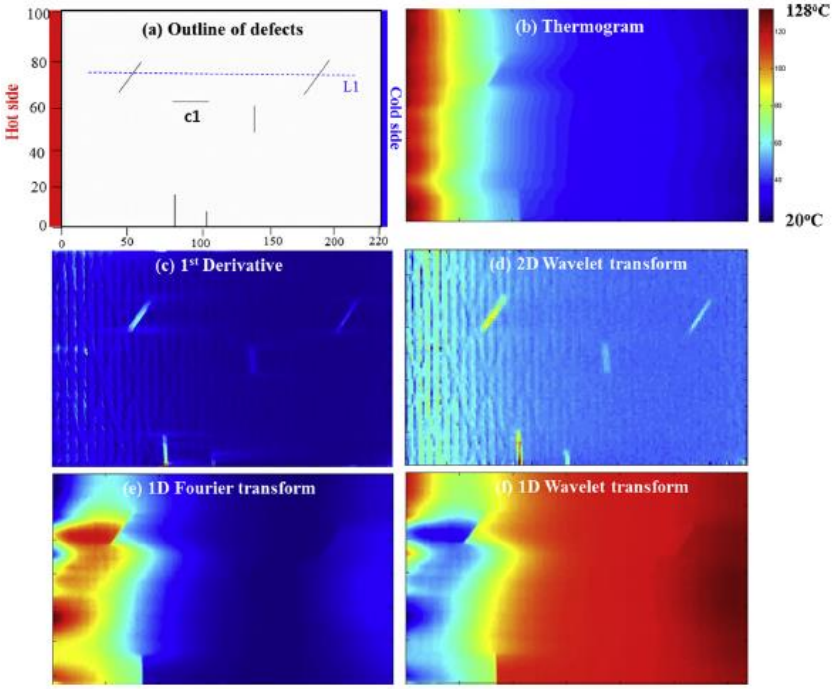

Figure 17: Sample with ply layup $(0^o)_2$: (a) location of known defects, (b) thermographic image after 20 seconds of excitation, (c) norm of the first derivative, (d) 2D wavelet transform, (e) 1D Fourier transform, (f) 1D wavelet transform (Chrysafi et al., 2017)

The one-dimensional Fourier and wavelet transform proved ineffective in detecting the orientation and location of cracks. Only the defect near the heat source was visible, whereas with the two-dimensional transform most of the cracks and their orientation were detected. The use of one dimensional transforms showed great accuracy in detecting delamination in the laminates (Figure 18).

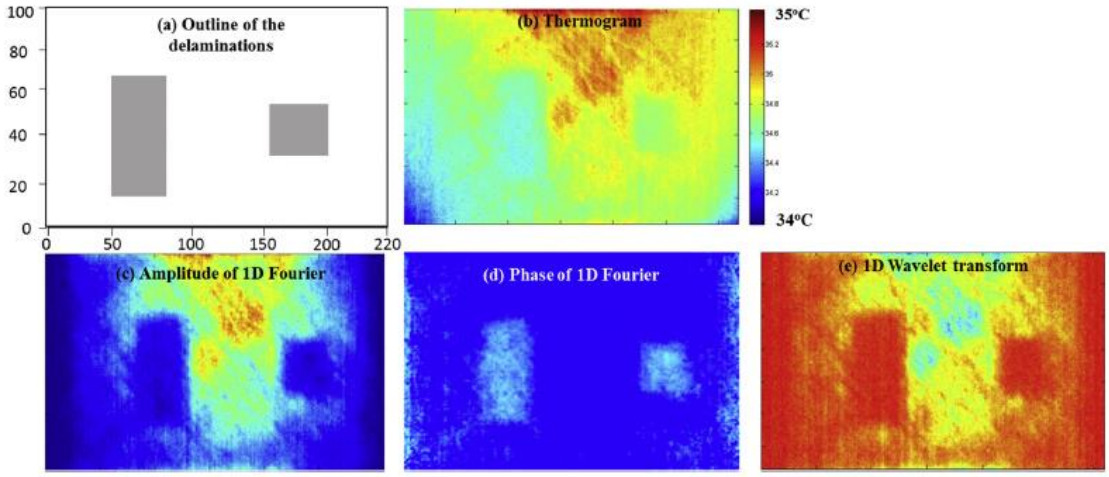

Figure 18: Sample with ply layup $(\pm 45^{o})_2$: (a) location of the delamination, (b) thermographic image after 1s of excitation, (c) amplitude of 1D Fourier, (d) phase of 1D Fourier, (e) 1D wavelet (Chrysafi et al., 2017)

Work on wavelet transforms was also carried out by (Faria et al., 2017). They focused on improving the ability of continuous and discrete wavelet transforms in laminated composite plates to detect matric damage by signals derived from high and low vibrational modes. Simulations were conducted on both the undamaged and damaged numerical models with a fixed end along four of the edges. 400 mm x 300 mm x 1 mm thick glass/epoxy composites with ply layup of $(90^{o}/0^{o}/90^{o})_3$ were modelled for the simulation. The damage was caused by applying an impulse force as a function of time on the model. An error percentage in the first 10 natural frequencies of the undamaged and damaged model was found to be in the range of 0.007 % to 0.3 %, signifying stiffness degradation. Figure 19 shows the analysis of the damaged model.

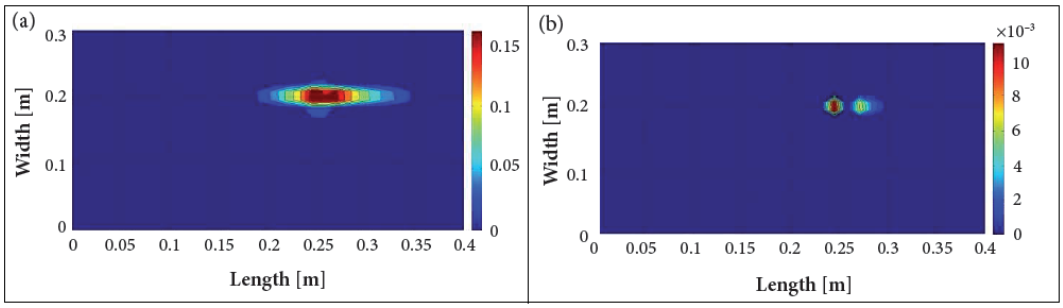

Figure 19: Numerical model of damage scalar variable distribution: (a) external layer of the laminate, (b) internal (central) layer of the laminate (Faria et al., 2017)

The difference in the damage distribution on different layers illustrated in Figure 19 is a result of through thickness linear stress variation of the laminate. Maximum damage can be noticed on the external layer and decreases moving toward the center, a consequence of the ply orientation. The signals from the vibrational modes of the undamaged and damaged plate model were interpolated using cubic splines in order to grow the numerical data. Signal processing was done using the mother wavelets Daubechies and the signal's decomposition achieved through wavelet transforms.

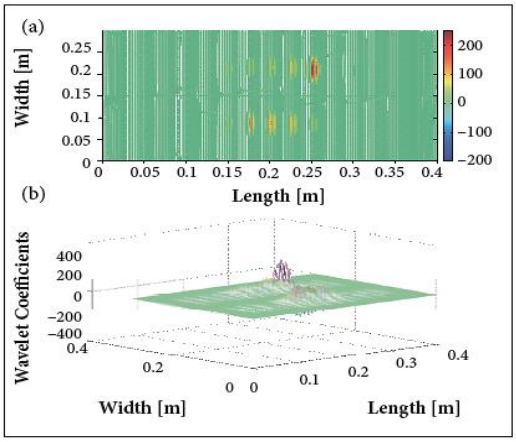

Figure 20: Wavelet coefficients of the discrete wavelet transform: (a) flat distribution along the flat surface, (b) spatial distribution for the plates' dynamic signal computations (Faria et al., 2017)

Their results showed that damage was incurred at the location where the load was applied. From the first ten natural frequencies between the undamaged and damaged model of the composite, it was noticed that the frequencies of the damaged model decrease indicating loss of stiffness with increase in the calculated damage variable. Figure 20 shows how the discrete wavelet transform was able to estimate the damage location same as with the continuous wavelet transform.

It has been shown that the damage of carbon fiber reinforced polymer composites (CFRPs) is linked to the change in the material's electrical resistance (Wen et al., 2013). Electrical resistance measurements allows in-situ monitoring of growth of internal defects such as interply matrix cracks, delamination and fiber fracture. Damage detection by measuring electrical signals is often contaminated by noise which introduces difficulty in measuring the signals. Wen et al. (2013) made use of Fast Fourier Transforms to filter unwanted noise. When the noise is significantly larger than the input signal, inaccurate electrical signals are obtained. They made use of joint time-frequency technique with continuous and discrete wavelet transforms to overcome the drawback.

Crall et al. (2019) examined the accuracy of magnetic and thermal sensing methods to detect damage in fiber reinforced composites. Work has been done to visually see damage within the composite near the surface by introducing chemicals in the matrix in the form of microcapsules. When the capsules are ruptured by compromised fibers, they release agents which undergo a chemical reaction that forms a colour change around the damaged area (Li et al., 2016).

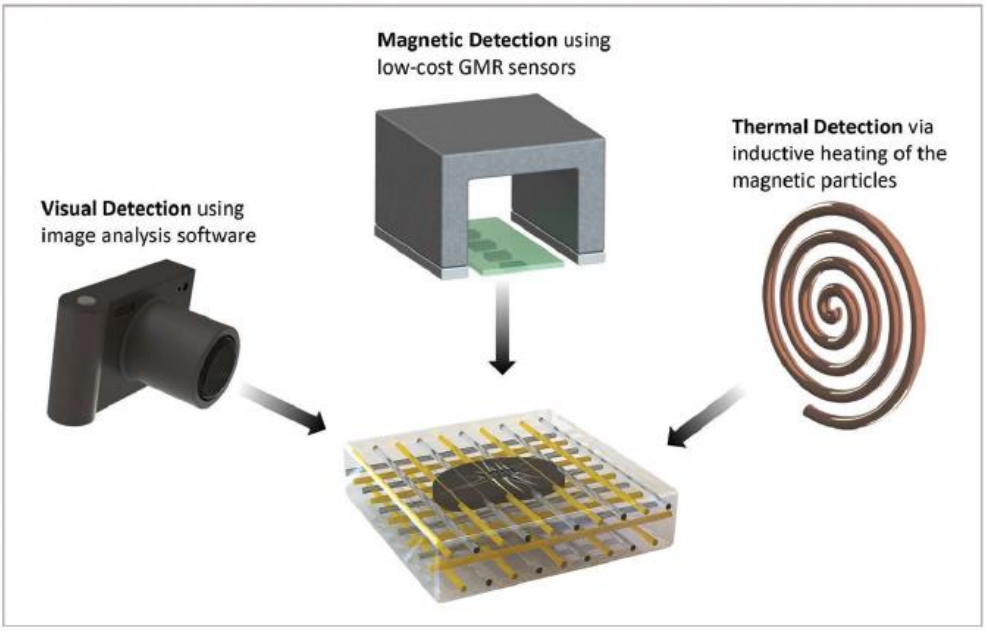

Figure 21: Three modes of damage detection in a vascular composite (Crall et al., 2019)

Most of these techniques which communicate the presence of damage visually fall short in communicating the severity of the damage through the thickness of the material. Crall et al. (2019) demonstrated a vascular composite which is capable of multimodal damage detection through the thickness.

Chemicals stored separately in the vascular network are released in the fractured zone and react to form an agent which consists of magnetic particles. This process forms a magnetic damaged area that can be magnetically, thermally and visually be detected (Figure 21).

The magnetic damage region is the product of a chemical reaction between an iron salt solution that contains ferric chloride, ferrous chloride and deionized water with Ammonium hydroxide concentrate. The high contrast biomimetic magnetic damaged area can be then be observed visually, a range of magnetic sensors can be used to interact with the damaged area, and inductive heating of the magnetic particles causes temperature changes which can be observed with a thermal camera. Figure 22 shows the detection accuracy of the method compared to C-scan results.

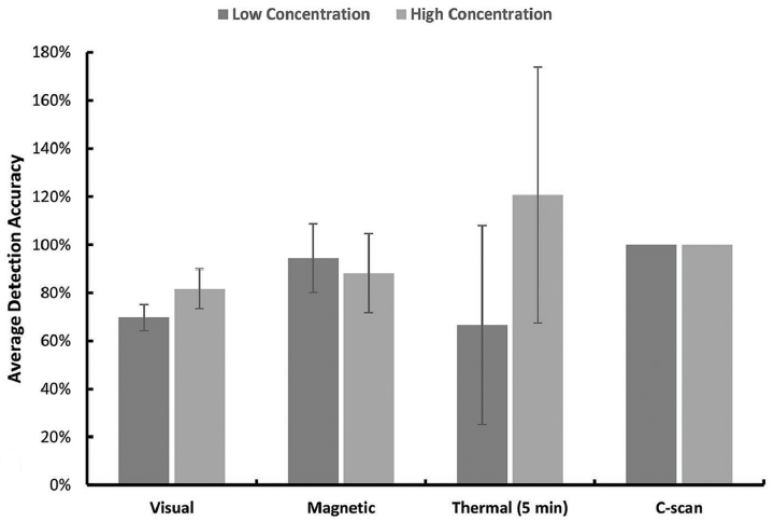

Figure 22: All methods accuracy compared to C-scan, error bars denote one standard deviation based on six models (Crall et al., 2019)

A thesis by Michelle Dubose Spiegel. (2014) demonstrated the use of piezoelectric sensors and actuators to detect damage in unidirectional carbon/epoxy composite panels with a ply scheme of $(0^o)_{16}$. The actuator mounted on the surface delivered Lamb waves of which the response was measured by the sensor. The thesis focused on two methods for using Lamb waves to detect damage i.e. pitch and catch method and pulse echo method. Damage on the test coupons was introduced in form of holes of different sizes drilled into the specimen as shown in Figure 23.

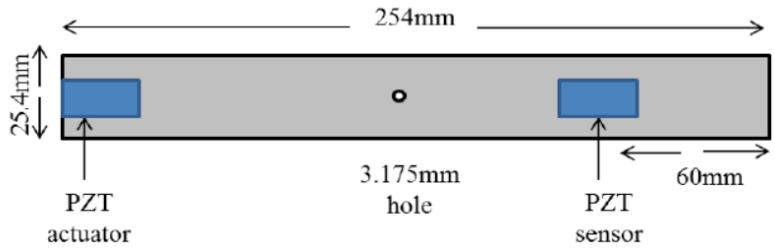

Figure 23: piezoelectric sensor and actuator setup (Spiegel., 2014)

The experimental data showed that the amplitude of the response signal increases as the size of the hole increases. The signal amplitude also increases with increase in the amount of damage introduced on the specimen (more holes) with noticeable phase shifts towards the end of the signal, further verifying the presence of damage (Figure 24).

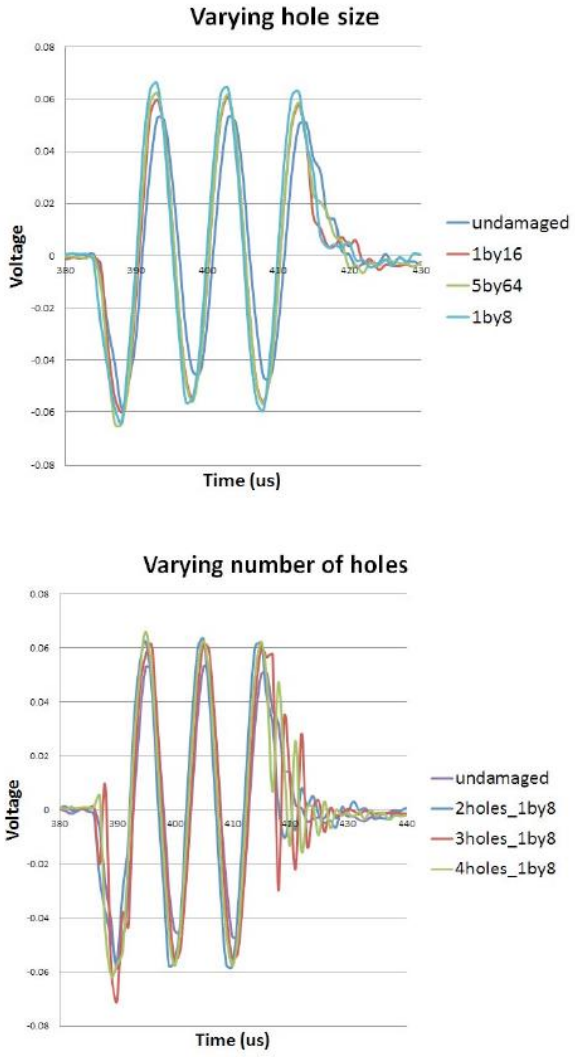

Figure 24: Response signal from varying hole size and number (Spiegel., 2014)

Similar experimental work to that of Spiegel. (2014) has been carried out using Lamb wave to detect microstructural damage in composites caused by impact loading (Rauter and Lammering, 2014). They used Lamb waves at a certain frequency to generate cumulative second harmonic modes in a unidirectional carbon/epoxy composite with a $(0^{o})_4$ ply scheme.The dispersive and multi-modal nature of the Lamb wave made it difficult to accurately determine the amplitude of the harmonic wave modes. To overcome the difficulty, signal processing was done using wavelet transform. Their work demonstrated that the nonlinear propagation properties of the Lamb wave was a sensitive detector of micro-structural damage.

1.3 Conclusion to literature review

Laminated composites are versatile materials in the mechanical sense. A key characteristic of their behaviour in response to damage is that the effects do not always materialize immediately on the surface for the naked eye or NDT methods to detect.

Various damage mechanisms in laminated composites result from impact, fatigue and manufacturing flaws. In all cases matrix damage (cracks) is the first mechanism of failure. Continued damage from the source causes the matrix cracks to propagate and eventually coalesce leading to delamination. Fiber damage occurs as a result of uneven distribution of the stresses to fibers in the plies due to matrix failure. In some cases matrix and fiber failure occur simultaneously when the source of damage is severe enough.

Impact damage is commonly incurred in laminated composites, the resultant damage is often barely visible on the surface of the laminate (i.e. barely visible impact damage). For instance the damage can occur during manufacturing, part assemblies or from airborne debris carried by the elements. The initial site in their composition to experience failure is the matrix which binds the fibers and fabrics together (Tuo et al., 2019) and (Malhotra and Guild, 2014). Compromised regions within the matrix are the ideal settings for loss of strength under the loading circumstance and inevitably delamination. When the impact is severe enough, fibers of the impact surface plies will immediately separate.

Many methods have been developed for the purpose of detecting damage in composites based on the fact that defects tend to causes disturbances in the stimuli supplied to the composite material for excitation. The disturbances can be picked up in a variety of ways from signal processing to optical sensors. In modal analysis the change caused by the presence of defects manifests as shifts in natural frequency values (Kessler et al., 2002) which may be linked to changes in the stiffness and mass of the subject. The methods of thermography and ultrasonic testing have been given attention towards improving damage detection by employing mathematical transformations for data processing (Chrysafi et al., 2017).

Current practices of damage detection in laminated composites such as C-scans, X-ray, ultrasonic testing and thermography require strict adherence to lengthy procedures in order for effective damage detection. X-ray requires that the orientation of the damaged area not lie perpendicular to the x-ray beam for effective detection (Gholizadeh, 2016). Thermography is most effective for thin parts when the damage is closer to the surface. In thick components any damage that lies deeper into the surface results in weaker thermal fluctuation for effective damage detection (Gholizadeh, 2016). C-scan although effective in detecting damage with the benefit of also providing the damage parameters such as the size, requires a lengthy scanning period (Kersemans et al., 2018). All the methods discussed use the fact the flaws cause materials to behave differently when subject to some form of excitation. This research aims to do in a similar manner, use the change in deformation data brought about by the loss in stiffness as a damage indicator for laminated composites. A method which can be implemented regardless of the material's thickness, damage size, damage orientation or thermal properties.

1.4 Project plan and flow diagram

The first phase of the research is structure in such a manner so as to evaluate the technique of modal analysis and full field DIC in detecting barely visible damage in laminated composites. Modal analysis was conducted in two ways: contact and non-contact modal analysis. In contact modal analysis the excitation instrument (i.e. modal hammer) made physical contact with the target surface for excitation. In non-contact modal analysis no physical contact occurs between the target surface and the source of excitation. Modal analysis was considered as one of the methods as it has been used successfully in the literature to detect impact damage (Kessler et al., 2002) in laminated composites.

In this research the contact method is used to validate the non-contact method. This is because the non-contact method holds the benefit of automation and the ability to generate the mode shapes. The contact method was conducted on both the undamaged and damaged composites to check for shifts in natural frequencies values which would indicate damage.

Prior to conducting the full field DIC experiments under static loading on the laminated composites, a couple of tests were conducted to evaluate full field DIC. The test were setups to capture rigid body motion and out-of-plane deformation using DIC. The results from the DIC were compared to independent measurements taken simultaneously during the tests. Once the independent measurements and full field DIC data were in agreement, experiments on the composites were conducted. The interest from DIC data is the peak out-of-plane deformation data (i.e. displacement and strain) and loss in stiffness under static and dynamic loading. The availability of equipment invoked the interest for DIC investigations under both static and dynamic loading conditions, in order to evaluate benefits and limitations of each setup.

The changes in the experimental data between the undamaged and damaged laminated composite from the modal and full field DIC were used to decide upon the best method for damage detection in laminated composites. The effective method would then be the focus of the next investigation, in which the technique would be used to evaluate how well it could detect barely visible damage induced from impacts of varying energies at different locations of the specimens (i.e. center and off-center impact).

From the literature review on modal analysis shift in natural frequencies due to the damage were observed at frequencies larger than 300 Hz (Kessler et al., 2002). Due to the lack of information regarding the orthotropic properties of the specimens and the precise manufacturing process, the appropriate frequency range for the experimental modal analysis in this research was uncertain. A range of up to 1000 Hz was selected to detect any noticeable shifts in natural frequencies. The same composites used in the modal analysis were used for full field DIC experiments. To ensure that no additional damage occurred, the loads for full field DIC under static loading were kept below the loading used to cause audible damage. For full field DIC under dynamic loading conditions, the impact energy used was that which resulted in displacements similar to those obtained under static loading conditions for the undamaged specimen.

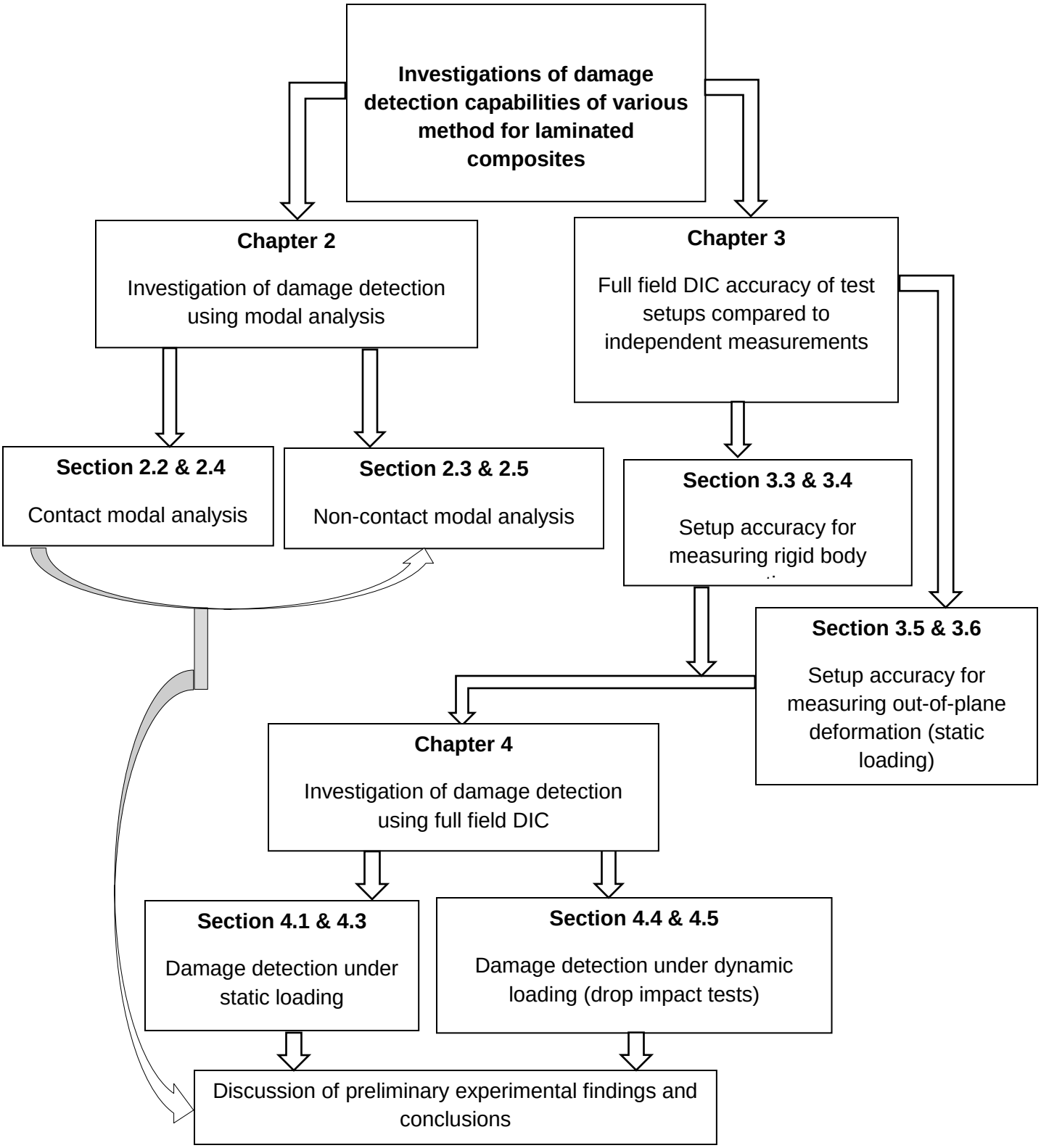
Investigations of damage detection capabilities of various method for laminated composites
Chapter 2
Investigation of damage detection using modal analysis
Chapter 3
Full field DIC accuracy of test setups compared to independent measurements
Section 2.2 & 2.4
Contact modal analysis
Section 2.3 & 2.5
Non-contact modal analysis
Section 3.3 & 3.4
Setup accuracy for measuring rigid body
Section 3.5 & 3.6
Setup accuracy for measuring out-of-plane deformation (static loading)
Chapter 4
Investigation of damage detection using full field DIC
Section 4.1 & 4.3
Damage detection under static loading
Section 4.4 & 4.5
Damage detection under dynamic loading (drop impact tests)
Discussion of preliminary experimental findings and conclusions

1.5 Project contribution

Non-Destructive testing (NDT) is a broad field which is changing dynamically and is rich in innovation. Inspection for damage must also be conducted while the test object is online or offline. NDT is often of great importance for mechanical systems for maintenance and safety reasons. There are two forms of NDT namely contact and non-contact NDT, the most favored being non-contact due to the benefits such as automation and less interference during contact.

In this research various methods for damage detection were explored in order to inform an investigative protocol based on available equipment. Modal analysis has been successfully employed for damage detection in laminated composites. The damage can be detected as shift in natural frequency values (Kessler et al., 2002) and (Banks and Emeric, 1998). Two approaches of modal analysis were considered in this research, namely contact and non-contact modal analysis. The intention was to use the contact approach to validate the non-contact method and corroborate the obtained mode shapes corresponding to the excited natural frequencies. Once agreement was obtained between the two approaches to modal analysis, either one could be used for damage detection. In this research contact modal analysis was used. The results demonstrated that for the type of damage which is of interest in this research (i.e. Barely Visible Damage and Barely Visible Impact Damage) modal analysis was not effective even in the high frequency range (with no distinguishable shifts in natural frequencies between the undamaged and damaged laminated composites).

The literature on the types of damage laminated composites can incur (i.e. section 1.2.2) demonstrates that the damage diminishes the composite's mechanical abilities, specifically the young's modulus in all three directions (i.e. reduction in stiffness). The loss in stiffness tends to change the response of the composites when they are excited in certain ways such as vibrational excitation (Faria et al., 2017) and (Kessler et al., 2002), electrical stimulation (Spiegel. 2014) and wave signal manipulation. This presented an opportunity to employ deformation data capturing equipment as the next method for exploration, since deformation behaviour changes with change in stiffness. The literature on ways in which DIC has been successfully employed to capture deformation data (section 3.1.5) informed the use of full field DIC as the next method to investigate in terms of damage detection. Full field DIC experiments were conducted under static and dynamic loading condition for damage detection. Barely visible damage was better detected using full field DIC under static loading condition.

The work presented in this research aims is to demonstrate the capabilities of experimental modal analysis and full field DIC as non-destructive test techniques for barely visible damage in laminated composites. In a structured format the study focuses down to the most fitting technique for detecting barely visible damage, which in this case is full field DIC under static loading. This research aims to add full field DIC under static loading to contact NDT methods capable of detecting barely visible damage (BVD) and barely visible impact damage (BVID) in laminated composites. The results achieved in this investigation show that full field DIC can be used for damage detection when the interest is in the reduction in stiffness caused by the damage rather than the identification of the exact damage mechanism. In the composite industries there are standards of minimal allowable damage that govern their use which is directly linked to the material stiffness.

1.6 Overview of preliminary experiments for damage detection in laminated composites

An investigation of damage detection capabilities of various methods for laminated composites were explored. The outline of the preliminary investigations is given which includes how the damage was induced in the composites. A description of the laminated composites which were the subjects of the various methods used to attempt to detect barely visible damage are given.

Two techniques of detecting damage in composites are explored: experimental modal analysis and full field DIC. Barely visible damage (BVD) and barely visible impact damage (BVID) are characterized by cracks and fiber breakage in the composite, the propagation of barely visible damage leads to delamination of the plies that make up the composites. Two techniques are used to attempt to detect this type of damage, the first was modal analysis which in many cases has been a successful technique in detecting damage in many components (Banks and Emeric, 1998) and (Kessler et al., 2002). The second was full field Digital Image correlation (DIC) which is commonly used to capture deformation data which can be correlated to finite element simulations. In this preliminary investigation study carbon/epoxy woven laminated plates were the subject of the experiments with no information regarding their mechanical properties.

Two methods of modal analysis were conducted on the composite plate, namely, contact modal analysis in which a modal hammer was used as the exciter and a non-contact method in which a signal was used for excitation. In both methods a freely suspended setup of the composite test piece was used to simply boundary conditions and minimize damping. The results of the contact method were used to validate the non-contact method from which the mode shapes could be obtained. The results of the undamaged and damaged composite were compared from the FRFs obtained using the contact method.

The full field DIC experiments were conducted under static and dynamic loading conditions, prior to actual testing of the composite plate a couple of experiments were performed to characterize the accuracy of full field DIC In measuring rigid body motion and out-of-plane deformation. The results of interest from the full field DIC experiments on the composite plate are peak out-of-plane displacements and force versus displacements curves for the undamaged and damage composite plates.

1.7 Description of laminated composites for preliminary experiments

The laminated composites plates were manufactured from twelve carbon plane-weave plies pre-impregnated with resin (prepreg fabric). The plies were fused together in an autoclave. The specimens was donated and thus precise details of the manufacturing process and overall material properties are unknown. Known details of the panel are given below:

- Material: Carbon woven fabric prepreg.
- Number of plies: 12 plies.
- Ply scheme: $[0^0]_{12}$
- Dimensions: 183mm x 133mm x 2.5mm.

Figure 25: Woven carbon/epoxy laminated composite panel

The damage in the carbon/epoxy woven laminated plate was caused by subjecting the plate to a point load. A pneumatic actuator was used to generate the force which was delivered to the specimen via the piston and 30mm ball. The force was increased until cracking of the matrix within the composite could be heard.

Chapter 2: Preliminary investigation of the capabilities of experimental modal analysis for damage detection in laminated composites

An investigation on the damage detection capabilities of experimental modal analysis in laminated composites was explored. Two forms of experimental modal analysis were performed (i.e. contact and non-contact modal analysis). The theory behind modal analysis is given prior to the details of the actual experimental setups and results.

2.1 Theory of modal analysis

Modal analysis has been a primary tool in understanding linear structural systems. Natural frequencies are inherent properties of a structure and are governed by material properties such as mass, damping, stiffness and boundary conditions of the structure. Natural frequencies are frequencies at which a structure tends to oscillate when subjected to external excitation. The natural frequency are accompanied by mode shapes which describe the manner in which the structure deforms when it is excited at its natural frequencies. In engineering natural frequencies are identified so as to avoid operation of the structure at the frequencies which will cause the structure to resonate and failure. The result of a modal analysis is a Frequency Response Function (FRF) i.e. a plot of magnitude against the frequency (Figure 26).

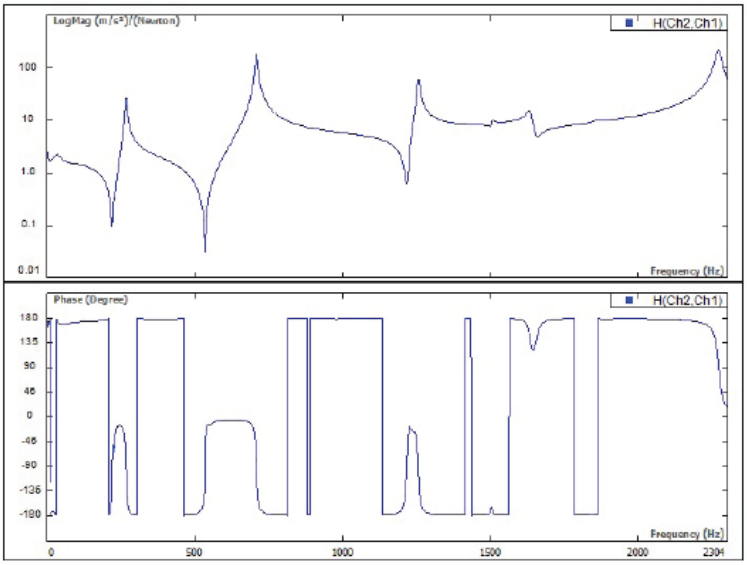

Figure 26: FRF with magnitude plot (top graph) and phase lag plot (bottom graph) plotted against frequency (Crystal Instruments manual, 2017)

Natural frequencies are identified as the peaks on the FRF graph. An FRF graph is also associated with a phase lag graph in which a phase change of 180° represents a natural frequency. Modal results similar to those in figure 26 are expected for the experimental modal analysis on the test coupons. Sharp peaks on the FRF in Figure 26 indicate a system with very little damping, in order to obtain a similar FRF a complete free modal analysis was conducted using a contact and a non-contact modal analysis.

2.2 Experimental setup for contact modal analysis

Two methods of the analysis were conducted i.e. a) contact modal analysis and b) non-contact modal analysis. The contact modal analysis in which a modal hammer with a plastic tip was used to excite the composite is shown as a schematic in Figure 27.

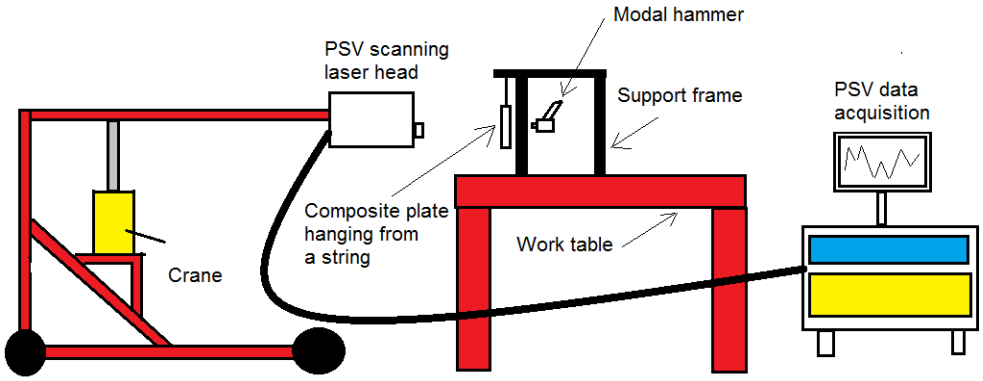

Figure 27: Side view schematic of the experimental setup for contact modal analysis

A hand operated crane was used to support the PSV scanning laser head positioned to face the front face of the composite plate. A cotton string was used to hold the composite plate in position. It was attached to the top right and left corners of the plate by means of adhesive tape. Using a light cotton string and tape to position the plate eliminated adding unwanted mass to the system which could slightly influence the results. A steel support frame was used as a means of support for the string. Excitation was provided by striking the back face of the plate using a modal hammer.

Figure 28 shows the setup of the actual experiment. The surface of the composite plate used for measurements was prepared by first cleaning it with acetone. Small pieces of reflective tape were placed on the surface in grid form to serve as points for the laser to scan. The laser vibrometer is one beam laser interferometer that is split into the target and reference beam. It measures the phase or frequency difference of the internal reference beam and that reflected by the excited specimen onto the photo detector.

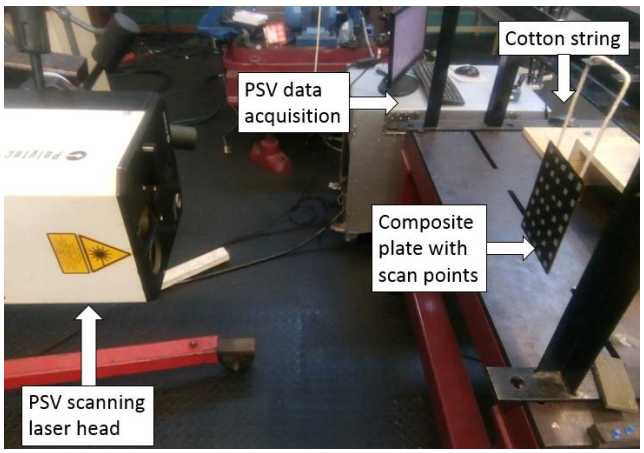

Figure 28: Experimental setup for the contact modal analysis

The reflective pieces of tape seen in Figure 28 served to strengthen the reflected beam received by the photo detector from the excited target surface for more accurate results free from excessive noise. The center of the plate near the left edge was selected as the striking location for the measurement of each scan point until the optimum point which resulted in the desired result was identified.

2.3 Experimental setup for non-contact modal analysis

For the non-contact analysis a signal generated within the PSV data acquisition and transmitted through a speaker was used for excitation. The non-contact method holds the benefit of automation and the mode shapes can only be obtained using the method.

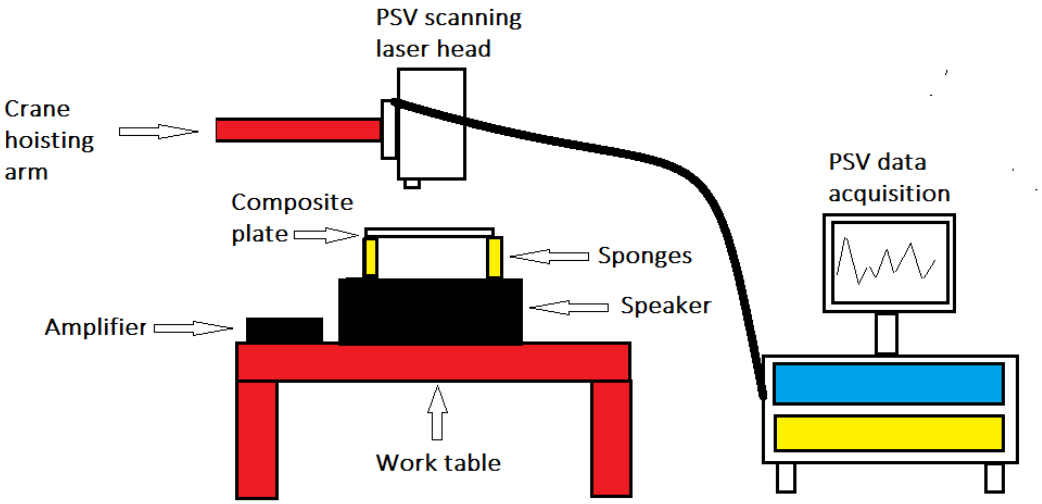

Figure 29: Side view schematic of the non-contact modal analysis experiment

Figure 29 shows a schematic of the test setup for the non-contact modal analysis. The same instruments used for the contact method were also used for the non-contact modal analysis. Since in this method a signal was required to excite the composite plate, an amplifier and speaker were added to the setup to provide the excitation signal generated from the PSV data acquisition. In this setup the orientation and the manner in which the composite plate was supported differs to the setup of the contact method, the plate was supported on two of its edges by sponges.

Figure 30 shows the experimental setup for the non-contact modal analysis. Figure 30(a) shows the laser vibrometer held in position by a hand operated crane above the target surface of the composite plate. The laser vibrometer was used to make non-contact vibration measurements of the excited surface. Figure 30(b) shows the composite plate with two of its edges supported on sponges above the speaker so as to offer as little damping as possible. This setup was found to be the most accurate in terms of the number of expected natural frequencies, after having explored the option of suspending the specimen above the speaker using rubber bands and thin cotton strings which resulted FRFs with some of the expected natural frequencies unexcited in both cases.

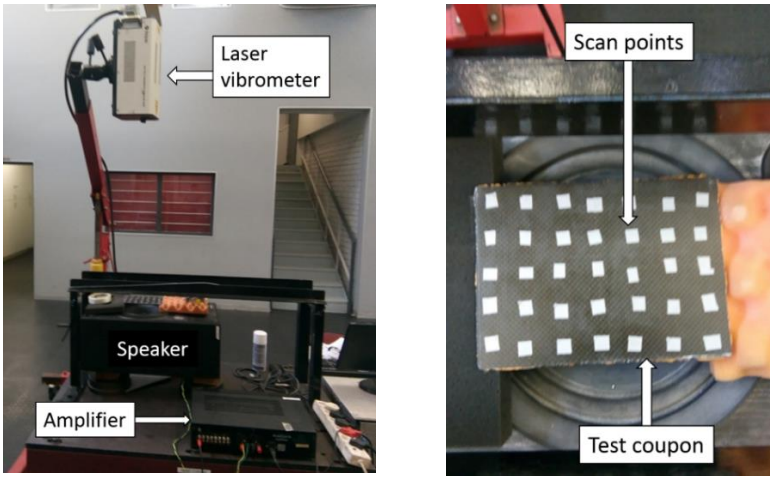

Figure 30: Non-contact modal analysis experimental setup: (a) shows the PSV laser held above the composite, (b) shows the composite suspended above the speaker by two sponges

Pieces of reflective tape were placed on the target surface and served as locations where the PSV laser measured the vibrational response (i.e. scan points). With the setup shown in Figure 30 free-free modal analysis was performed with a periodic chirp signal used to excite the specimen via an amplifier and speaker.

2.4 Contact modal analysis results of undamaged composite

Figure 31 shows the frequency response functions obtained from the contact modal analysis on the undamaged composite. A hand held modal hammer was used to excite the specimen and the laser vibrometer was used to measure the vibrational response. All the experiments were conducted following the settings outlined in the experimental procedure along with the parameters to alter to better refine the results.

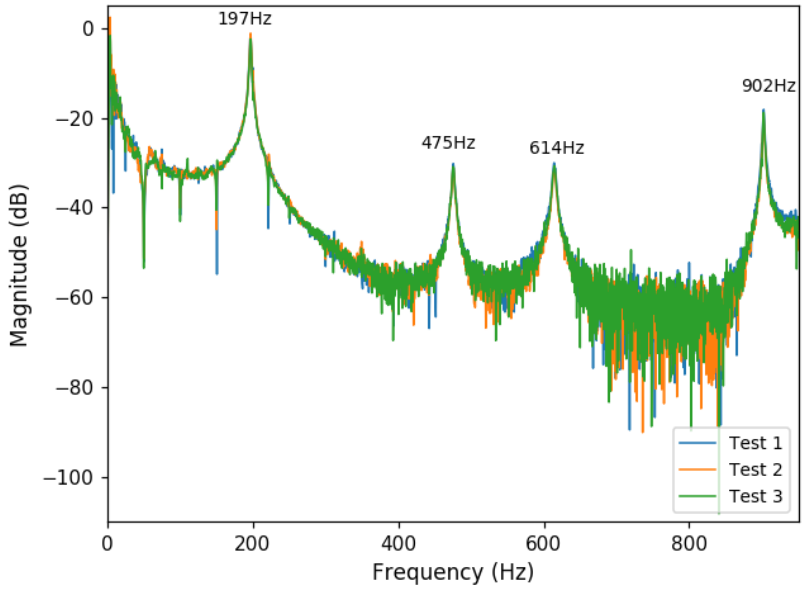

Figure 31: Contact modal analysis FRF of undamaged composite, with reference of 0 dB = 1 m/s/N

In order to insure that all modes participate when the composite panel was excited by the modal hammer, all locations marked with reflective tape were struck and the resulting FRFs compared to see all participating natural modes in the chosen frequency range. Some of the natural frequencies were not excited on the FRFs obtained from striking certain points. Through the comparison of all the FRFs the optimal point was found and marked on the specimen, in which all natural frequencies within the frequency range occurred.

The frequency response functions shown in Figure 31 were obtained by performing the experiment three times, exciting the system at the optimal location, to demonstrate repeatability. All the peaks occur at the same frequencies in each test. Six natural frequencies were excited within a frequency range of 950 Hz as seen from the frequency response functions in Figure 31. The peaks of the excited natural frequencies appear sharp indicating a system with little damping. The noise between peaks on the frequency response functions can be attributed to the electrical sources such as the electrical cable of the hammer as well as speckle noise from the motion of the specimen after being struck by the modal hammer.

Figure 32 shows one of the tests along with its phase graph in order to confirm that the peaks are indeed natural frequencies and not unidentified noise. A phase change of 180° exists at each peak on the phase graph confirming them as natural frequencies. The noise at high frequencies (i.e. larger than 600 Hz) in Figure 32 may be due to the combination of speckle noise and difficulty of getting sufficient energy into the system at high frequencies.

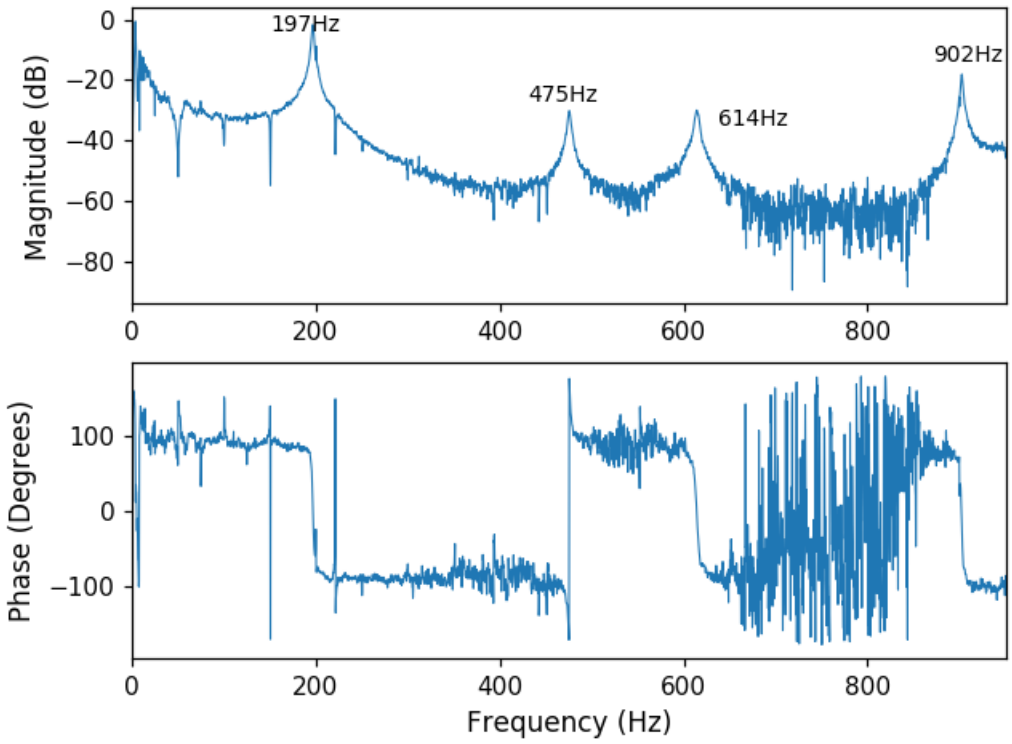

Figure 32: Contact modal test FRF and phase graph with the reference 0 dB = 1 m/s/N

2.5 Non-contact modal analysis results of undamaged composite

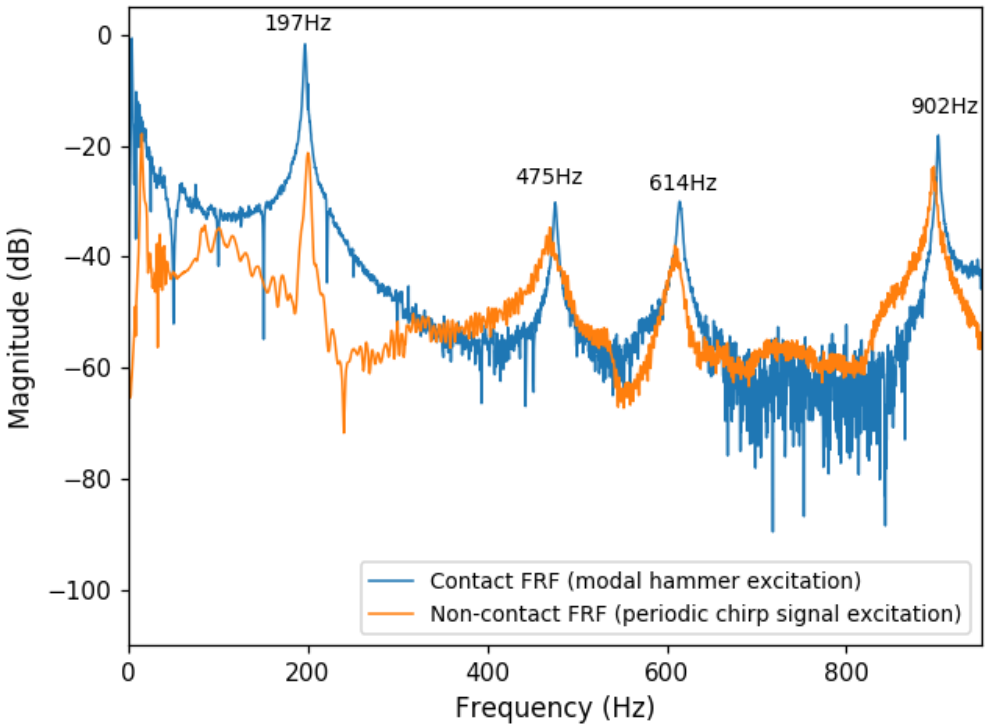

Figure 33: Contact and non-contact FRF of undamaged composite with the reference 0 dB =1 m/s/N for the contact FRF and 0 dB =1 m/s/V for the non-contact FRF

Figure 33 shows the frequency response functions from the contact modal analysis in which a modal hammer was used for excitation, superimposed with the frequency response function from the non-contact modal analyses in which a periodic chirp signal generated via a speaker was used for excitation.

Table 1: Summary of natural frequency values for the contact and non-contact modal analysis

Contact FRF	197 Hz	475 Hz	614 Hz	902 Hz
Non-contact FRF	198 Hz	473 Hz	610 Hz	899 Hz

The frequency response functions of the contact and non-contact modal analysis shown in Figure 33 are in good agreement in terms of the excited natural frequencies (i.e. minimal difference in the values of the natural frequencies shown in Table 1). The small difference in excited natural frequency values can be ascribed to the additional transmission path from the speaker box through the sponges to the composite plate. The peaks on the frequency response function from the non-contact method are also sharp indicating a system with little damping.

The difference in profile between the two frequency response functions is due to the difference in the mode of excitation, i.e. concentrated load from the modal hammer and a distributed load from the pressure field generated by the driving signal.

Significant reduction in noise can be observed from the non-contact frequency response function bearing a smoother profile than the frequency response function from the contact analysis.

In the non-contact modal analysis setup, the specimen was supported at two of its edges by sponges placed on top of the speaker. Looking at the agreement that exists between the FRF of the contact and non-contact modal analysis there is insignificant transference of the speaker box natural frequencies into the system via the sponges.

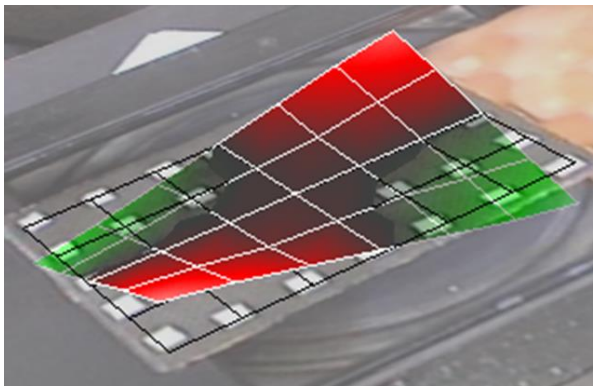

(a) 198 Hz first torsional mode

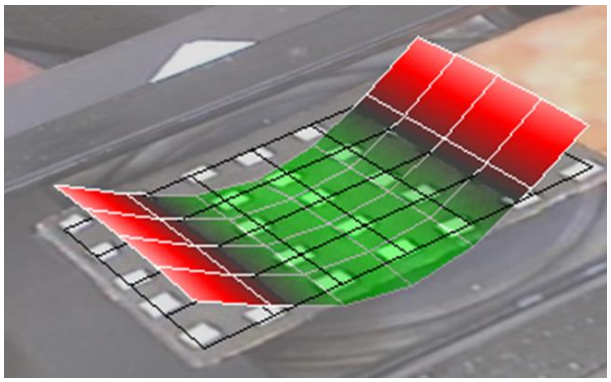

(b) 473 Hz first bending mode

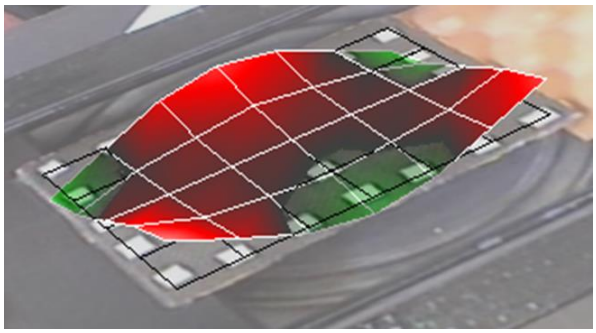

(c) 610 Hz second torsional mode

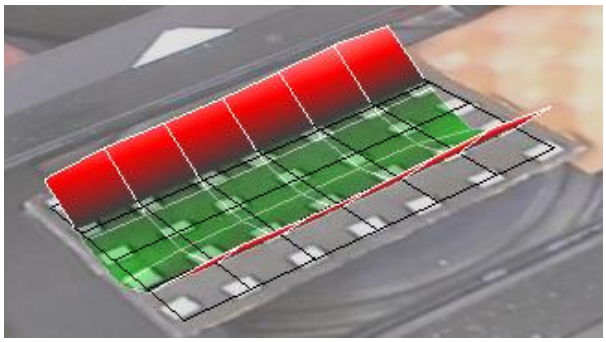

(d) 899 Hz second bending mode

Figure 34: First four operational deflection shapes obtained from the non-contact modal analysis

Figure 34 shows the first four operational deflection shapes from the peaks of frequency response function of the non-contact modal analysis. The mesh of the model was generated by connecting the defined scan points in the PSV laser analyzer (i.e. locations on the target surface where the pieces of reflective tape were placed). The scan points can also be seen in Figure 34 on the undeformed model in each mode shape. The difference in colour observed on the mode shapes indicate upward (red) and downward (green) motion from the reference position of the specimen.

2.6 Comparison of undamaged and damaged composite modal results

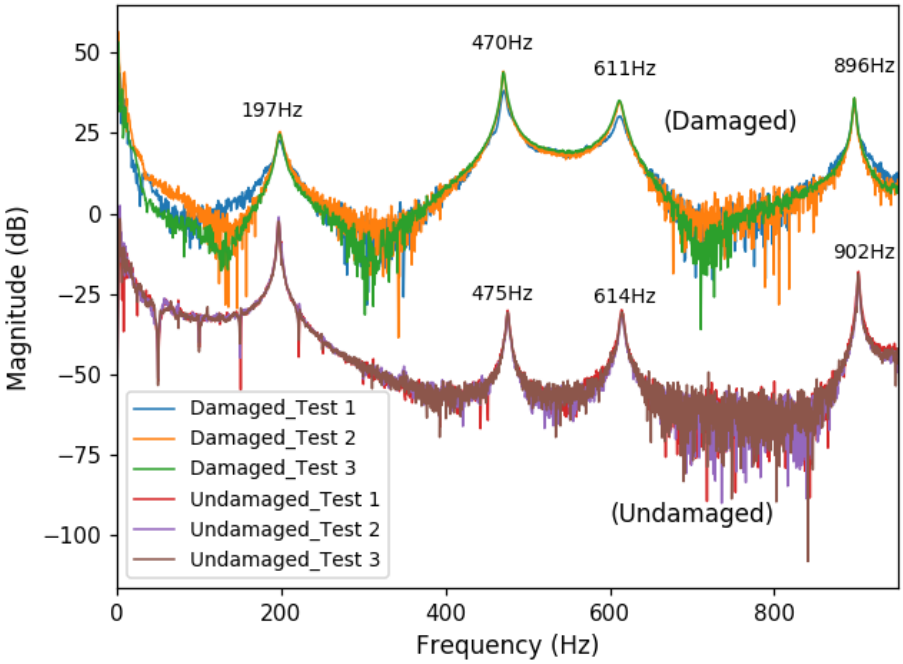

Figure 35: FRF of an undamaged and damaged laminated composite plates 0 dB =1 m/s/N

Figure 35 shows the frequency response functions (FRF) of the undamaged and damaged carbon/epoxy woven laminated plates, for both plates the tests were conducted three times to demonstrate repeatability.

Table 2: Summary of natural frequencies of undamaged and damaged laminated composite

Modes	First torsional mode (1st peak)	First bending mode (2nd peak)	Second torsional mode (3rd peak)	Second bending mode (4th peak)
Undamaged	197 Hz	475 Hz	614 Hz	902 Hz
Damaged	197 Hz	470 Hz	611 Hz	896 Hz

The frequency response function of the damage composite in Figure 35 was produced by the PSV 300 laser vibrometer, and the frequency response function of the undamaged composite was produced by the PSV 400 laser vibrometer. The difference in magnitude between the two FRFs may be attributed to the sensitivity values and the difference in settings between the PSV 300 and PSV 400. The FRF of the damage composite plate shows four distinct peaks which are similar in value to the peaks of the undamaged plate. Small shifts in natural frequencies are noticed above the frequency of 200 Hz. However, the change in the natural frequencies (Table 2) are not as much as expected so that damage can be affirmed with confidence. Kessler et al. (2002) demonstrated bigger shifts in natural frequencies above the range of 400 Hz than the ones obtained in Figure 35.

Chapter 3: Theory and evaluation of full field DIC

In this section of the research full field DIC preliminary experiments were performed on the laminated composites described in section 1.7. The same undamaged and damaged specimens used in the experimental modal analysis (chapter 2) were the subjects of the full field DIC experiments. Prior to the details of the experiments the theory of DIC is given. The full field DIC experiments were performed under static and dynamic loading conditions, the experimental setups were designed such that no addition damage would be induced.

3.1 The theory of full field DIC

As mentioned in the literature review, digital images contain very useful information which can be taken advantage of in the practical world. Full field DIC has been employed in a wide variety of fields including material testing, failure studies, health monitoring and of particular interest to this research deformation data of materials with complex compositions.

Digital image correlation tracks features in space and assigns them to a coordinate system by making use of the principle of photogrammetry, digital image processing and stereo imaging. Measurements using this technique are obtained by comparing numerous images of the externally excited specimen taken in series in a small time frame (microseconds). This optical measurement technique is able to measure the displacement on the surface of an object subject to external forces, the measured displacements (i.e. displacements or strains) are comparable to those obtained by numerical means.

3.1.1 Photogrammetry

Photogrammetry is defined as “a science of gathering reliable information about the properties of a surface or object without physical contact with the object, and of measuring and interpreting the information.” (Schenk, 2005).There are other definitions in literature and all are in agreement that the “reliable information” is captured through the process of recording the electromagnetic radiant energy patterns in the form of photographic images. This science can be divided into three stages: 1) Data acquisition, 2) Photogrammetric procedures, and 3) Photogrammetric products. The essence of photogrammetry is that the science enables determination of an object or point in three dimensional space from two-dimensional images of the object/point captured at different angles. This is achieved by setting up equation based on the ray from the cameras at different angles and their intersection points (Figure 36).

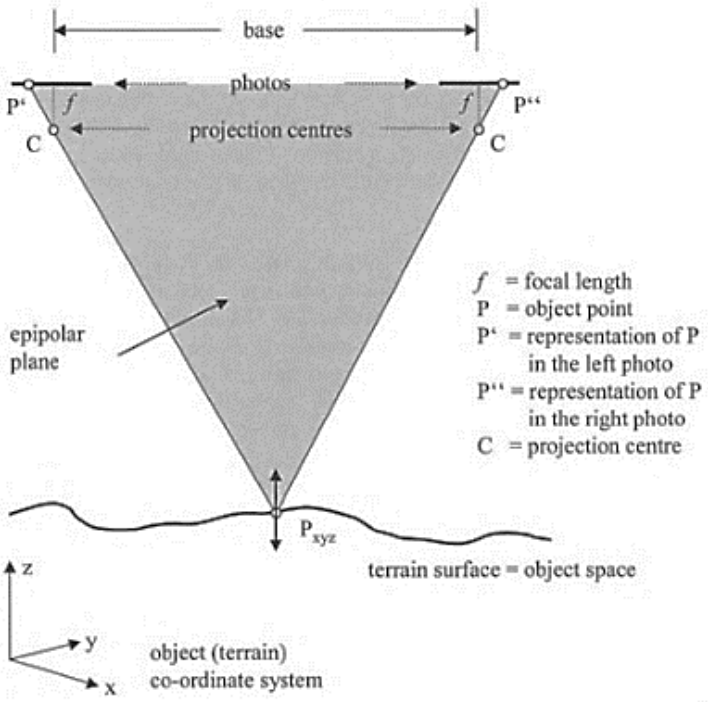

Figure 36: illustration of photogrammetry (Linder, 2003)

Data acquisition

This stage in the process of gathering information which can be in temporal form; which is information about the change of an object in time by comparing images of it taken at different times or physical forms. This refers to the electromagnetic properties of the object and the most important information which is the spatial position and shape of the object referred to as geometric information. This information is obtained by means of sensors which are digital cameras mounted on tripods. Digital cameras are advantageous in that they offer spectral flexibility and the images are instantly available for analysis.

Photogrammetric products

Photogrammetry can be classified into three categories namely, photographic products, computational results and mapping. The photographic products are the photos, derivatives of the photos and photos from multiple photos overlapping one another (i.e. Photo mosaics). Among successful applications of photogrammetry lies aerial triangulation which is able to produce the position of points measured on a photograph in three dimensions from a ground coordinate system. Such results are commonly applied in instances where cross-section data and profile is required. Maps from photogrammetry can be planimetric, topographic or thematic in nature.

Mathematical concepts

Direction and distance are the two fundamental measures required to derive the spatial position of an object or point on a surface. These measures can be obtained directly or indirectly, this study is concerned with the indirect method specifically from digital images. Measurements from images have their own reference states and it is frequently required in photogrammetry to perform coordinate transformation so as to bring points in communication to one another. The change in the coordinate system can be brought about by either changing the coordinate system while keeping the object stationary and assigning a new coordinate system to each and every point on the object (i.e. passive interpretation of the change in coordinate system), or changing the position of the object in space while the original coordinate system remains fixed (i.e. active interpretation of the change in coordinate system). There are 3 fundamental coordinate transformations in photogrammetry which can mathematically be expressed in two-dimensional space as:

- Scalar change; in which the original coordinate system is multiplied by a scalar transforming it into a new coordinate system.
- Rotating the original axis by a certain angle.
- Translation of the original axis by the addition of a scalar.

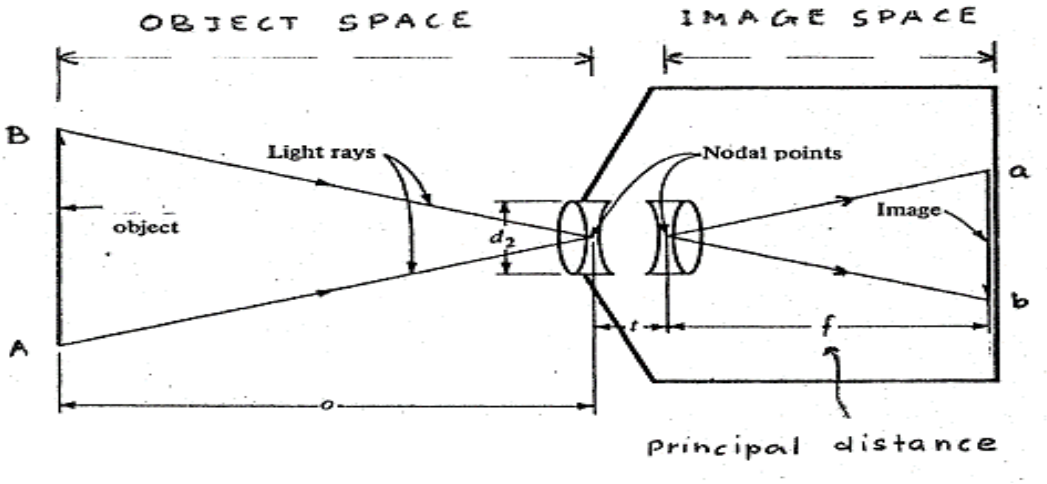

Figure 37: Photographic camera nodal points (Derenyi, 1996).

As mentioned above the primary tool of data acquisition in photogrammetry is the camera, as such it critical to comprehend the geometry that comes about from the formation of an image in camera. Cameras have interior and exterior projection centers at the rear and front nodal point of the objective lens respectively. The rays coming for the object intersect at the front nodal point and diverge toward the image plane at the rear nodal point, Figure 37 depicts the nodal points as well as the image and object space.

An important geometric quantity of the camera is the principal distance; it is the distance between the perspective centers to the image plane. The image plane in cameras manufactured for photogrammetry purposes possess four or more fiducial marks (reference marks).

A single image of the object in space is not sufficient for the reconstruction of the spatial existence of an object in three dimensional space. Only the direction of the ray which runs from the perspective center through an image point to the object point can be improved from a single image. In order to fully resolve the spatial reconstruction problem, secondary images taken from a different angle must be available or the third dimension of the object point must be known. When a second image is available (this is almost always the case) the collinearity equations can be solved simultaneously to determine the space coordinates of the point in an image. From knowledge of the third dimension comes the process of rectifications in which the image coordinate system is not parallel to the object space coordinate system. The image is then transformed into an equivalent one with coordinates parallel to the object.

3.1.2 Stereo imaging

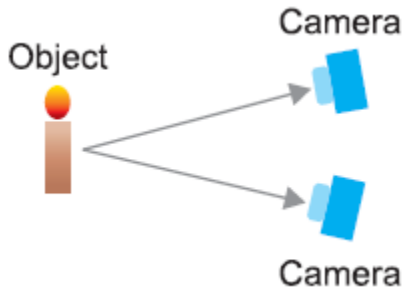

Figure 38: Parallel camera system (Won Nam et al., 2012)

Stereo imaging comes from the biological term of stereopsis which is defined as the ability to perceive the depth dimension of objects as viewed by both eyes (Poggio et al., 1984). Stereo imaging or rather a stereoscopic system in photography consists of two or more cameras positioned to capture an image of the same object at different angle to enable depth reconstruction of the viewed object (Won Nam et al., 2012).

There are different kinds of stereoscopic system but parallel-camera and beam splitter systems are the ones which are commonly used. For this research the parallel camera system was used for all full field DIC investigations. The Aramis GOM system was used for static loading conditions and Motion Studio for high speed cameras was used for dynamic loading. In the parallel camera structure as the name suggests two cameras are placed side by side just like the arrangement of the human eyes (Figure 38). This camera arrangement presents the convenience of making adjustment to the settings in order to match alignments and results in no difference between the two images in terms of light exposure and color.

3.1.4 Principles of DIC

Digital image correlation requires a software which is able to process the images as desired. Understanding the mathematical principles behind the processing is a vital part in applying the technique in experiments. Digital images are made up of pixels one of which is the smallest single unit of the digital image. Using a numeric pixel array a two-dimensional graphic image can be stored. The position and value of any pixel can then be expressed by the use of a matrix indexing (Chang et al., 2015). In this way the entire image is expressed as a matrix whose elements are pixels which can be identified as: $DI(r,c)$ where 'DI' is the Digital Image matrix and 'r' is row location of the pixel and 'c' is the column location of the pixel. By convention the origin of the planar coordinates is set at the upper left corner of the image. This sort of mathematical representation of the image enables establishment of the location vector of each pixel and additional images of the same feature enable tracking of these vectors.

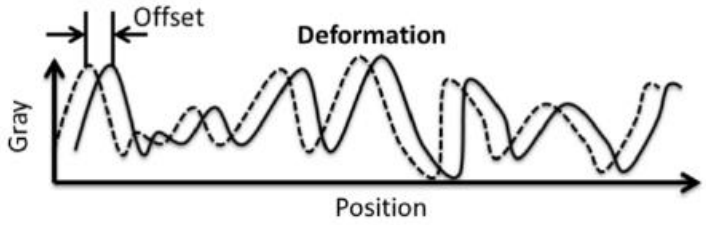

Figure 39: Schematic of feature image deformation (Chang et al., 2015)

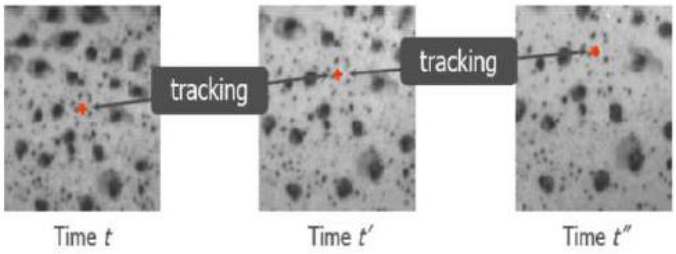

Figure 40: Spot tracking in a continuous image (Chang et al., 2015)

When the surface features of the object are unvarying and ordered the effective analysis of the moving vectors of the features becomes more challenging. The ideal surface is said to be the one which is messy and irregular as it will yield good positions when the specimen deform. Figure 39 shows a gray scale of the intensity curve of the spatial coordinates when a surface feature full of irregular spots deforms. By determining the offset in the curves using DIC spots in a continuous image can be tracked (Figure 40).Digital Image correlation applies the deformation theory of solid mechanics to define the displacement and the strain of an element (i.e. pixel) at any instance in time given the original location of the element.

Digital image correlation applies the deformation theory of solid mechanics to define the displacement and the strain of an element (i.e. pixel) at any instance in time given the original location of the element in the manner described below:

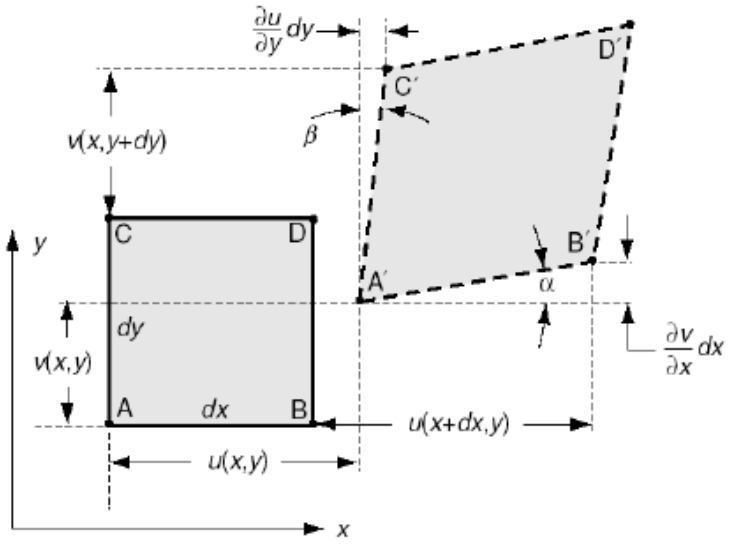

Figure 41: Element (pixel) displacement and strain after deformation (Chang.et al, 2015)

Working on an element level depicted in Figure 41 dx,dy, u and v are the width, length, displacement in the x and y direction respectively, and the angular deformations α and β. DIC employs an algorithm which makes iterations involving these six variables at a specified clearance. The clearance becomes gradually refined as the computations proceed until all the variables converge and the displacement of the best subset image is obtained in the specified region of interest. The strain which is the elongation divided by the original length of the specimen can be expressed as:

$$\varepsilon_x = \frac{A'B' - AB}{AB} = \frac{du}{dx} \ \ (i.e.\, strain\ in\ the\ x\ direction)$$

$$\varepsilon_y = \frac{dv}{dx} \ \ (i.e.\, strain\ in\ the\ y\ direction)$$

$$\gamma_{xy} = \frac{du}{dx} + \frac{dv}{dx}\ (i.e.\ shear\ strain)$$

DIC the uses the deformation data in conjunction with failure theories such as the von Mises strain theory to produce strain fields in in two and three dimension according to the formula

$$\varepsilon_e = \frac{2}{3}\sqrt{\frac{3(\varepsilon_x{}^2 + \varepsilon_y{}^2 + \varepsilon_z{}^2)}{2} + \frac{3(\gamma_{xy}{}^2 + \gamma_{yz}{}^2 + \gamma_{zx}{}^2}{4}}$$

3.1.5 Full field DIC arrangement

This section looks into the application of DIC setups for deformation measurements on various materials, as well as the difficulties which can be encountered in obtaining accurate results.

Stress and strain results from a uniaxial tensile test on aluminum using DIC is shown in Figure 42(a) (Gadhe and Navthar, 2016). A single Sony T2 ultra 16:9 aspect ratio high speed camera was used to capture the deformation every 3 seconds from the onset of the loading till failure of the material. A total number of 280 images were taken within the time it took the specimen to fail. Digital Image processing and correlation was performed using MATLAB software image processing tool which has the capability to add, subtract and detect the differences between two or more images.

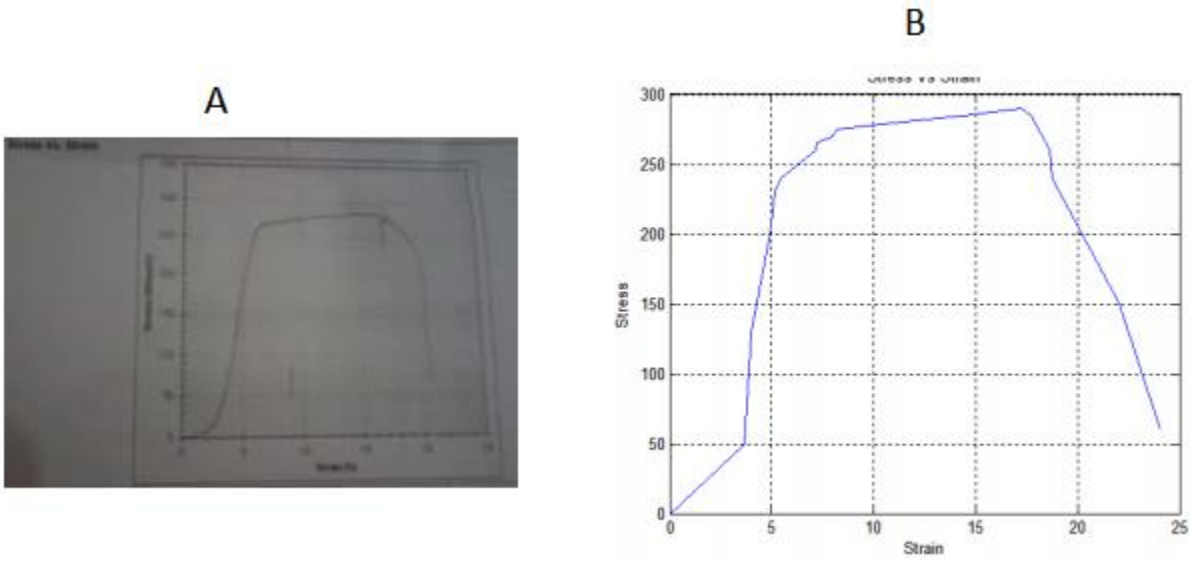

Figure 42: Stress strain curve results: (A) from tensile test machine, (B) from DIC (Gadhe and Navthar, 2016)

The MATLAB DIC tool converts the RGB image to gray and then from gray to binary. It then crops the selected target area and inverts it in order to measure speckle area and calculate correlation factors, entropy, variance and standard deviations. It then calculates elongation followed by strain percentages and graphs the results as the output. Figure 42(b) shows the similarity in the stress-strain curves between the uniaxial tensile test machine and DIC. A 22% strain was obtained from the tensile test and 24% from DIC. As this was a simple tensile test only a single camera was required, for critical components and material with complex composition a multi-camera DIC technique will yield more accurate results.

A unique digital image correlation system which makes use of multi-cameras was proposed by Chen et al. (2013) for full field DIC. In their proposed system multiple cameras are calibrated to act as a single system. Based on the fundamentals of triangulation two cameras can be paired to measure a part of a three dimensional object.

The captured data from the different pairs of cameras can then be mapped into a universal coordinate system based on the calibration data. Based on the contours of the object at different times deformation data can be obtained. In their experiment four synchronized Charged Couple Device (CCD) cameras were used to test the performance of the system in a static and dynamic scenario (Figure 43) arranged in a stereovision system.

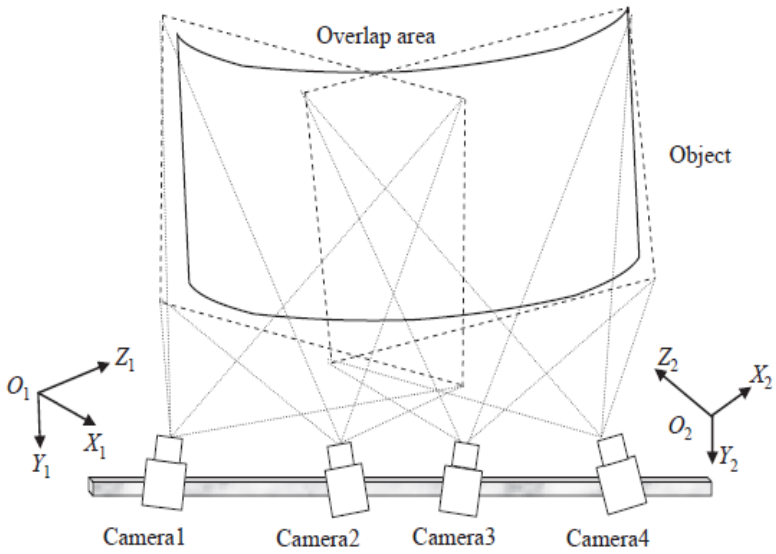

Figure 43: Measurement system of DIC using 4 CCD cameras (Chen et al., 2013)

Stereovision matching was used to match the four speckle patterns on the same object surface, which is captured by the left and right pair of cameras at different angles prior and post to deformation. The matching can be done by minimizing a function that has information about the pixel intensity from the image and correlating intensity values of the subsets till the function is minimized.

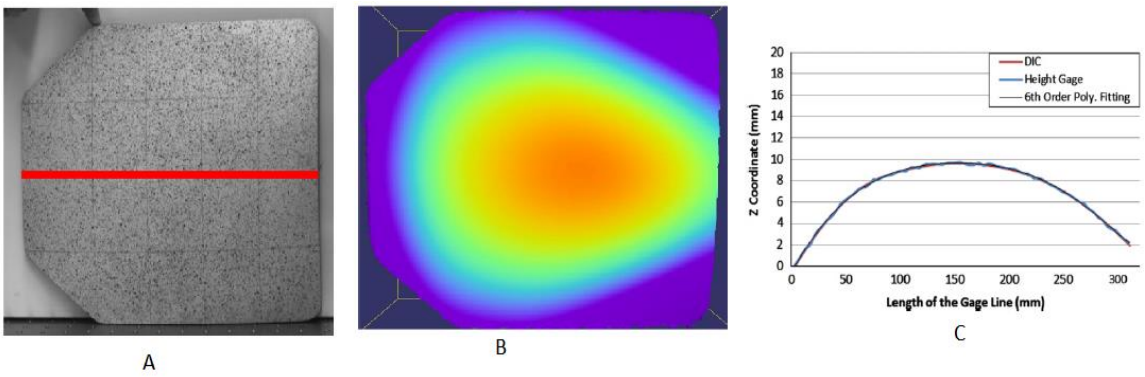

Figure 44: (A) Actual curved plate with a gauge line, (B) Full field 3D image, (C) Z coordinate vs length of the gauge line plot comparing DIC, height gauge and a 6th order polynomial fitting (Chen et al., 2013)

The performance of the technique was exceptional as indicated by Figure 44(c) which shows the comparison in accuracy of the DIC against actual measurements of the shape of a curved plate using a height gauge. In their dynamic analysis to test how well the technique captures deformation was conducted using an industry shaker, the frequency of the shaker was set to 1 Hz with an amplitude of 0.02mm for the dynamic load to the flat aluminum sheet.

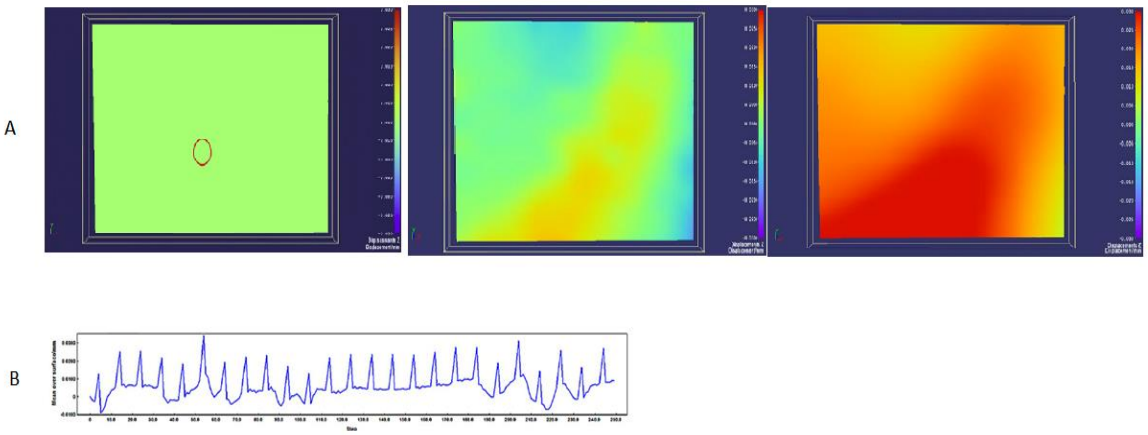

Figure 45: (A) Out-of-plane deformation with dynamic loading, (B) Out-of-plane deformation plot of the area in the red circle (Chen et al., 2013)

Their results indicate that the method is able to capture small and large out-of-plane deformation as shown in Figure 45. Their results also shows the plot of the averaged deformation data from the area indicated by the red circle Figure 45(b). Not only does the DIC technique capture deformation well, it can also provide information regarding the vibrations from the maximum recorded displacement, of which was 0.02mm the same as that of the amplitude of vibration.

Promising as the technique may be there are potential errors which can be incurred. The technique is largely dependent on the symmetry and stability of the arrangement. Should either one be lost the 3D measurements among the cameras will be inconsistent with one another and adversely affect the overall evaluation.

3.2 Procedure of the ARAMIS GOM DIC system camera calibration

The full field DIC experiments in this research were conducted using the Aramis GOM DIC system. The system makes use of parallel stereo imaging discussed in section 3.1.2. The first full field DIC experiments are conducted to evaluate the Aramis GOM DIC system.

Figure 46 shows a schematic of the Aramis GOM DIC parallel camera configuration which is the same as the stereo imaging described by Won Nam et al. (2012). Two 20 mm lens cameras were used for the experiments. The Aramis GOM optical measuring software was used for the analysis of the captured images. For a measuring volume of 350 by 260 a tripod on which the cameras were mounted had to be placed 480 mm away from the test subject as per the manual.

The slider distance i.e. the distance between the cameras from the center of the slider, was set to 186 mm which resulted in a camera angle of 25°.The camera angle is crucial as it determines the accuracy of out-of-plane resolution measurements.

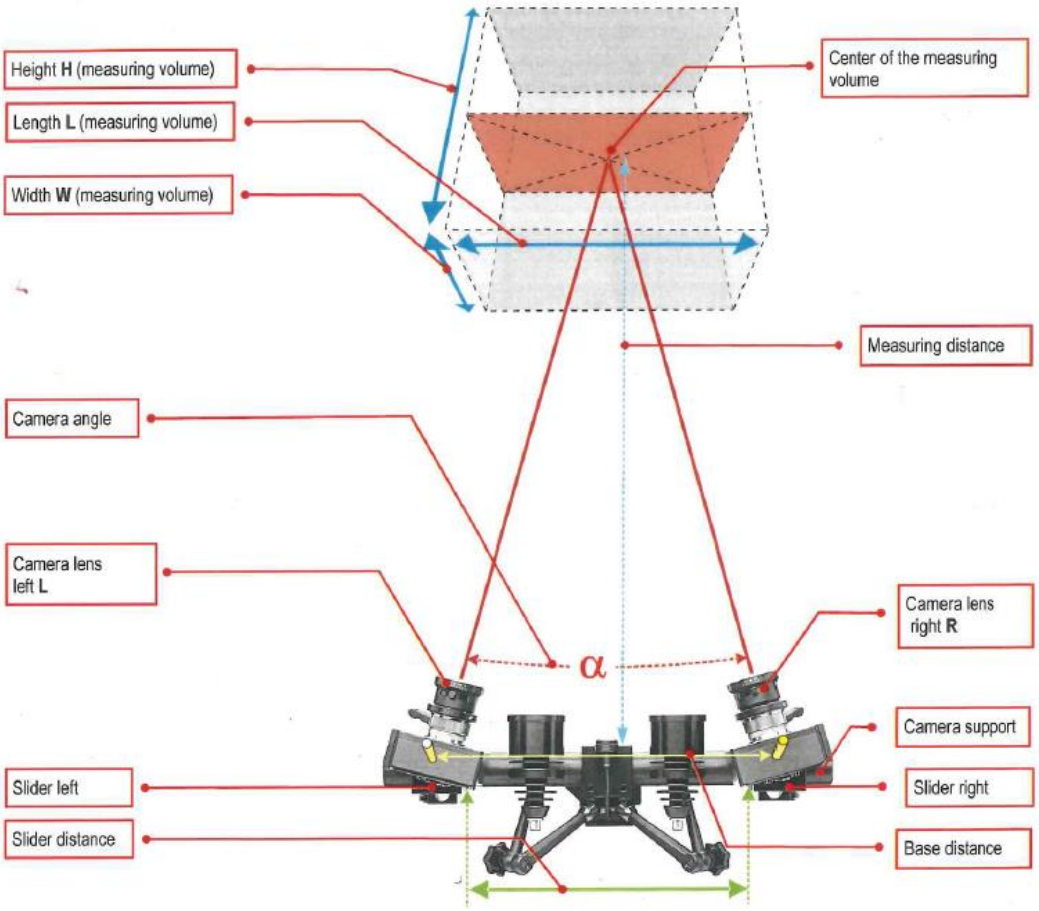

Figure 46: full field DIC setup schematic (Aramis manual. 2009)

The two camera setup determines the two dimensional coordinates of the facets from the corner points and center of the green facets (Figure 47). Making use of the method of photogrammetry the two dimensional coordinates of a facet that is observed by the left camera and right camera lead to a common three dimensional coordinate.

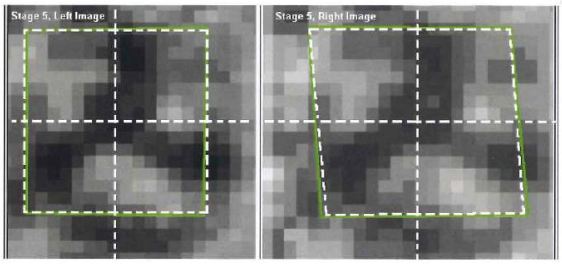

Figure 47:15x15 facets of the left and right camera in the final displacement stage (Aramis manual. 2009)

3.3 DIC rigid body motion experimental setup and camera calibration

In this section the full field DIC of the Aramis GOM system is evaluated. The system was used to measure rigid body motion and the results were compared to those obtained using independent methods. The full field DIC was used to measure forward movement of an object as it was moved a set of distances by a micrometer.

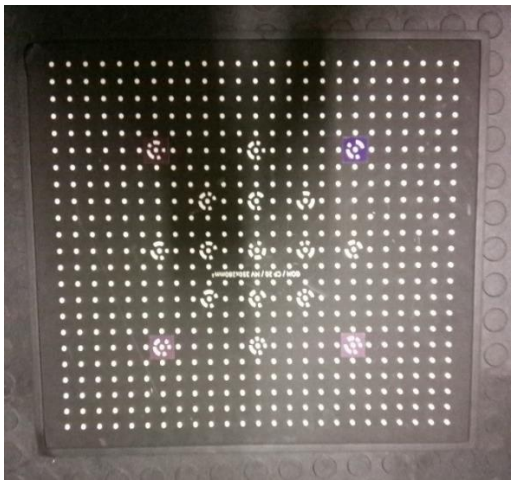

(a) Calibration panel with 17 main points

(b) Calibration setup with calibration panel placed 480mm from GOM cameras

Figure 48: Calibration setup: (a) shows the calibration panel, (b) shows camera and calibration panel setup

Figure 48 shows the camera setup for calibrating the GOM cameras. The cameras were mounted on a slider which is equipped with a laser to aid with centering of the cameras. Once the adjustments of the lenses and lights rendered images with sufficient contrast the cameras were calibrated using a calibration panel with two scale bars.

The panel was magnetically supported on its own tripod which had to be placed a measuring distance 480 mm away from the cameras for calibration. A calibration distance of less or more than the measuring distance of 480 mm would lead to inaccurate measurements. The panel was positioned such that the vertical cross hairs intersected with the laser point in the image of the left and right camera.

Calibration was carried out with instructions using the Aramis software and it is necessary in order to determine the distance and orientation of the cameras to each other, as well as the image characteristics of the lenses. Based on the settings such as lens distortion and focus, the software calculates the three-dimensional coordinates from the reference point of the calibration panel in the two-dimensional camera image. Multiple images of the calibration panel were taken at different angles and positions with all 17 main points on the panel captured by both cameras. Main points visible in the captured image of one of the cameras and not the other would lead to a high calibration deviation value in the calibration results.

The calibration deviation is computed from the average reference point deviation of all main dots recorded during the process of calibration and should be between 0.01 and 0.07 pixels (Aramis, 2009). A calibration deviation value larger than 0.07 leads to incorrect scale parameters, a calibration deviation in the range of 0.47 to 0.66 was obtained in the experiments. During the calibration of the cameras under the GOM instructions a single image of the calibration board is taken by each camera in the described positions:

- 480 mm away from the cameras (i.e. normal position).
- Placed close to the cameras (less than 480 mm).
- Placed far from the cameras (greater than 480 mm).
- Placed in the normal position and tilted 40º, and the rotated 180º.
- The board placed in the normal position facing the right camera and rotated from 0º to 360º, and the same repeated for the left camera.

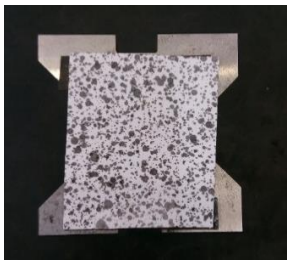

Figure 49: Rigid body motion test piece

The first test conducted with full field DIC after calibration was to check how accurate the system was in measuring rigid body motion. The specimen shown in Figure 49 was a square cut out of a white sheet of hard paper, the speckles were sprayed on using matt black paint in a scattered pattern. The application of black scattered speckles on a white background on the specimen is an essential step in a full field DIC experiment. The position of each speckle is tracked from the first captured image to the last one. Using the deformation theory of solid mechanics the change in speckle position as the specimen deforms is used to compute deformation data such as strain and displacement fields. The specimen was attached to a piece of steel with double sided tape.

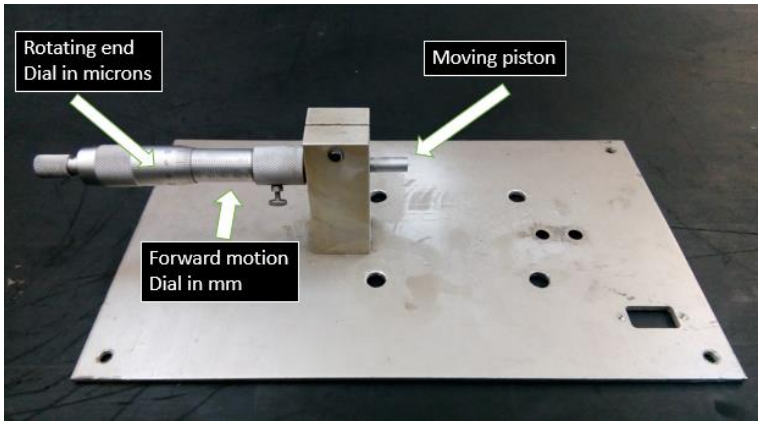

Figure 50: Micrometer

A Micrometer was used to move the steel piece forward as shown Figure 50. The micrometer operates by rotational movement measured in microns on the one end which in turn causes forward movement of the other end. One revolution of the rotating end of the micrometer moves its piston half a millimeter forward.

Figure 51: Experimental setup for rigid body motion tests

The micrometer was attached to a solid steel frame with magnets to prevent motion during the experiment (Figure 51). The steel piece was placed on top of a wooden block and a sheet of white paper served to reduce friction between the steel and wood which would cause unwanted rotation of the steel piece as it was pushed forward. To further limit any rotation the piston end of the micrometer was placed to push the steel at its center point. The test piece was the place 480mm away from of the cameras at the start of the experiment.

3.4 Results of full field DIC and micrometer for rigid body motion accuracy tests

Eight displacement readings were taken of the micrometer pushing the test piece forward, which was reset to zero after each test. A time delay of 3 seconds was set between the captured images as the test piece moved forward to the required displacement. A total time period of 2 minutes was set for each displacement measurement, this duration was much longer than the time it took to move the test piece to the required displacement. In this manner the final known displacement from the micrometer was captured in the last image since the cameras continued to record long after the test piece reached its displacement.

Figure 52 and Figure 53 show the full field DIC result compared to the measurement from the micrometer for small and large displacements respectively, also presented graphically in Figure 54 showing a linear behaviour. The full field DIC was used to measure movement of the object from a reference position to the final position governed by the micrometer.

The measurements received from full field DIC analysis which shows displacement measurements in the forward direction (+z axis) are very similar to those measured by the micrometer for small and large displacements.

The displacement fields from the DIC results show slight rotation of the sides of the test piece for both small and large displacements. The slight rotation of the different sides in the experiments can be attributed to slight changes during resetting of the test piece for the next experiment. Also any slight unevenness of the surface of the micrometer piston may have contributed since its forward movement is accompanied by rotation.

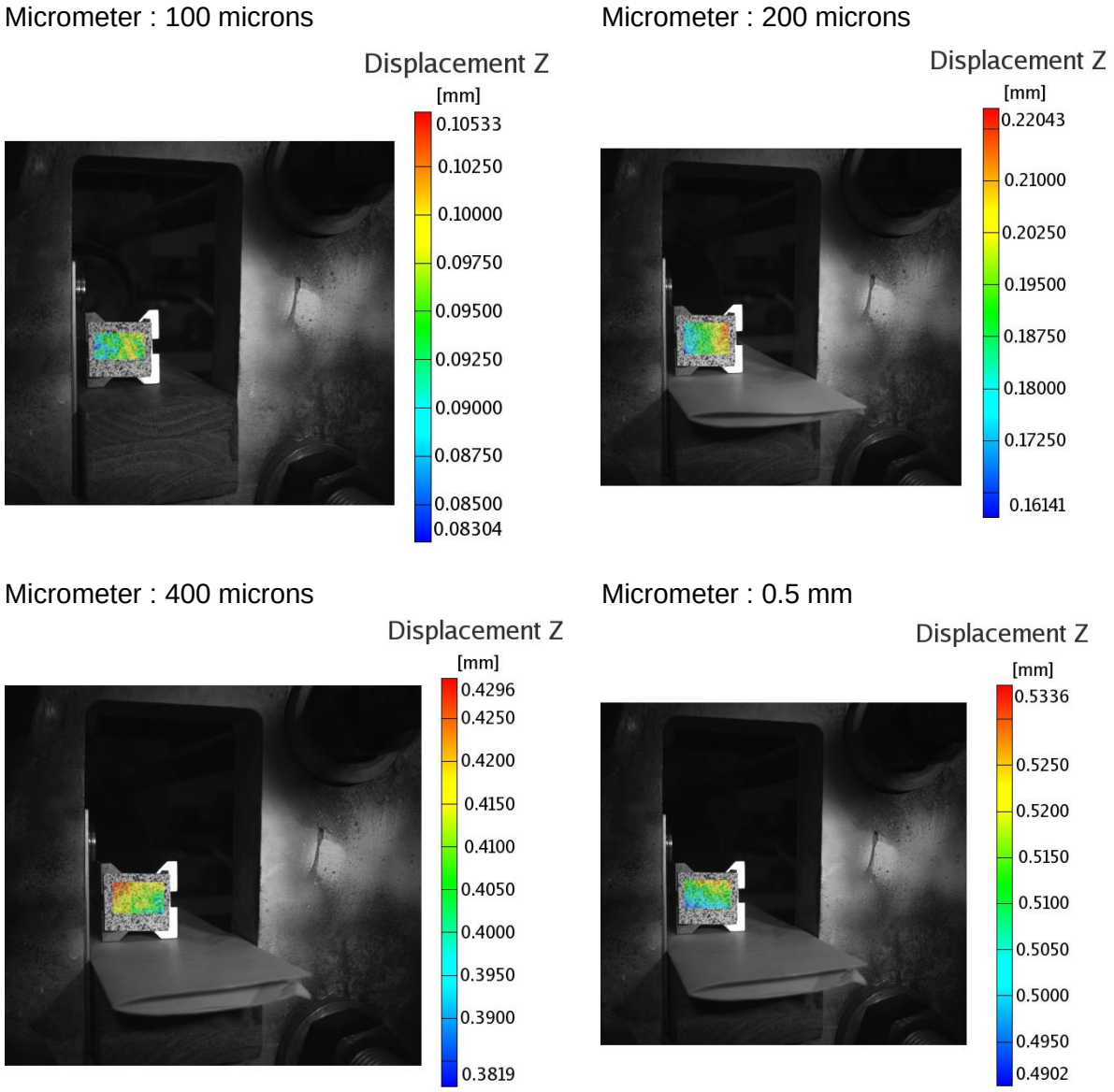

Figure 52: Full field DIC and micrometer results for small displacements

Micrometer :1 mm

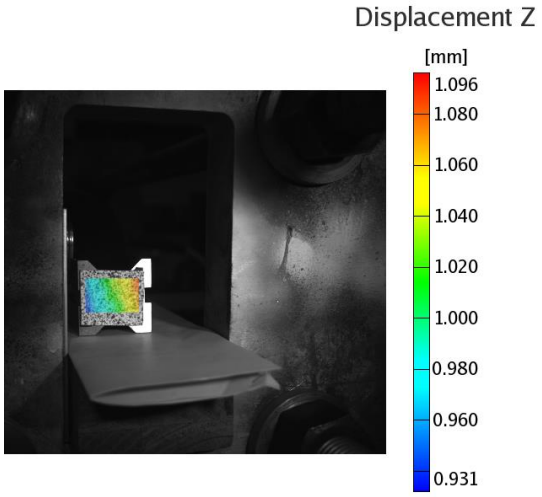

Micrometer : 1.5 mm

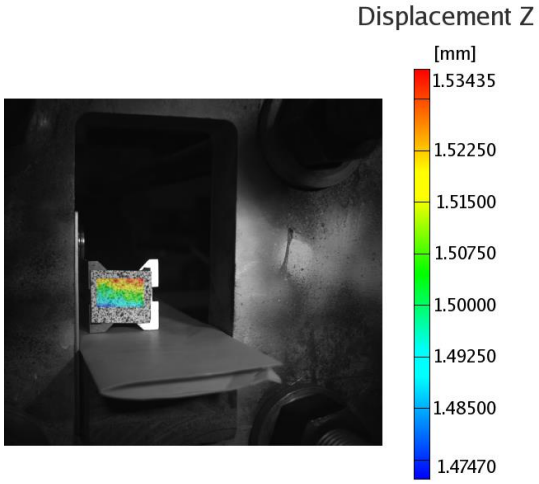

Micrometer : 2 mm

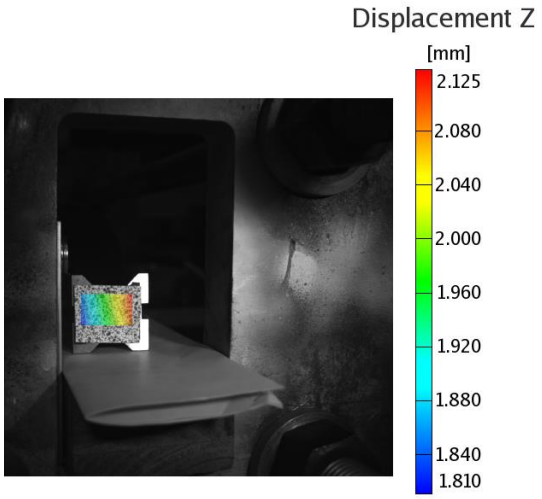

Micrometer : 2.5 mm

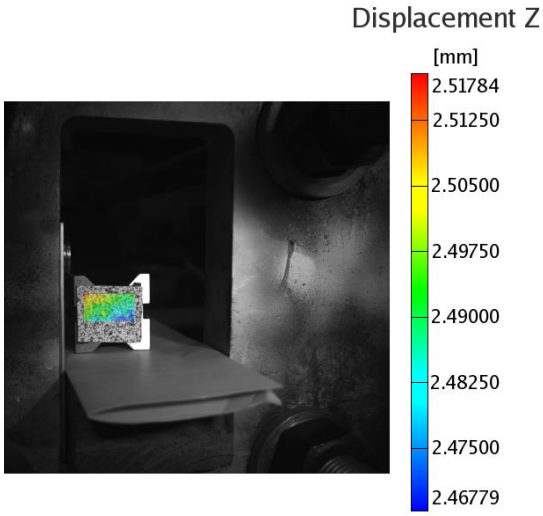

Figure 53: Full field DIC and micrometer results for large displacements

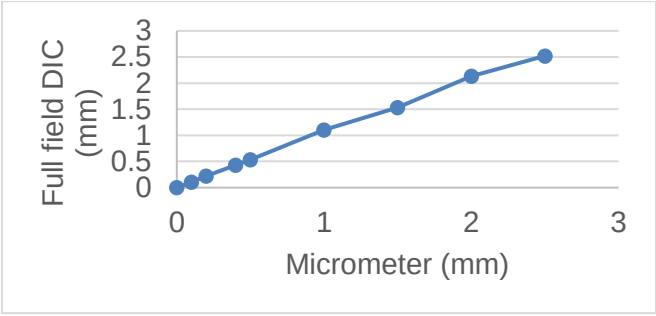

Figure 54: Graphical representation of full field DIC and micrometer results

3.5 Full field DIC out-of-plane displacement experimental setup and calibration: comparison with eddy current probe

Full field DIC was used to measure out-of-plane deformation of a steel plate subjected to a point load. The results were compared to the reading captured by an eddy current probe during deformation.

3.5.1 Theory of eddy current probe

Eddy current probes are non-contact measuring instruments capable of taking high resolution measurement of position or change in position of a conductive structure. Their operation is based on the principles of interaction between magnetic fields and current (Lion Precision, 2019). A drive source sends alternating current to the sensing coil located at the tip of the probe which then creates an alternating magnetic field. When the probe is placed near the target surface the magnetic field induces small currents in the target, the small currents are referred to as eddy currents. The small eddy currents create an opposite magnetic field which opposes that generated by the sensing coils in the probe. The communication between the two magnetic fields strongly depends of the distance between the target material and the probe. As the distance between the target and the probe changes so does the interaction between the magnetic fields. The change in the magnetic field interaction is sensed by electronics which produce a voltage output that is proportional to the change in distance between the target and the probe.

3.5.2 Calibration of the eddy current probe

An NI8-M18-LIU eddy current probe (Figure 55) was used in the experiment and calibrated using a micrometer.

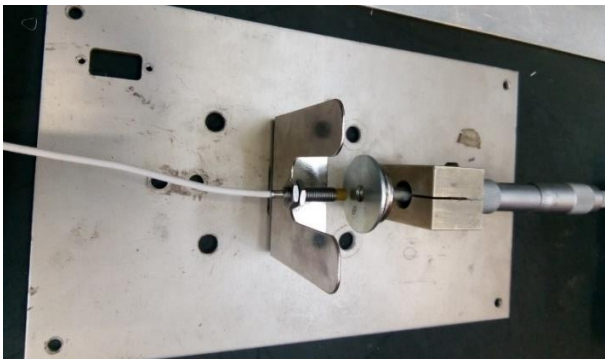

Figure 55: Eddy current probe calibration setup

For full stability the probe was attached to a steel support using its fixtures. The steel base supporting the probe was attached to the base plate of the micrometer with double sided tape. A circular steel plate was attached to the moving end of the micrometer to serve as the target.

The output voltage as the distance between the probe and the target surface on the micrometer is shown in table 3. The data was used to generate a calibration graph (Figure 56) for converting voltage to displacement data.

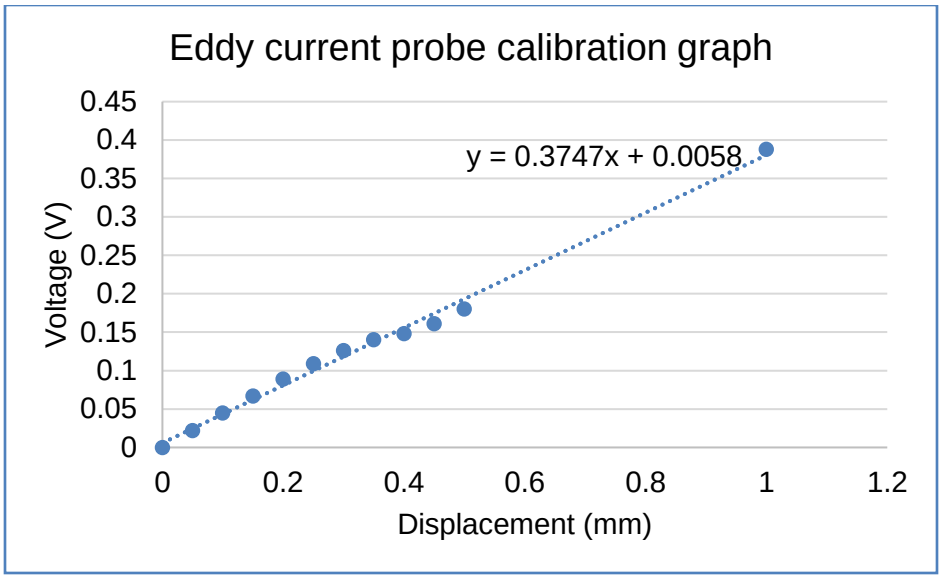

Figure 56: Eddy current probe calibration graph

From the data distribution in Figure 56 a second order polynomial seems to best fit the data below 0.6 mm. However, a jump to the last data point provides a better prediction of the distribution as the displacement increases and thus a linear function best represents the data in table 3 covering the data points. Since eddy current probes are very sensitive to movement the imperfectness of the linear fit on the graph can be attributed to manual operation of the micrometer and slight vibration during calibration.

Table 3: Eddy current probe output voltage

Target surface displacement(mm)	Output voltage(V)
0	0
0.05	0.022
0.1	0.045
0.15	0.067
0.2	0.089
0.25	0.109
0.3	0.126
0.35	0.14
0.4	0.148
0.45	0.161
0.5	0.18
1	0.388

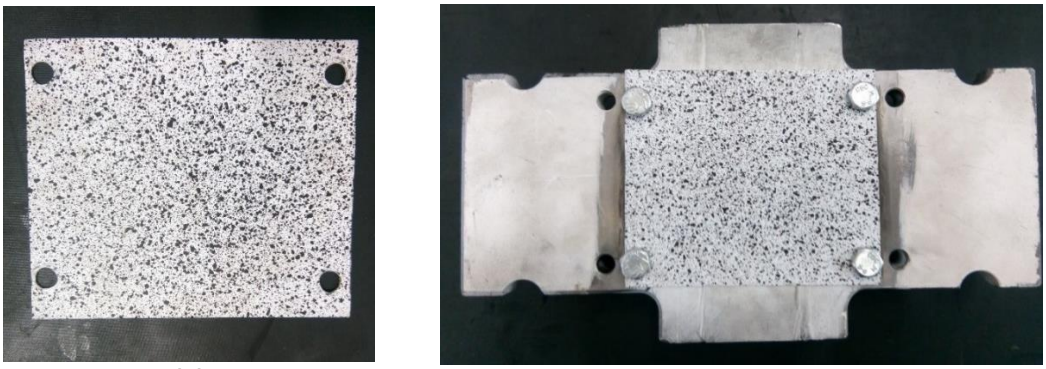

(a) (b)

Figure 57: Target steel plate for eddy current probe: (a) shows the steel plate, (b) shows the steel plate attached to the holding plate

Figure 57(a) shows the 156 mm x 133 mm x 1 mm steel plate that was the subject of the point load test. The surface of the plate that was prepared by first cleaning it with acetone followed by four coats of matt white spray paint. A scattered black dot pattern was applied using matt black spray paint to provide the speckles for tracking. This is shown in Figure 57(a), the test piece was attached to a holding plate by M10 bolts at the corners, shown in Figure 57(b).

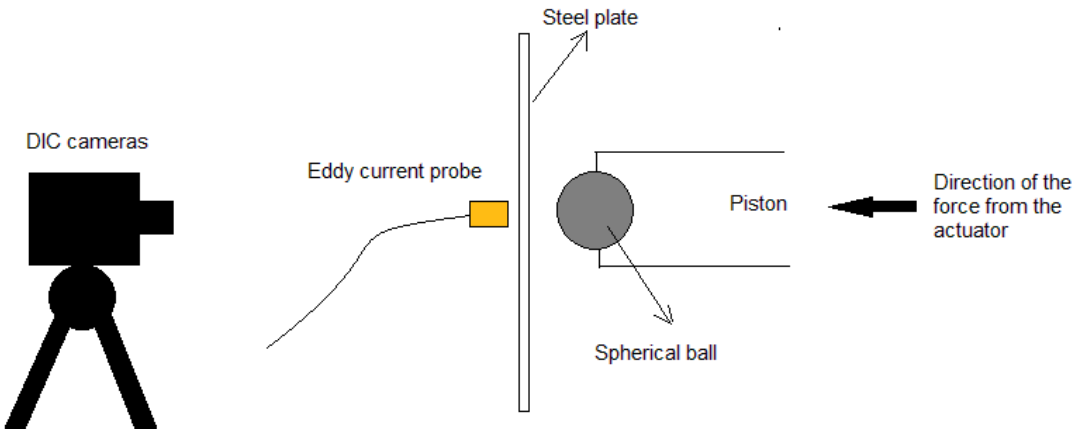

Figure 58: Schematic representation of the experimental setup for out-of-plane measurements with the eddy current probe

Figure 58 shows a simplified schematic of the experiment for measuring out-of-plane deformation. Figure 59 shows the actual experimental setup that was used to conduct the experiment. It is a simple test apparatus designed to hold the specimen against a rectangular opening when the holding plate is bolted on the steel frame. The opening exposes an area of interest (220mm x 110mm) to the full view of the full field DIC cameras.

A pneumatically operated actuator was used to generate the force delivered to the back face of the specimen via a piston and spherical (30mm in diameter) ball located inside the holding plate. The probe was taped to the fixtures of a magnetic base for stability and positioned a distance away from the center of the target (i.e. the load application point) at zero voltage reading. The camera calibration procedure explained in section 3.2 and 3.3 was followed for this experiment.

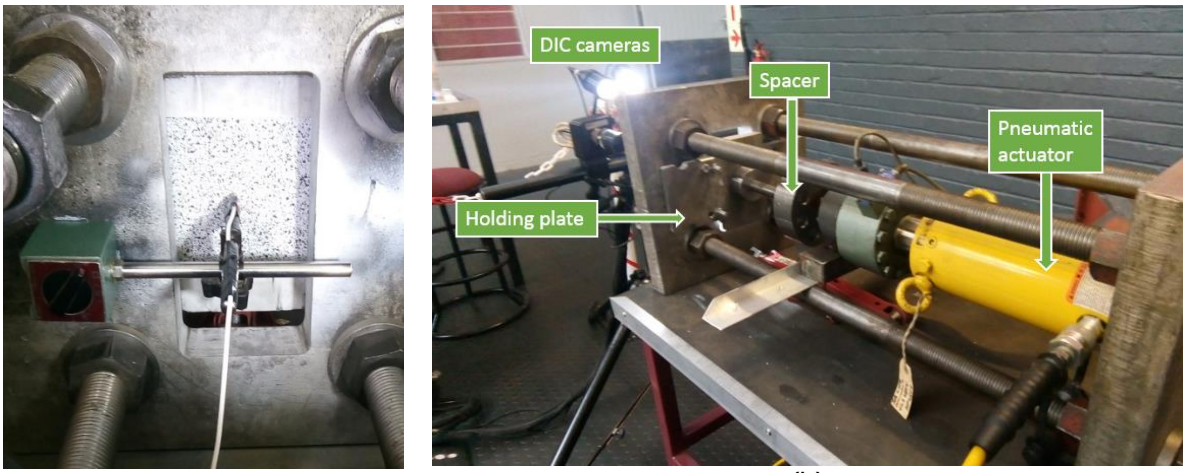

(a) (b)

Figure 59: Eddy current probe experimental setup: (a) shows the eddy current probe and the specimen exposed to the cameras, (b) shows the experimental setup

3.6 Results of full field DIC and eddy current probe for out-of-plane deformation accuracy tests

The results obtained from full field DIC measurements are in very good agreement with the independent measurements from the eddy current probe (Figure 61). Since the eddy current probe was placed in front of the cameras only the pixels defining the upper portion of the steel plate could be analyzed. Since the plate is symmetrical the lower portion of the displacement field can be assumed to be identical to the top.

The maximum out-of-plane displacements reported by DIC are measured very close to the location of the probe. The difference in the percentage error can be attributed to the calibration of the probe since the linear approximation of the data distribution is not a fully perfect fit but an approximation. Slight vibrations of the probe may have also contributed to the obtained error percentage. From the results for rigid body motion tests and the out-of-plane measurements in this section, it can be concluded that full field DIC is capable of fairly accurate out-of-plane displacement measurements as also demonstrated by the fairly linear behaviour in Figure 60.

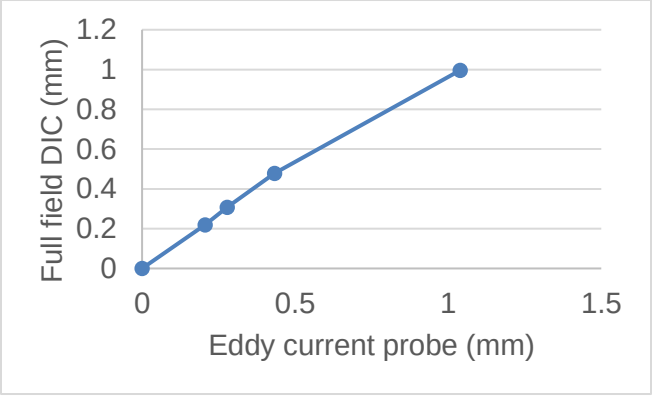

Figure 60: Linear behaviour of full field DIC and eddy current probe results

Eddy current probe: 0.083v **(0.206 mm)**

DIC +Z-displacement: 0.219 mm
Error: 6.3%

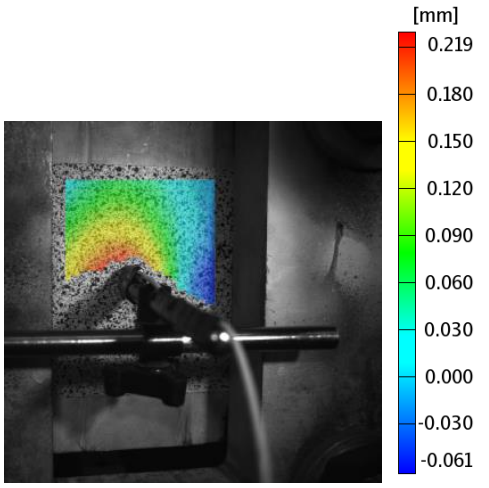

Eddy current probe: 0.110v **(0.278 mm)**

DIC +Z-displacement: 0.307 mm
Error: 10.4%

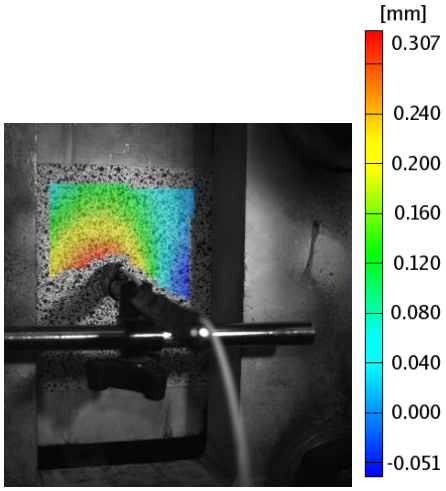

Eddy current probe: 0.168v **(0.433 mm)**

DIC +Z-displacement: 0.4789 mm
Error: 10.6%

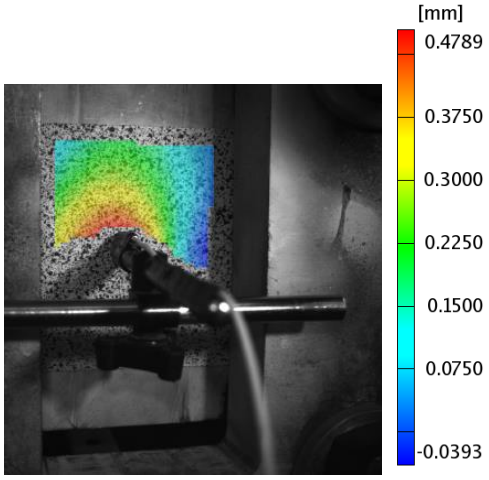

Eddy current probe: 0.395v **(1.039 mm)**

DIC +Z-displacement: 0.996 mm
Error: 4.1%

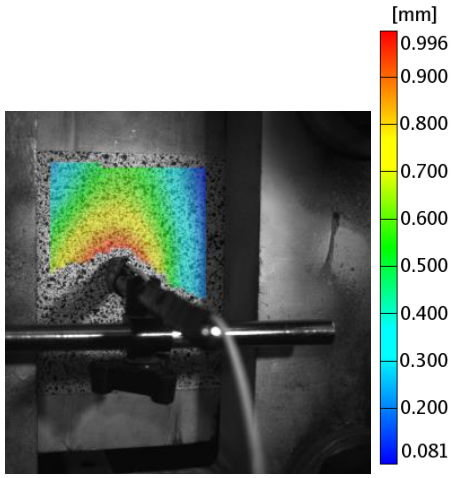

Figure 61: Shows four experiments measured simultaneously by the eddy current probe and full field DIC

Chapter 4: Preliminary investigation of full field DIC for damage detection in laminated composites

After evaluating full field DIC in measuring rigid body movement and out-of-plane deformation, the focus narrows in this section to out-of-plane displacements of laminated composite plates subjected to static and dynamic loading. The out-of-plane data will reveal whether full field DIC can distinguish between an undamaged and damaged composite, bearing barely visible damage induced from point loading.

4.1 Full field DIC experimental setup for static loading conditions

The same setup used for the eddy current test was used in this section with an addition of a 200 kg load cell connection to the system for force measurements from the actuator (Figure 62). The setup was designed to apply point loading at the center of the specimen.

(b)

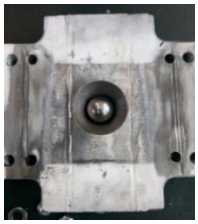

(c)

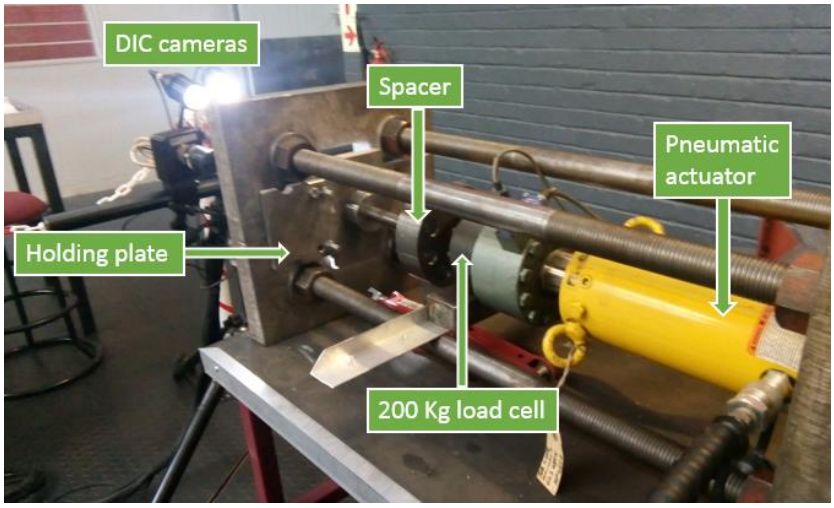

(a)

Figure 62: Experimental setup for full field DIC on a laminated composite subjected to point loading: (a) shows the labeled experimental setup, (b) shows the view of the specimen exposed to the cameras, (c) shows the 30 mm diameter spherical steel ball located inside the holding plate

Figure 63 shows the same undamaged carbon/epoxy woven laminated composite as used in the modal analysis experiments. The original dimensions of the composite specimen were reduced from 183 mm x 133 mm x 2.5 mm to 156 mm x 133 mm x 2.5 mm in order to fit the holding plate. 10.3 mm holes were made on the composite panels for the M10 bolts used to fix them to the holding plate. For surface preparation both the undamaged and damaged composite panels received 3 coats of matt white spray paint. The undamaged panel was painted by scattered black dots (speckles) applied using a matt black spray paint. A scattered black dot stencil was applied to the damaged panel. A speckle generator software was used to generate the speckles with a diameter and density of 0.05 inches and 75 % respectively. The generated speckles were printed out on A4 sized printable tattoo paper. The adhesive side of the printable tattoo paper was placed on the specimen, and the other side of the paper was damped with water using a wet cloth and then gently removed, leaving only the speckle pattern on the specimen.

The use of a stencil presents the opportunity to eliminate manual painting of the speckles using matt black spray paint for cases in which numerous specimens are to be tested. The same camera calibration procedure followed for the rigid body and out-of-plane accuracy tests (section 3.2 and 3.3) was followed in these experiments.

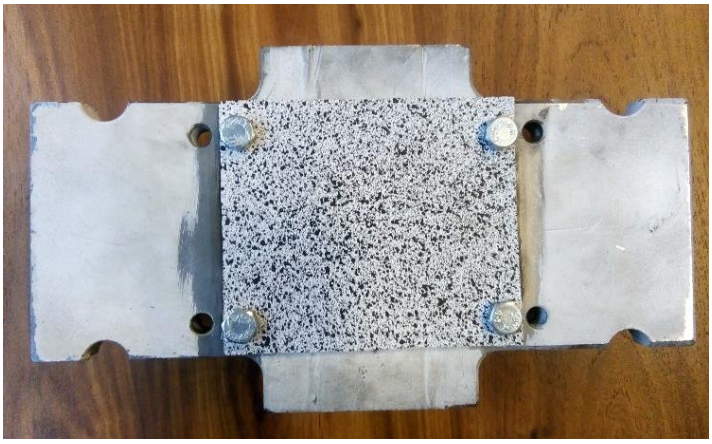

Figure 63: Undamaged laminated composite plate surface prepared for full field DIC experiment

4.2 Calibration of the 200 kg load cell

The 200 kg load cell was connected to the full field DIC Aramis GOM system via a load cell display box as an external trigger. The changes in loads from the load cell were interpreted as changes in voltages observed from the GOM software. The load cell was calibrated using three 10 kg masses, placed one at a time on top of the load cell, as well as a certified calibrated load cell of the same capacity for verification. From the voltage reading in table 4 a calibration graph to convert from voltage to force for each mass was plotted.

Table 4: 200 Kg load cell calibration voltage readings

Mass (kg)	Force (N)	Voltage (V)
0	0	0
10	98.1	0.225
20	196.2	0.426
30	294.3	0.627

Using the calibration graph in Figure 64 a trigger list of loads in terms of voltages was created in the GOM software settings. With a trigger list an image would be taken automatically when the specified voltage is reached as the actuator applies the loads via the piston and 30 mm spherical steel ball.

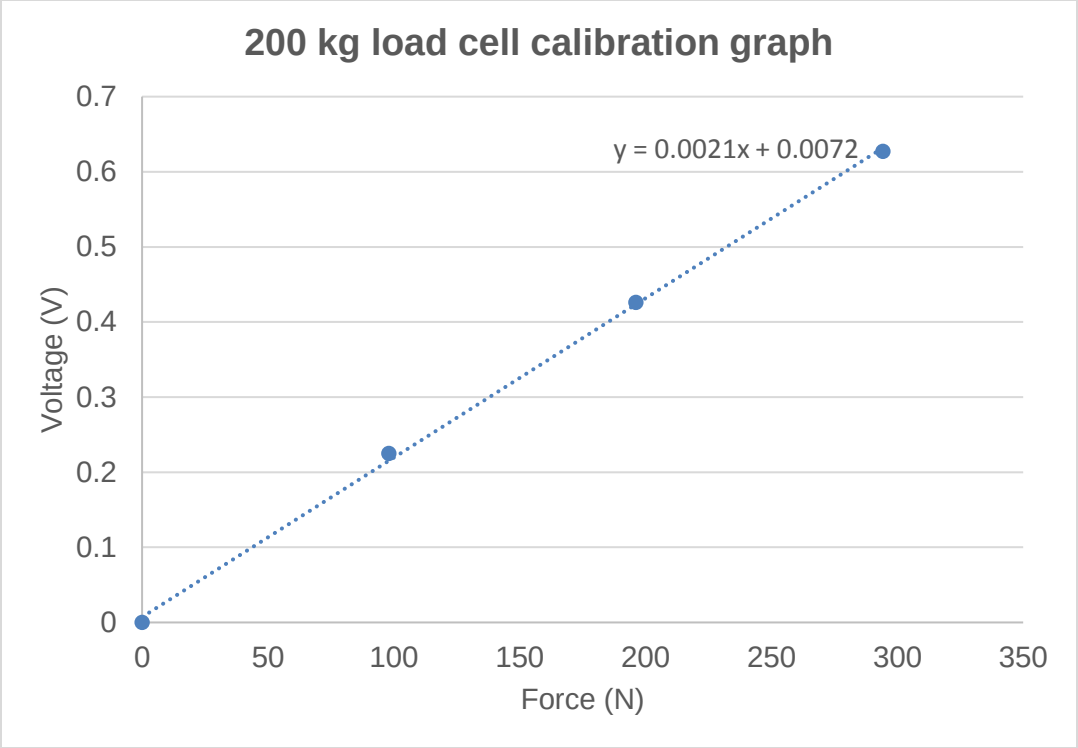

Figure 64: 200 kg load cell calibration graph to convert from voltage to Newton

4.3 Results of full field DIC damage detection in laminated composites under static loading

The experiments were conducted in two ways. In the first the force was applied to the specimen via a steel piston and a spherical steel ball located inside the holding plate. Both the ball and the piston had a diameter of 30 mm. In the second experiment the spherical ball was removed and the force was applied by a 24 mm diameter steel piston with a rounded end. From the two experiments it is expected that the specimen deformed using the 30 mm ball to show larger deformation than when the specimen is deformed using the 24 mm piston.

Figure 65 shows the force vs displacement curves for an undamaged and damaged laminated composite. The load history was determined through trial and error during the infliction of audible damage on the one specimen. The trial was started at low loads with increments of 10 N for a choice of 20 loads, the final choice in increments was 50 N which resulted in cracking of the matrix within 20 loads. Cracking sounds started to occur over the load of 900. From this the last six loads were removed from the trigger list so as not to cause any damage on the undamaged specimen during testing.

Each experiment was repeated four times to check repeatability, a variation in the range of 0 mm to 0.02 mm exists between the repeated experiments for both damaged and undamaged composite. The results show that under static loading conditions full field DIC can identify an undamaged composite from its counterpart by the reduction in stiffness.

4.3.1 Results of damage detection for loads applied via 30mm spherical ball

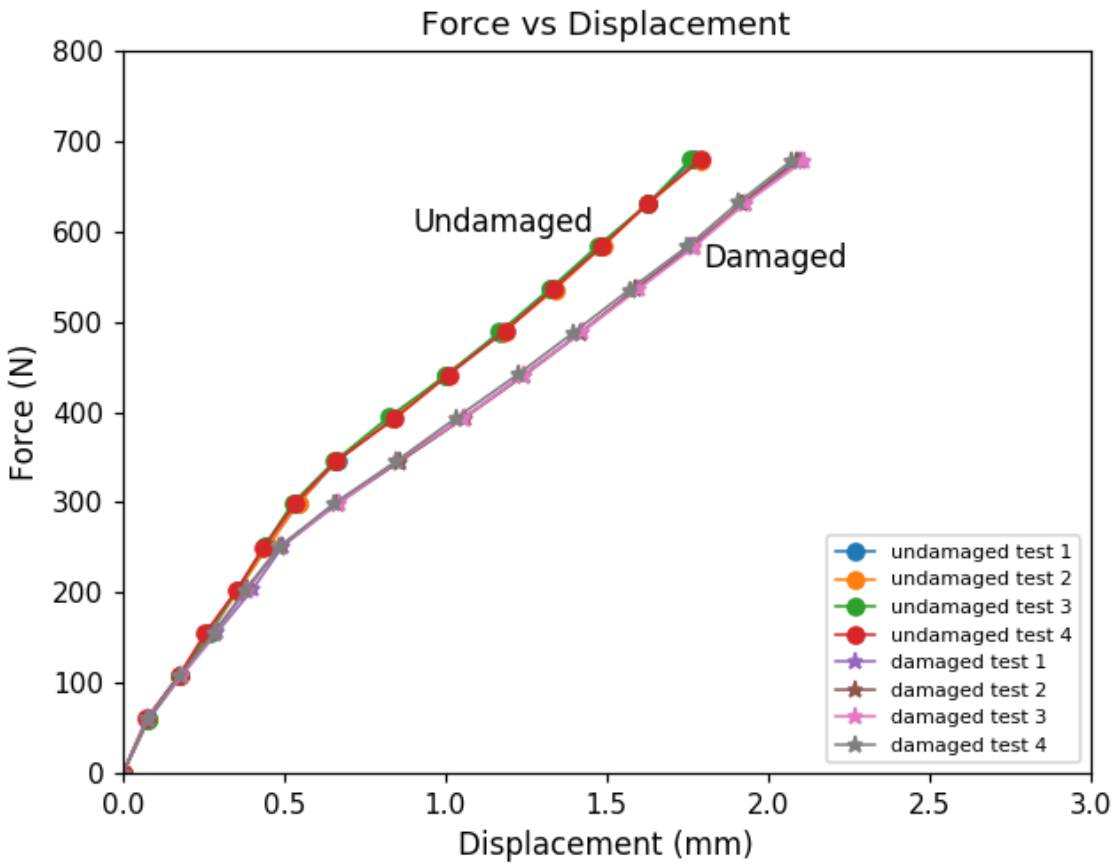

Figure 65: Force vs displacement curves for damage and undamaged composite, force applied by 30 mm spherical steel ball

From the results it can be observed that at small loads below 150 N the damaged and undamaged specimens behave in very similar ways. The increase in load is proportional to the difference in stiffness between an undamaged and damaged composite. The greater the load the more compliant the damaged composite becomes to deformation. The force vs displacements curves show a non-linear behaviour of both composites. Similar results have been attained in the work of Foulk et al. (2006).

Their work was centered on how woven fabrics of different materials, blends and moisture content affect the mechanical properties of the composite. They evaluated the mechanical performance of the woven fabric composites by using force vs displacement curves (Figure 66). Not much was mentioned in their paper regarding the experimental setup they made use of to obtain the force vs displacement curves, or whether the experiment was linear or conducted to failure for their test coupons. What their force displacement curves demonstrate is a similar non-linear behaviour to the results in Figure 65.

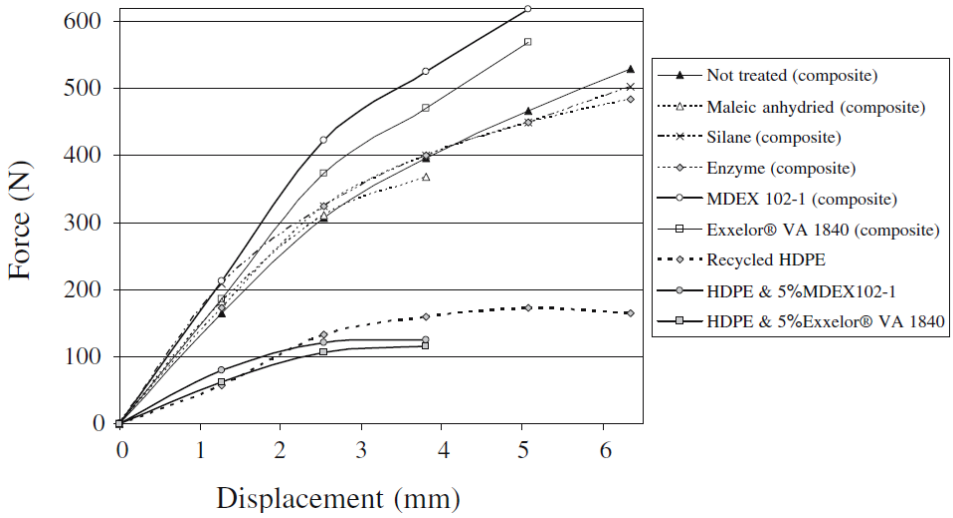

Figure 66: Force vs displacement curves for various woven fabric composites (Foulk et al., 2016)

Figure 67 shows the displacement fields for the damaged and undamaged composites subject to the final load of 679 N in the trigger list. Circular out-of-plane displacement fields are observed from the load which was applied by mean of a 30 mm steel spherical ball. The intensity of the displacement fields decreases moving away from the location where the load was applied demonstrating the law of deformation for point loading. The maximum displacement of 2.114 mm reported by the damaged composite was 0.324 mm more than the undamaged composite. The intensity of the displacement field for the damaged composite is more as seen from the colour bar which is in agreement with its loss in stiffness due to the damage.

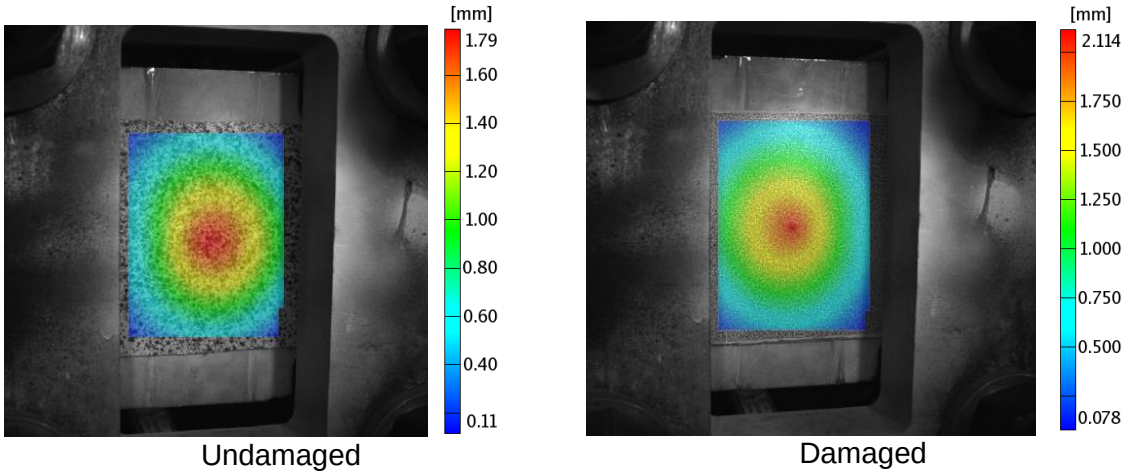

Figure 67: Undamaged and damaged laminated composites full field DIC +Z displacement field results at a static load of 679 N

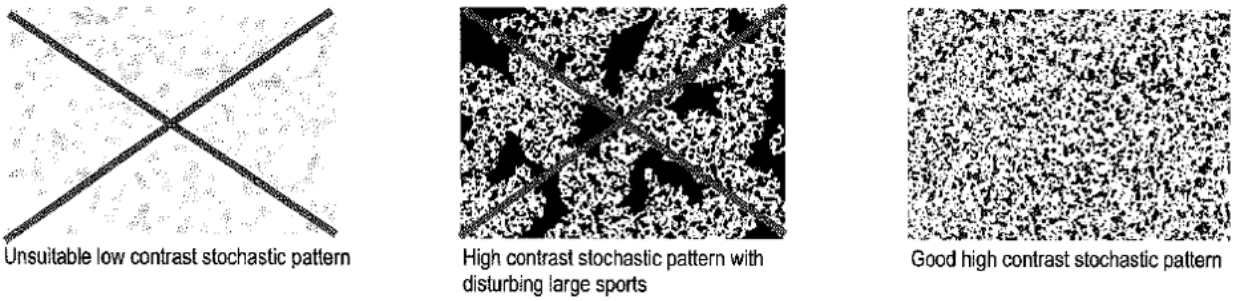

Figure 68: Good and bad contrast stochastic patterns (Aramis manual, 2009)

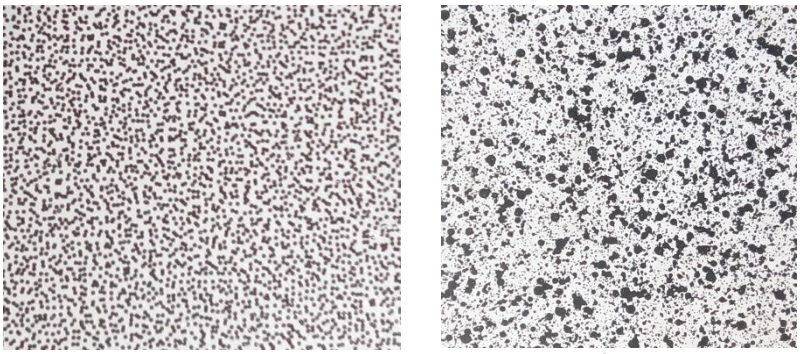

Figure 69: Comparison of scattered dot stencil and sprayed pattern with acceptable GOM stochastic pattern

The difference in resolution between the undamaged and damaged composite specimens (Figure 67) is due to the surface preparation of the specimens. A scattered dot stencil was used on the damaged composite and a scattered pattern was sprayed on the undamaged composite using matt black paint. The same DIC analysis settings were used in all the experiments for both undamaged and damaged composite. The best stochastic pattern is one that offers good high contrast without areas of large spots or constant brightness (Figure 67). A comparison of the GOM acceptable stochastic pattern and that of the undamaged and damaged composites shows that both methods of surface preparation are acceptable (Figure 69). Since the stencil provides smaller black spots per area than the sprayed on pattern it results in better resolution.

4.3.2 Results of damage detection for load applied via 24 mm rounded piston

Figure 70 shows the force vs displacement results for the second full field DIC experiment in which a 24 mm diameter steel piston with a rounded end was used to apply the load. The results are superimposed with those of the first experiment in which the force was applied to the composite via a 30 mm spherical steel ball. Once again in the second experiment the tests were repeated four times to confirm repeatability of the experiment. A different trigger list of loads was used for the second experiment (24 mm piston) with a higher starting load.

The results show that both the stiffness of both the damaged and undamaged composite increased as a result of a reduction in the contact area (i.e. from 30 mm spherical steel ball to 24 mm steel piston with a rounded end).

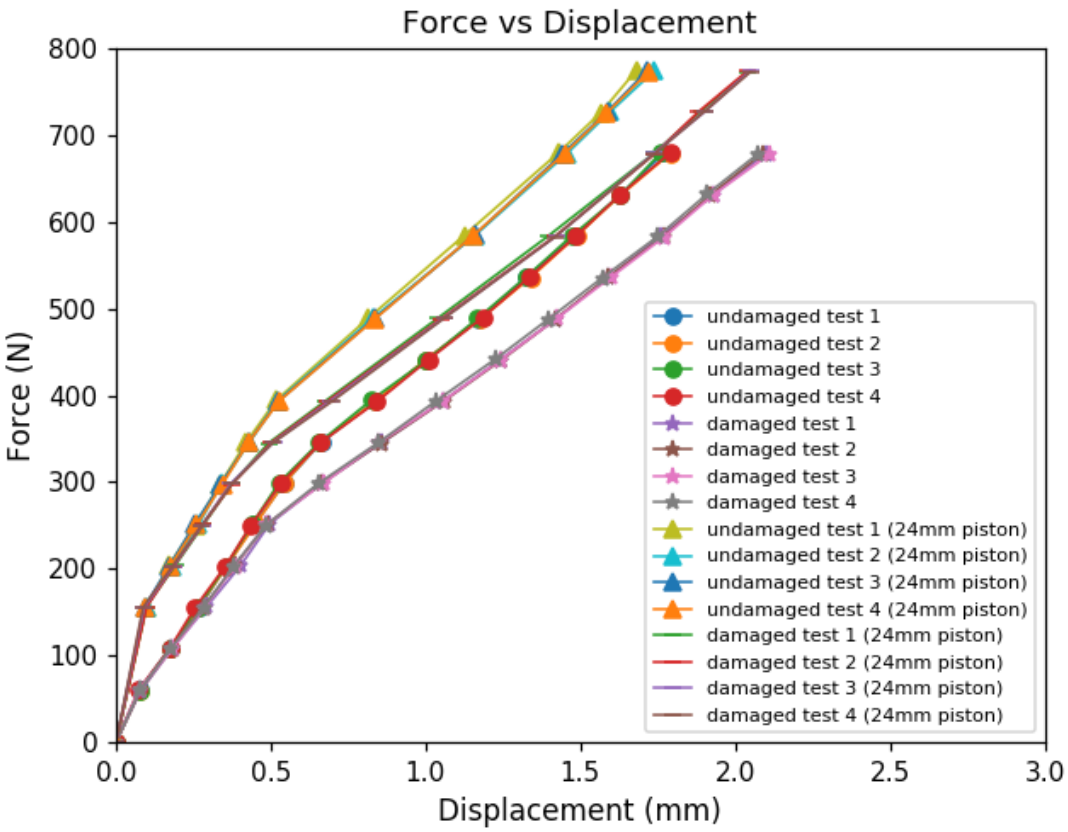

Figure 70: Force vs displacement curves for damaged and undamaged composite. Force applied by 30 mm spherical steel ball and 24mm steel piston superimposed

The results of the second experiment also show that the reduction in contact area increased the load at which a difference in stiffness between the damaged and undamaged composite starts to become evident (i.e. from below 150 N in the first experiment to below 200 N in second experiment).

The second experiment still shows that the damaged composite is more compliant than its counterpart. It can also be observed that the greater the load the more significant the difference in stiffness becomes with a similar non-linear behavior as in the first experiment.

Figure 71 shows the displacement fields of the damaged and undamaged composite subjected to the final load in the trigger list of 774 N applied via a 24 mm steel piston with a rounded end. The displacement fields of both specimens are still circular as expected since the piston had a rounded end. The final displacement at the center of the composites show that the damaged composite deformed 0.33 mm more than the undamaged composite. The damaged composite displacement field intensity in the second experiment is still higher than the undamaged composite.

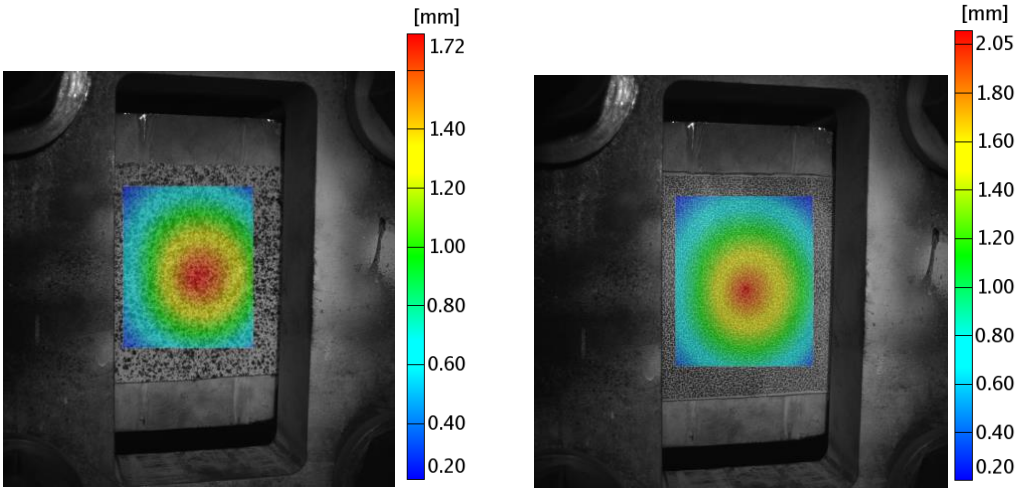

Undamaged Damaged

Figure 71: Undamaged and damaged laminated composites full field DIC +Z displacement field results at a static load of 774 N

4.4 Full field DIC experimental setup and camera calibration for damage detection in laminated composites under dynamic loading

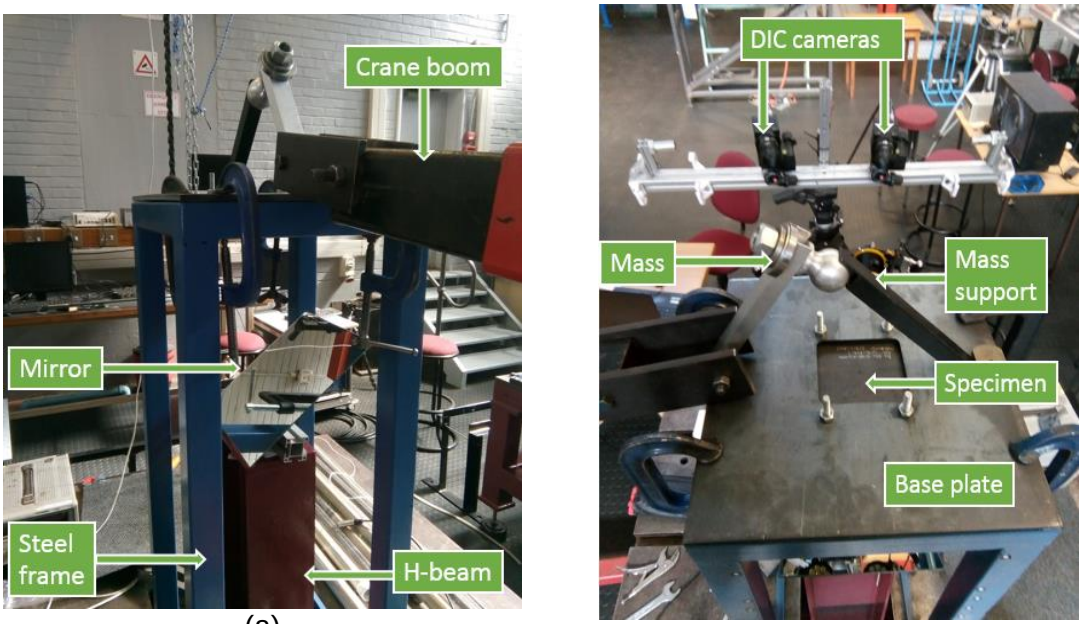

(a) (b)

Figure 72: Impact test setup: (a) shows the side view of the setup, (b) shows the top view of the setup

Figure 72 shows the experimental setup that was used for damage detection in laminated composites under dynamic loading. The experimental setup consisted of a steel frame whose base was fixed to a heavy duty work table via clamps to ensure full stability. An H-beam was placed in the open portion of the work table located at its center. The H-beam was used to support the mirror through which the deformation of the specimens was captured by the cameras. A 400 mm x 400 mm x 15 mm steel base plate was used to support the specimens using M10 bolts and was clamped to the steel frame.

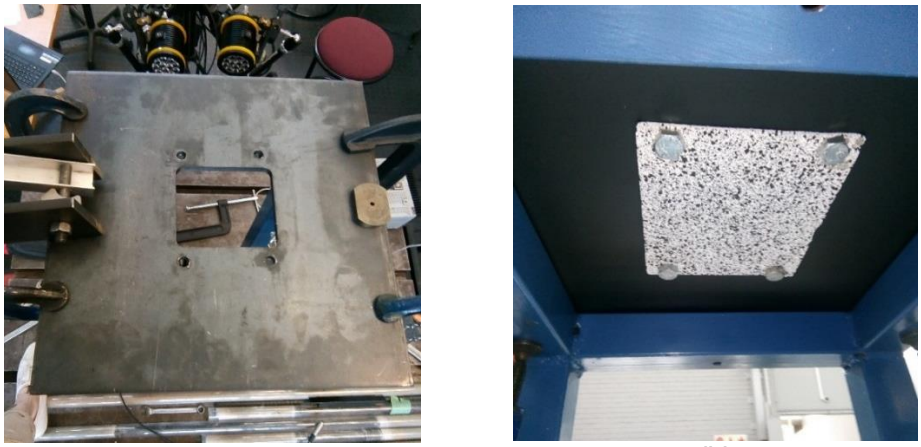

(a) (b)

Figure 73: 15 mm base plate: (a) shows the top of the base plate without the specimen attached, (b) shows the bottom of the base plate with the specimen attached

Figure 73 shows the top and bottom of the steel base plate, it has 100 mm x 110 mm opening to allow impact. The specimens were bolted to the bottom side of the base plate in order to expose the entire specimen to the mirror and to have the base plate window edges play no part in affecting the deformation. A swinging mass of 0.6 kg with a spherical end was used as the impactor. It was held in position by the boom a mobile crane. The mass was held in position by steel bar at height of 155 mm above the specimen imparting an energy of 0.9 J which was low enough so as not to induce any additional damage. To establish this a trial an error method was also adopted starting at a small energy of 0.2 J, and incrementing as necessary till the obtained peak displacement results were similar to the final peak displacements obtained under static loading conditions.

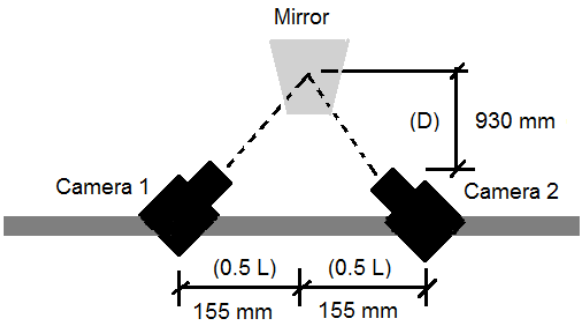

Figure 74: NX8 high speed camera setup for impact tests

Figure 74 shows the IDT NX8 high speed camera setup that was used to capture the dynamic response of the specimens subjected to impact loading. In order to ensure accurate out-of-plane measurements a rule of thumb in the Image system motion analysis. (2016) was followed which states that:

$$L \approx \frac{1}{3} D$$

Where: L is the distance between the cameras and D is the measuring distance.

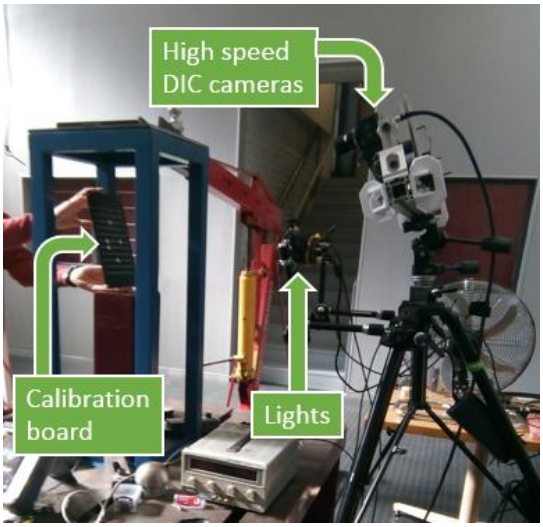

(a)

(b)

Figure 75: Setup for high speed camera calibration for full field DIC under dynamic loading: (a) shows the calibration board held 930 mm away from the cameras, (b) shows and acceptable GOM analyzed image of the right camera for correct calibration

Figure 75(a) depicts how the high speed cameras were calibrated. An A4 size calibration board with white dots on its surface was used to calibrate the cameras. The mirror was removed and the board was held by hand at the same measuring distance of 930 mm. 500 images per camera of the board were taken at different angles, which include the board rotated up to 90° in-plane and tilted up to 40° out-of-plane. The images were captured using Motion Studio and imported into the ARAMIS GOM software for analysis and generation of a calibration file within GOM specification. Enough of the dots including the larger main dots on the calibration board must be recognized in all the images captured by both the left and right camera (i.e. marked green, Figure 75(b)) in order to obtain a calibration deviation between 0.01 and 0.07 pixels (Aramis, 2009). Once an acceptable calibration file was obtained the mirror was placed back for the experiments.

4.5 Results of full field DIC damage detection in laminated composites under dynamic loading

Figure 76 shows the dynamic responses of the undamaged composite during the first and second impact as well as the displacement fields of the initial impact energy of 0.9 J. Experiments conducted using the available NX8 cameras at their maximum 4000 fps at full resolution resulted in errors during image processing using the GOM, therefore the optimal camera settings for the experiment had to be found through trial and error. The cameras were set to capture 2000 images at a rate of 1500 fps resulting into a duration of 3 seconds. The duration was enough to capture the initial impact and the rebound. Each experiment was repeated three times using the high speed cameras. All the captured images were imported and analyzed using the Aramis GOM software.

The results of the dynamic tests are presented as an Aramis GOM report, the report shows two figures for all three tests: the first figure on the top shows the +z displacement vs image graph and the second figure on the bottom shows the out-of-plane displacement field of the initial impact superimposed on the laminated composite.

The repetition of the experiment done on the undamaged specimen reveals a variation in the displacement fields in the range of 0 mm to 0.018 mm between experiments. The range is similar to the repeated tests in the static analysis for the undamaged composite. From the +z displacement vs image plots it is observed that the response of the initial impact is larger in value than the rebound impact. This is expected since the energy of rebound impact is reduced due to the deceleration of the impactor as the specimen resists penetration from the first impact, this resultes into a smaller rebound height (i.e. lower potential energy than before). In all experiments the displacement fields are circular and reduce in intensity moving away from the impact location, i.e. the center of the specimens.

A comparison in dynamic response between the damaged and undamaged displacement results reveals a difference in peak displacement ≤ 0.03 mm, which is insufficient to distinguish the damaged composite from its counterpart (Figure 76). This suggests that the size of the damaged area induced in the composite via point loading is not sufficient to enable detection from a dynamic response measured using full field DIC. This can be explained by the possibility that the depth of the damage in the thickness direction from the one side is not enough to be noticed by measuring the dynamic response of the other side.

To prove this hypothesis the damage size and depth was increased using a hammer resulting in visible indentations on the composite. Figure 77 shows the dynamic results between the severely damaged and undamaged specimen. A difference in maximum displacement in the range > 0.03 mm was observed between the severely damaged and undamaged composite, a range similar to the results obtained under static loading.

A difference in maximum displacement of 0.119 mm, 0.096 mm and 0.078 mm is observed from Figure 77 between the undamaged and severely damaged composite for the first, second and third tests respectively.

The results suggest that in order to detect damage in laminated composites under dynamic excitation, the depth and size of the damage needs to be significant i.e. completely visible damage on both sides of the specimen over a large area. Comparing the full field DIC measurements under static loading and dynamic loading, shows that under static loading condition one can detect small sized damage more successfully than subjecting the specimens to impact loading.

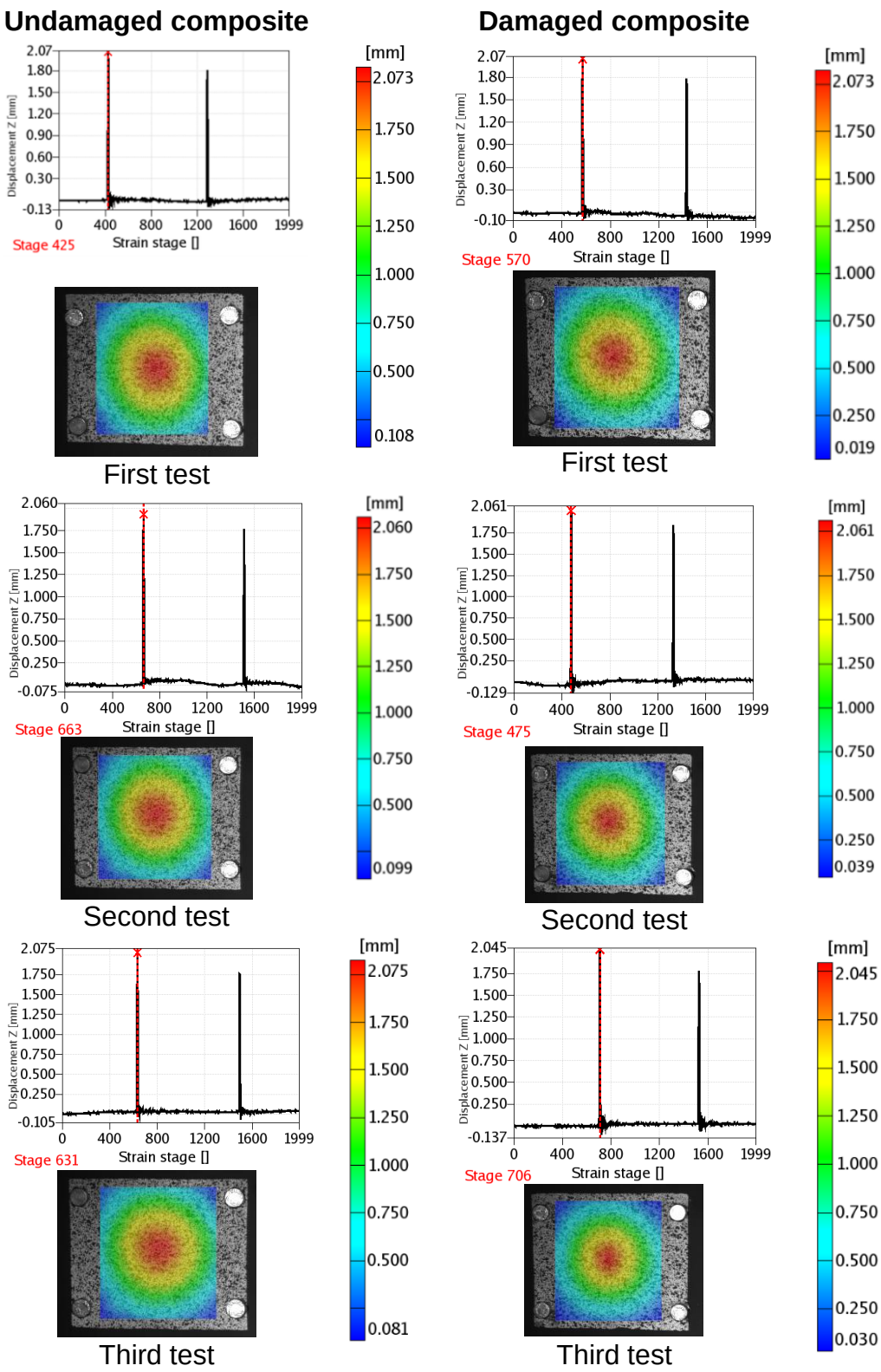

Figure 76: Dynamic results of a damaged and undamaged carbon/epoxy woven laminated composite plates showing +z-displacement vs image plots and +z-displacement fields in response to an initial impact of 0.9 J

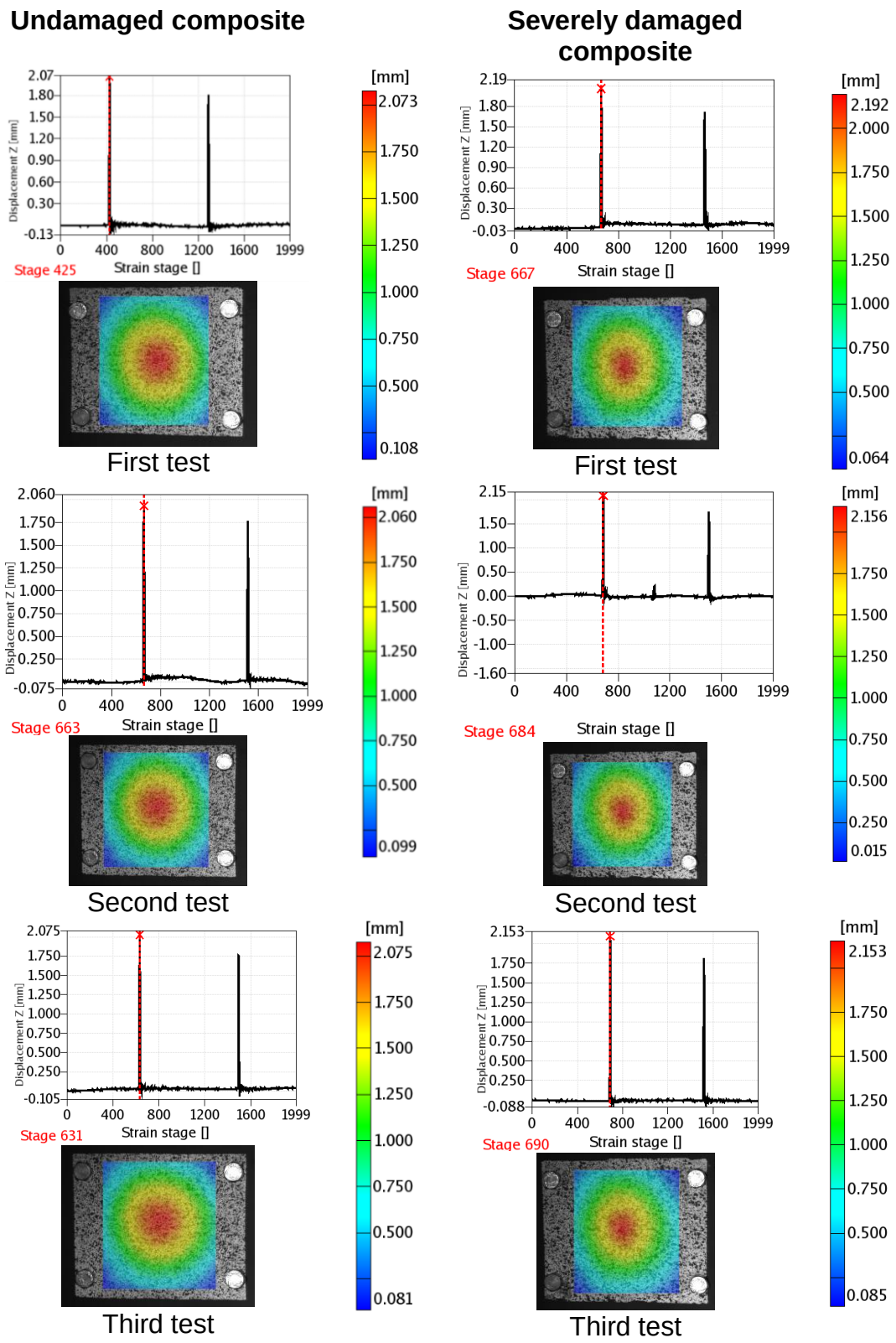

Figure 77: Dynamic results of a severely damaged and undamaged carbon/epoxy woven laminated composite plates showing +z-displacement vs image plots and +z-displacement fields in response to an initial impact of 0.9 J

4.6 Discussion of Preliminary investigations of damage detection in laminated composites using experimental modal analysis and full field DIC

Phase one of the research revealed interesting results with regards to using different techniques to detect damage in laminated composites. The use of modal analysis both the contact and non-contact approach show no significant change in the value of the natural frequencies between the undamaged and damaged composite. The type of damage which is of interest in this research (i.e. barely visible damage) causes no significant change in the modal properties of the composite. Modal properties are often affected by changes in mass of the component, the damage induced in this research is not expected to change the mass of the composites. The matrix and possibly fiber damaged induced in the composite caused a reduction in stiffness of the composite but not significant enough to cause shifts in the value of the natural frequencies which would be indicative of the damage.

Full field digital image correlation showed good results in measuring rigid body motion and out-of-plane displacements. The results assured the ability of full field digital image correlation in capturing deformation data accurately. With full field DIC the barely visible damage could be detected by measuring the out-of-plane deformation of the composites subjected to a static point load. The force vs displacement curves revealed a reduction in stiffness of the damaged composite.

Full field DIC experiments under dynamic loading condition showed no significant change in out-of-plane deformation data of the undamaged and damaged composite after being subjected to an impact energy of 0.9J. Under dynamic loading conditions the initial induced barely visible damage could not be detected using full field DIC. Only when damage was significantly severe and clearly visible on the composite could full field DIC detect changes in out-of-plane deformation between the undamaged and damaged composite. The severely damaged composite showed greater out-of-plane deformation than the undamaged composite due to loss of stiffness.

From the full field DIC experiments it can be concluded that barely visible damage in laminated composites can be detected under static loading condition. The final stage of the research explores variations in the extent of the damage caused by varying impact energies. From the full field DIC results under static loading conditions, the use of a scattered dot stencil for surface preparation showed better resolution in out-of-plane deformation fields than the composite that had the pattern prayed on with matt black spray paint.

Chapter 5: Barely visible impact damage detection in laminated composites using full field DIC under static loading conditions

This section of the research was informed by the results of the experimental work conducted in first stage. Barely visible impact damage (BVID) in laminated composites was induced by varying energies. The carbon/epoxy woven laminated composites were subjected to static loading. The deformation data (i.e. out-of-plane displacement and von Mises strain fields) was captured using full field DIC prior and post the impact in order to compare changes in deformation data as a result of the induced damage.

5.1 Overview

The preliminary investigations of this research explored various method for damage detection in laminated composite (Barely visible damage). Informed by the literature review modal analysis was the first method to be explored. However, the modal results showed no significant shifts in natural frequency values between undamaged and damaged laminated composite. Between full field DIC under static and dynamic loading, the performance of full field DIC under static loading showed potential in detecting barely visible damage, and thus the preferred method for the final investigation of the research.

- A 24 mm diameter piston was used to apply the load to the laminated composites for simplification.
- Scattered dot stencils were used for the speckles with a diameter of 0.05 inches and a density of 75% as part of surface preparation of the specimens due to the resulting better resolution in the deformation data (i.e. out-of-plane displacements).
- A drop impact apparatus was designed for causing the barely visible impact damage at different energies.
- The results of each specimen were captured before and after the impact damage.

Carbon/epoxy woven laminated composites used in the experiments were purchased fully fabricated without details of the fabrication process. The composites were divided into two groups i.e. the first group was for centered impact at various energies and the second group was for off-center impact. Off-center impact damage was done to study if full field DIC under static loading could still detect the damage even when the loading is not applied around the damaged area.

The laminated composites were subjected to varying impact energies of 3 J, 6 J, 9 J, and 12 J in order to study at what energy level the damage becomes detectable using full field DIC. Based on literature looking into load vs displacement behaviour for different laminates of different thickness (Tiziana et al., 2019), it not expected that 3 J of impact energy to result in detectable damage.

5.2 Description of laminated composites

Two 300 mm x 300 mm x 1mm fully fabricated carbon/epoxy woven laminated plates were purchased. The plates were labeled plate A and plate B. Four pieces of the required dimensions (i.e. 156 mm x 133 mm x 1 mm) were cut from plate A and B using an electric band saw. Plate A1′ and B3′ in Figure 78 were cut from a separate plate. Four 10.3 mm holes were drilled on each specimen as fixture locations using M10 bots for the experimental setup for impact tests and full field DIC under static loading.

The specimens were given 3 coats of matt white spray paint. When dry the scattered dot stencils were applied on the white surfaces as the final step of surface preparation for full field DIC. The back face of each laminate was labelled according to the plates they were cut from, and the locations for centered and off-centered impact were marked with a cross using a permanent white marker as shown in Figure 78.

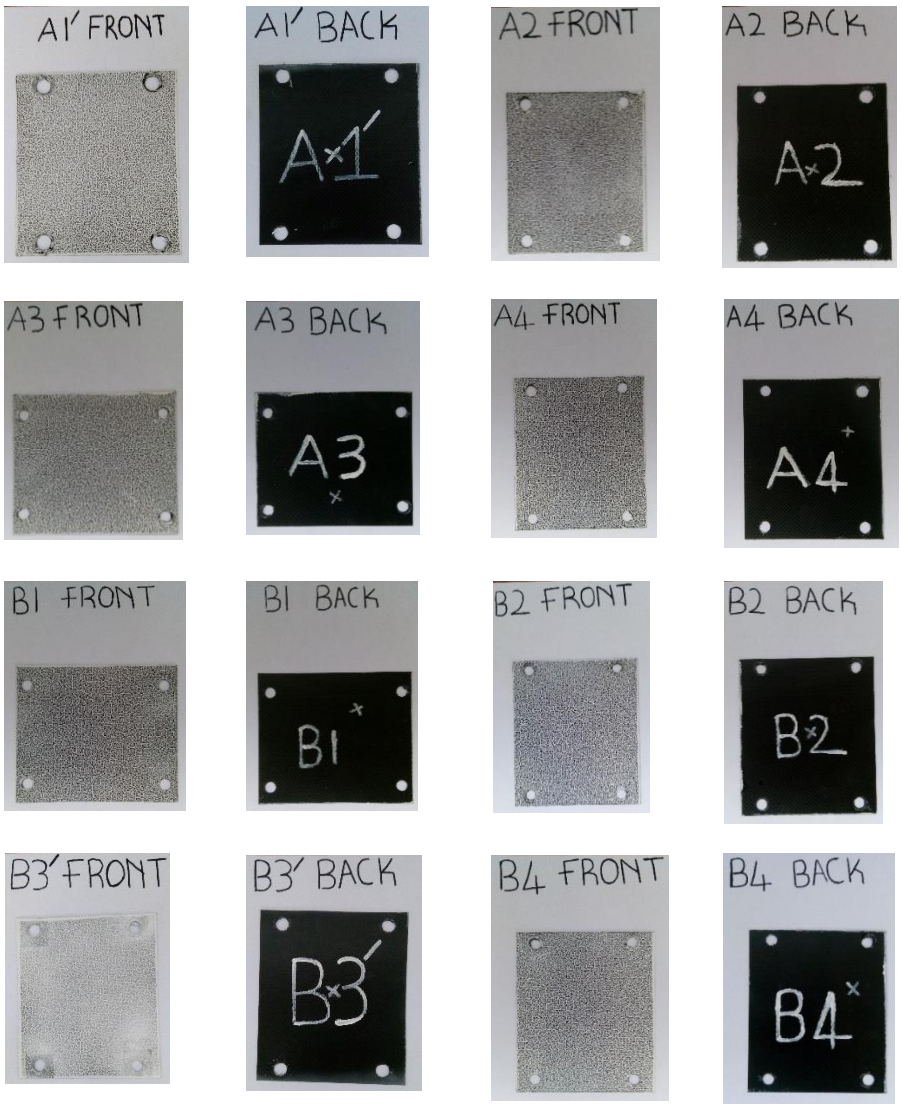

Figure 78: Carbon/epoxy woven laminated specimens showing the front and back face of each specimen

5.3 Plan for the experiments

The final stage of this research is structured to evaluate at what impact energies the induced barely visible impact damage becomes detectable using full field DIC under static loading. To eliminate any bias in the experimentation the specimens cut from the original plate A and B were mixed for the centered and off-center impact as shown in table 5

Table 5: Assignment of specimens for the centered and off-centered impact energies

Impact energy	Centered impact	Off- centered impact
3 J	Specimen A1′	Specimen B1
6 J	Specimen B3′	Specimen A4
9 J	Specimen A2	Specimen B4
12 J	Specimen B2	Specimen A3

To account for the variety introduced in the measurements by full field DIC under static loading conditions and the experimental setup, repeated experiments on one of the specimens (i.e. Specimen B2) were conducted. The repeat experiments included recalibration of the cameras and dismantling of the specimen prior and post the impact.

5.4 Experimental setup for drop impact tests and full field DIC

In this section the test apparatus that was designed for the causing the impact damage is discussed along with the experimental setup for the full field DIC under static loading conditions.

5.4.1 Drop impact test apparatus

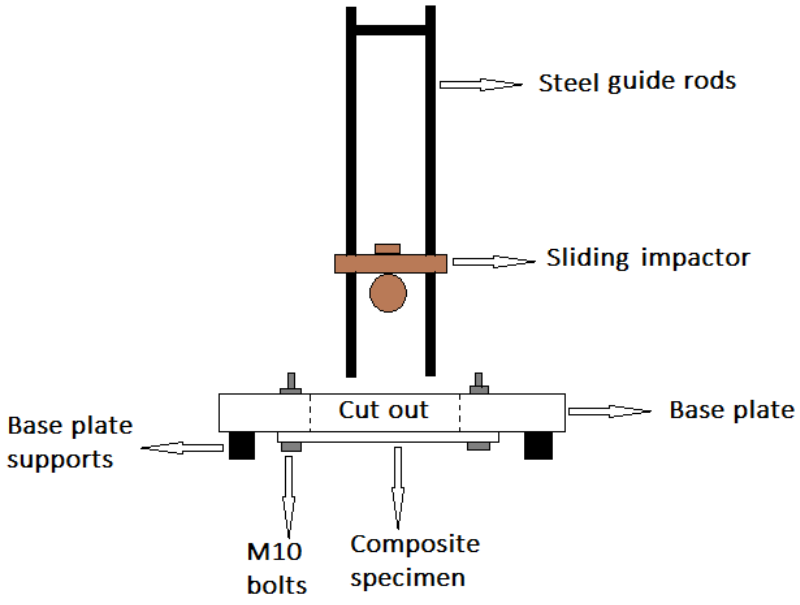

Figure 79: Simplified schematic representation of the drop impact apparatus

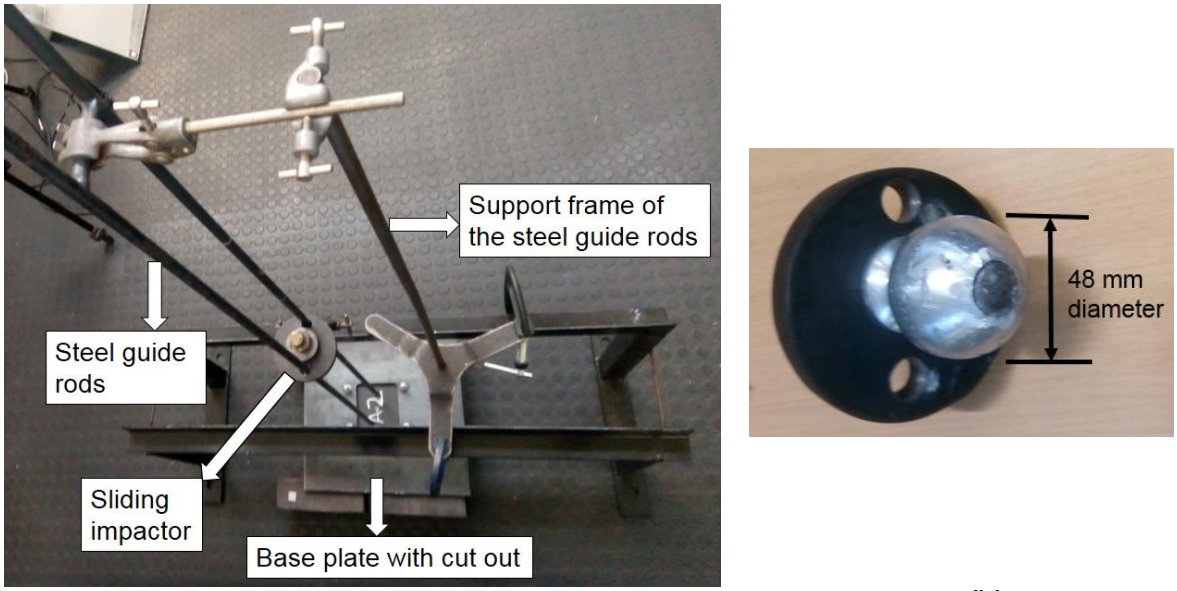

Figure 80: Actual drop test apparatus: (a) shows the setup, (b) shows the 1.4 kg impactor

Figure 79 shows the schematic representation of the constructed drop impact apparatus that was used to induce barely visible impact damage in the laminated composite specimens. Figure 80 shows the actual apparatus for the drop tests. Two 12 mm steel rods were used to construct a guide frame for the sliding impactor. A 1.4 kg mass with a rounded end was used as the impactor. Two 18 mm holes were drilled on the weight attached to the impactor to enable smooth sliding from the required height Figure 80(b). A 400 mm x 400 mm x 15 mm steel base plate with a 100 mm x 110 mm cut-out was used to support the specimens using M10 bolts from the bottom face of the plate. The cut-out exposed the back face of the laminated composite specimens to the centered and off-centered impacts. The steel base plate could be moved so as to align the marked location on the specimen with the tip of the impactor. The heights for the required impact energies were marked on the guide rods. For each test the impactor was simply raised to the required height and allowed to drop down to the specimen.

5.4.2 Experimental setup for full field DIC

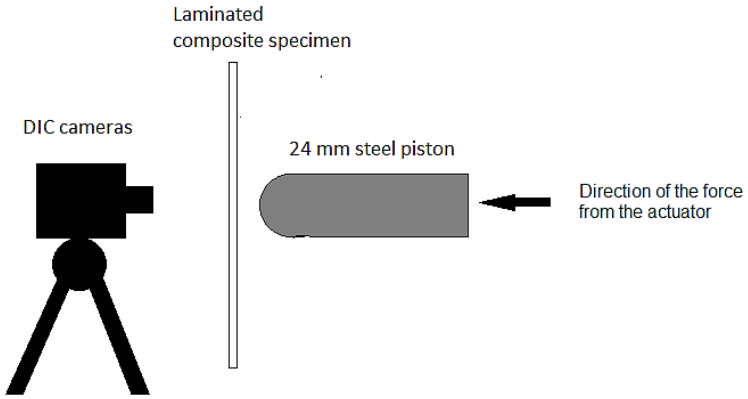

Figure 81: Simplified schematic representation of full field DIC setup for damage detection under static loading

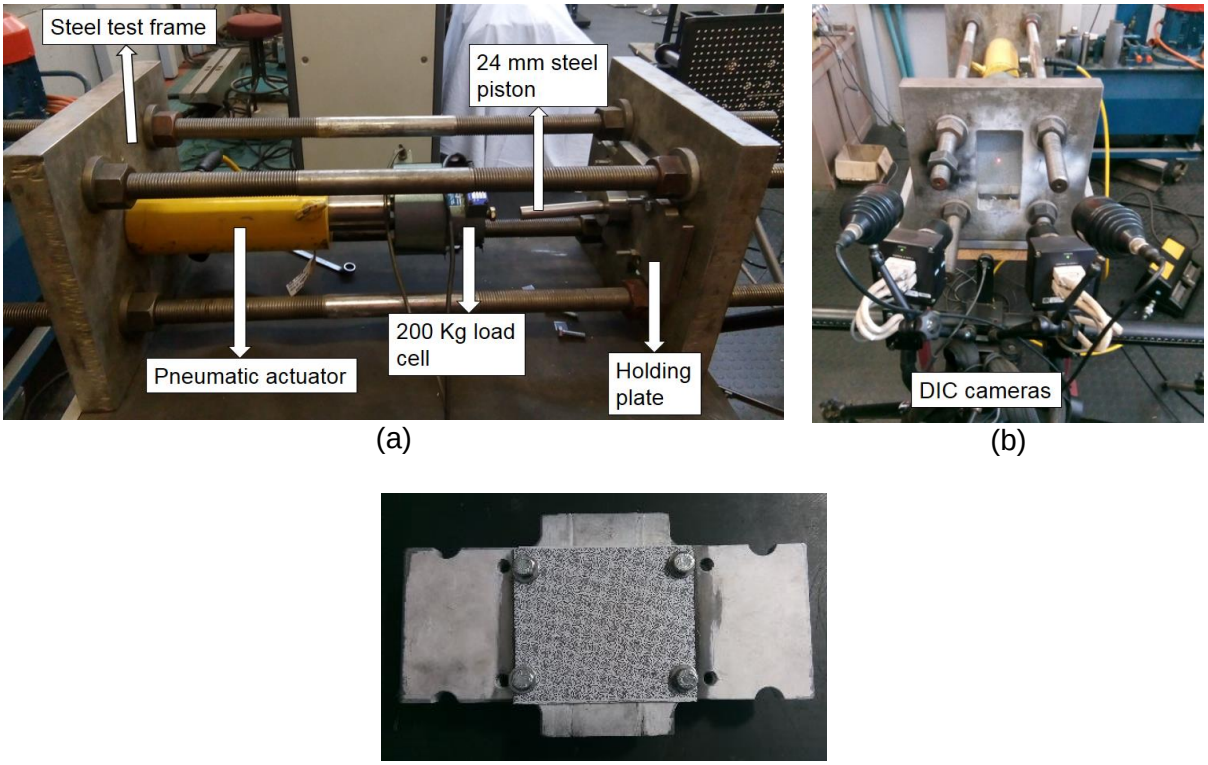

(a) (b)

(c)

Figure 82: Experimental setup for the full field DIC: (a) shows the side view of the setup, (b) shows the front view with the DIC cameras, (c) shows the holding plate with specimen attached to it using M10 bolts

Figure 81 shows a simplified schematic representation of the actual full field DIC experimental setup (Figure 82) that was used for damage detection in laminated composites. A holding plate was used to secure the specimens using M10 bolts (Figure 82(c)), the holding plate itself was attached to the test frame of the setup using M10 bolts. The front of the test frame has a cut out which exposes an area (220 mm x 110 mm) of the laminated composites to the DIC cameras as shown in Figure 82(b). A pneumatic actuator was used to exert forces to the back face of the laminated composites via a 24 mm steel rod with a rounded tip which slid through the hole on the holding plate. A calibrated 200 kg load cell was used to measure the forces applied to the specimens. The load cell was connected to the DIC data acquisition system as an external trigger, the Images during deformation were captured according to the set trigger list of loads (calibration of the load cell is documented in section 4.2).

5.5 Experimental results of damage detection in laminated composites using full field DIC under static loading

In this section full field DIC results of the laminated composite specimens which were subjected to center and off-center impact are discussed. The results included force vs displacement curves, force vs von Mises strain curves, out-of-plane displacement fields and von Mises strain fields. The von Mises strain became additional data to examine in this investigation when the out-of-plane data obtained showed no noticeable change in stiffness due to the damage as it did in the preliminary investigations (section 4.3).

The loads used in the trigger list were obtained through trial and error as described in section 4.3 but lower in magnitude due to the smaller thickness.

5.5.1 Variations in full field DIC measurements between repeated test, recalibrating of the cameras and dismantling of the specimens.

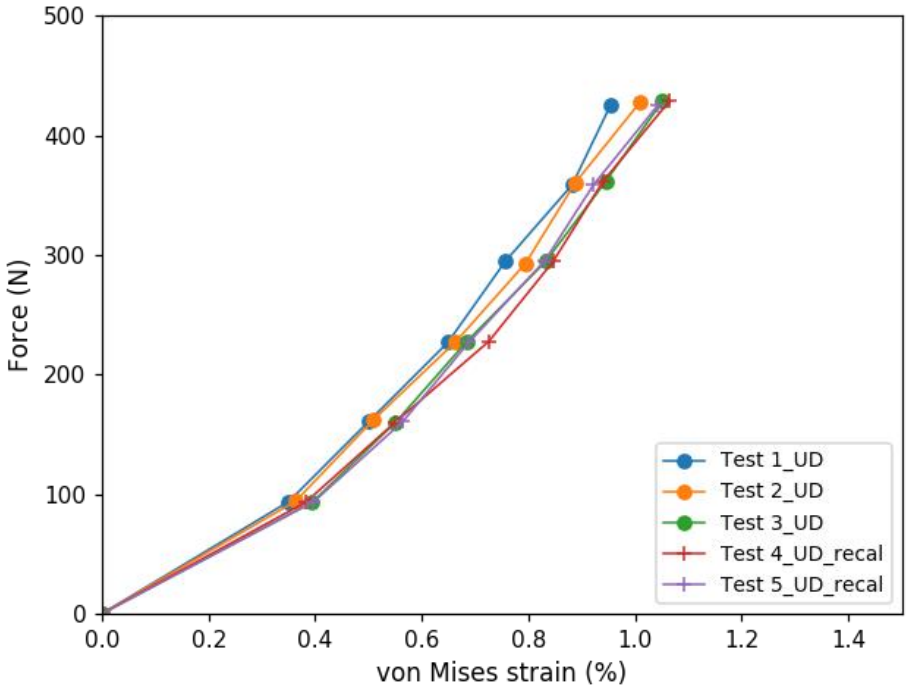

Figure 83: Variation in full field DIC von Mises strain measurements of specimen B2 repeated test and camera recalibration before impact of 12 J, where "UD" stands for undamaged, "D" stands for damaged and "recal" stands for recalibration of the cameras

Figure 83 shows the force vs von Mises strain curves of specimen B2 before the centered impact of 12 J. On the legend of the plot "UD" stands for undamaged and "D" stands for damaged and "recal" stands for recalibration of the cameras. The specimen was subjected to six loads as defined in the trigger list. The curves of the undamaged B2 specimen show that a variation exists between repeated test without dismantling and recalibrating the cameras between tests (test 1-3). Test 4 and 5 include dismantling of the specimens and recalibration of the cameras between the tests. No significant variation is noticeable between the tests as the curves of some of the tests that were performed with and without recalibration of the cameras sometimes coincide. The small variation between the tests may be a result of slight voltage fluctuations from the load cell resulting in exact, slightly higher or lower loads than stated in the trigger list.

Figure 84 shows the von Mises curves of the undamaged and damaged B2 specimen after 12 J of centered impact energy. The manner in which the tests were conducted was the same as before the impact; with test 1-3 done without dismantling and recalibration and test 4 and 5 with dismantling and camera recalibration. An immediate noticeable difference lies in the increase in strain values after impact. The barely visible damage caused by an impact of 12 J resulted in a

more compliant specimen (reduced stiffness). The deference in strain values between the undamaged and damage B2 specimen increased with increasing load.

Regardless of the variation in measurements a clear distinction in stiffness due to the impact is evident from the curves.

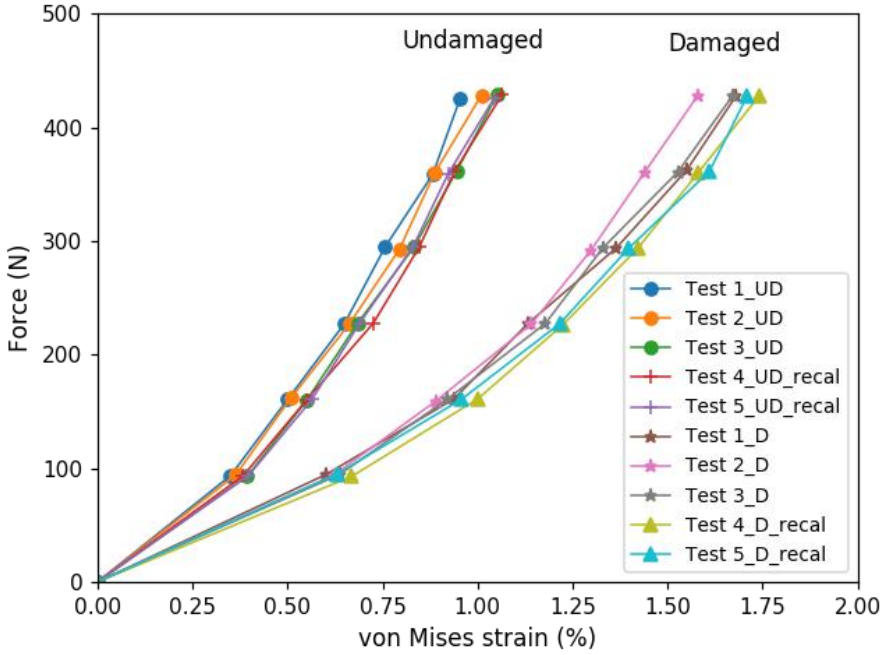

Figure 84: Full field DIC von Mises strain measurements of specimen B2 repeated test and camera recalibration before and after the impact of 12 J, where "UD" stands for undamaged, "D" stands for damaged and "recal" stands for recalibration of the cameras

Table 6 summarizes the range in variation possible from von Mises strains measurements obtained between the tests for specimen B2. From table 6 it can concluded that a maximum variation in von Mises strain of about 0.2% is possible between repeated tests.

Table 6: variation range in % Von Mises strains between repeated tests including dismantling and camera recalibration

	Undamaged B2 specimen	Damaged B2 specimen
Variation range	0 - 0.1 %	0 - 0.16 %

Figure 85 shows the out-of-plane displacement fields of specimen B2 prior to impact for three test in which the specimen was removed and installed again between tests. The out-of-plane displacement fields show that slip of the specimen at the bolts due to uneven torque can change the shape of the displacement field close to the edges of the specimen.

An error percentage in peak displacement of 12.2%, 11.1% and 0.93% was obtained between test 1 and 2, test 1 and 3 and test 2 and 3 respectively. This suggest that it is better to be consistent when tightening the bolts.

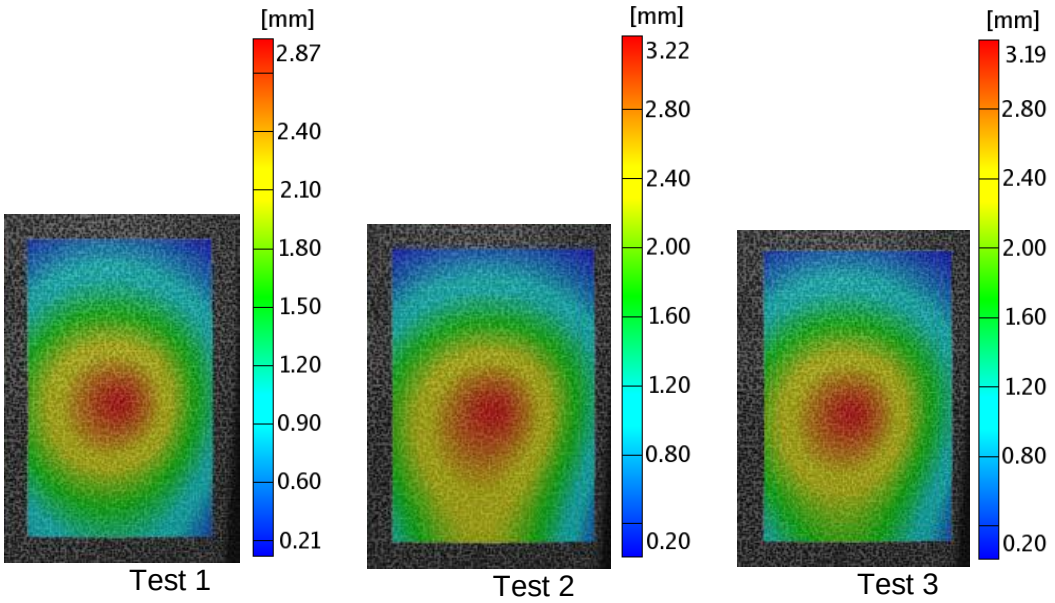

Figure 85: Out-of-plane displacement fields at a load of 161 N showing the effects of slip of the specimen B2 (prior to impact) at the bolts due to uneven torque when mounting and unmounting the specimen between repeated tests

5.5.2 Full field DIC results of laminated composites subjected to centered impact

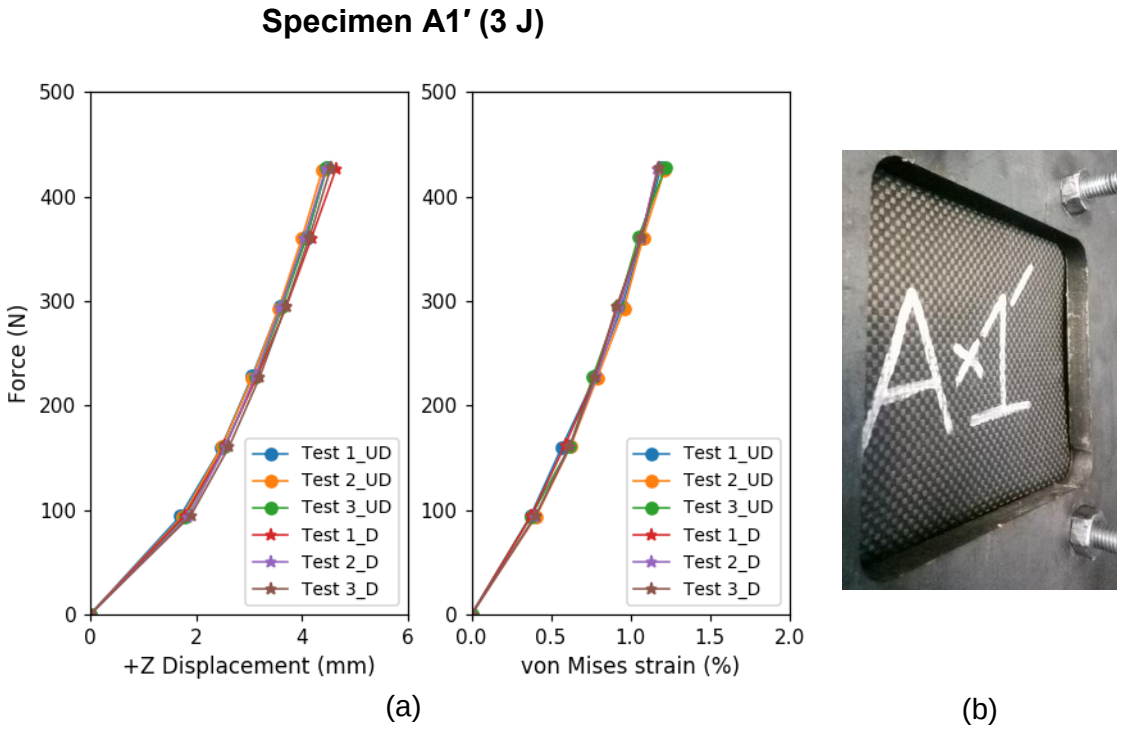

Figure 86: Full field DIC results of specimen A1′ which was subjected to 3 J of impact energy: shows the force vs out-of-plane displacement curves and force vs von Mises strain curves, where "UD" stands for undamaged and "D" stands for damaged, (b) shows the specimen after the impact

Figure 86(a) shows the full field DIC results for first specimen (A1′) which was subjected to a centered impact energy of 3 J. Figure 86(a) shows the force vs out-of-plane displacement curves and the force vs von Mises strain curves before and after the impact. Three tests were conducted for repeatability in each case. Both the out-of-plane displacements and von Mises curves show no change in stiffness due to the impact of 3 J. On all curves the values of the out-of-plane displacements and von Mises strains coincide for every test conducted before and after the impact. The results suggest that the impact energy of 3 J did not cause any significant impact damage detectable by using full field DIC, or the impact energy was too low to cause any damage at all. The specimen showed very little deformation after the impact as shown in Figure 86(b). The deformation however was not permanent and the specimen reverted to its original form once it was unbolted from the base plate. The impact energy of 3 J resulted in no damage as demonstrated by the full field DIC results of specimen A1′, this suggests that the 1 mm thick laminates are resistant to that amount of energy as expected (Tiziana et al., 2019).

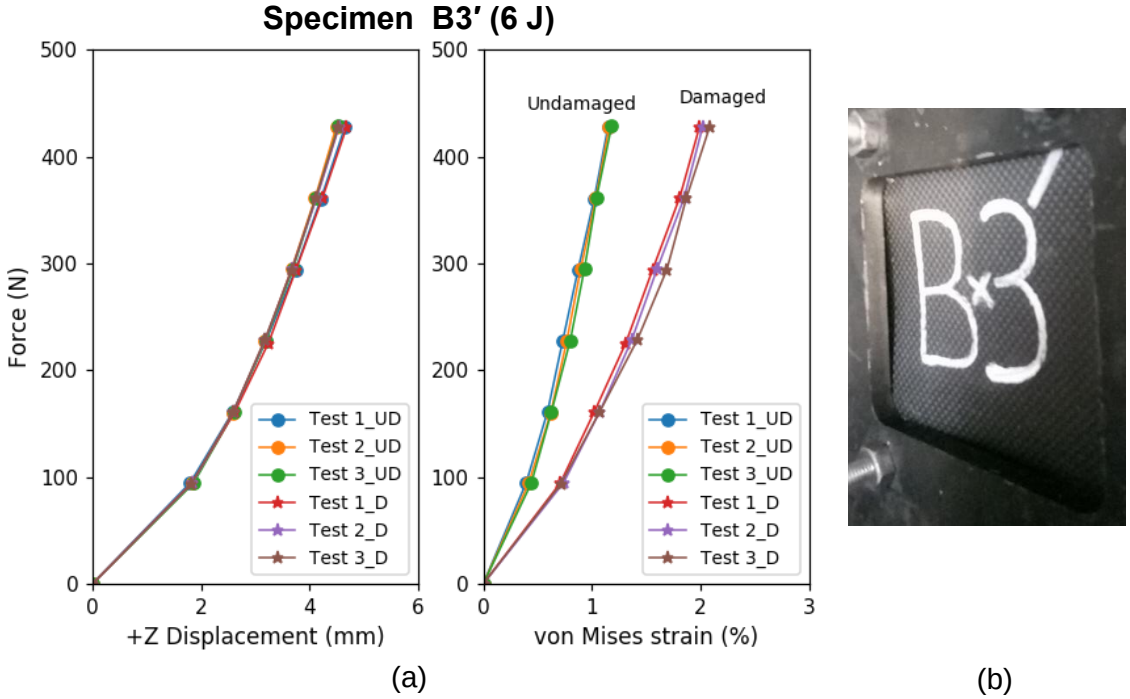

Figure 87: Full field DIC results of specimen B3′ which was subjected to 6 J of impact energy: (a) shows the force vs out-of-plane displacement curves and force vs von Mises strain curves, where "UD" stands for undamaged and "D" stands for damaged, (b) shows specimen B3′ directly after impact

Figure 87 shows the full field DIC results of specimen B3′ which was subjected to a higher centered impact energy of 6 J. The force vs out-of-plane displacement curves in Figure 87(a) show no noticeable reduction in stiffness of the specimen before and after the impact of 6 J. The force vs von Mises strain curves in Figure 87(a) show a change in maximum strain of the specimen after the impact. The impact energy of 6 J caused enough damage which could be detected using full field DIC. The force vs von Mises strain curves show a more compliant specimen after the impact for all repeated tests.

The von Mises strain values are in agreement for all tests well within the expected range of variance between tests (i.e. 0 - 2 % von Mises strain). The lack of distinction on the force vs out-of-plane displacement curves between the undamaged and damaged specimen may be due to the amount of flexibility of the composite. The deformation of the specimen shown in Figure 87(b) immediately after the impact was not permanent, but it was more significant than that of the specimen that was subjected to 3 J of impact energy. The specimen reverted back to its original shaped once it was unbolted.

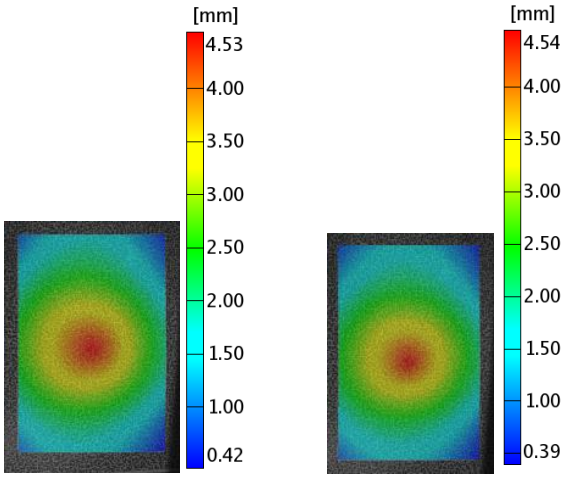

Figure 88: Out-of-plane displacement field of specimen B3′ for the final load of 427 N: (a) show the displacement field prior to 6 J of impact energy, (b) shows the displacement field after the impact energy of 6 J

Figure 88 shows the out-of-plane displacement fields of specimen B3′ before and after the impact of 6 J. A peak displacement of 4.53 mm is reported by specimen B3′ before the impact and 4.54 mm after the impact at the final load of 427 N, an insignificant difference to affirm the presence of damage. The displacement fields before and after the impact are also the same, circular around the center and becoming oval toward the free edges of the specimen. The displacement field in both cases is greatest at the center and decreases moving away from the location were the load was applied.

Figure 89 shows the von Mises strain fields of specimen B3′ before and after the impact of 6 J. The undamaged specimen sustained a peak von Mises strain of 1.182 % at a load of 427 N (Figure 89(a)). After the impact of 6 J the specimen exhibited a larger peak von Mises strain of 2.084 % at the same load (Figure 89(b)). The strain field in both cases is greatest at the location where the load was applied and decreases in intensity moving away from the center. Due to the damage the von Mises strain field is more concentrated around the center of the specimen where it was impacted. The barely visible impact damage resulted into a weaker composite as seen on the von Mises strain fields.

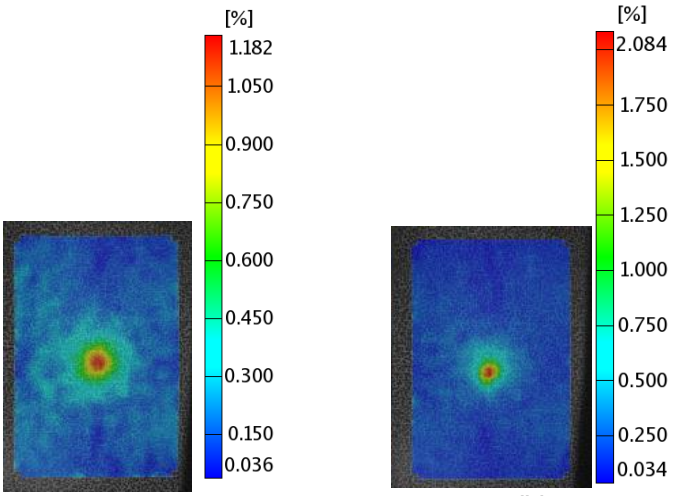

(a) (b)

Figure 89: von Mises strain fields of specimen B3′ for the final load of 427 N: (a) shows the strain field prior to 6 J of impact energy, (b) shows the strain field after the impact energy of 6 J

Figure 90(a) shows the force vs displacement curves and force vs von Mises strain curves of specimen A2 which was subjected to 9 J of centered impact energy. No noticeable difference exists on the force vs displacement curves between the undamaged and damaged A2 specimen. Figure 90(b) shows the deformation of specimen A2 immediately after the impact, the specimen reverted back to its original shape once removed from the base plate due to its flexibility. This shows no change in displacement values between the undamaged and damaged specimen with increasing loads.

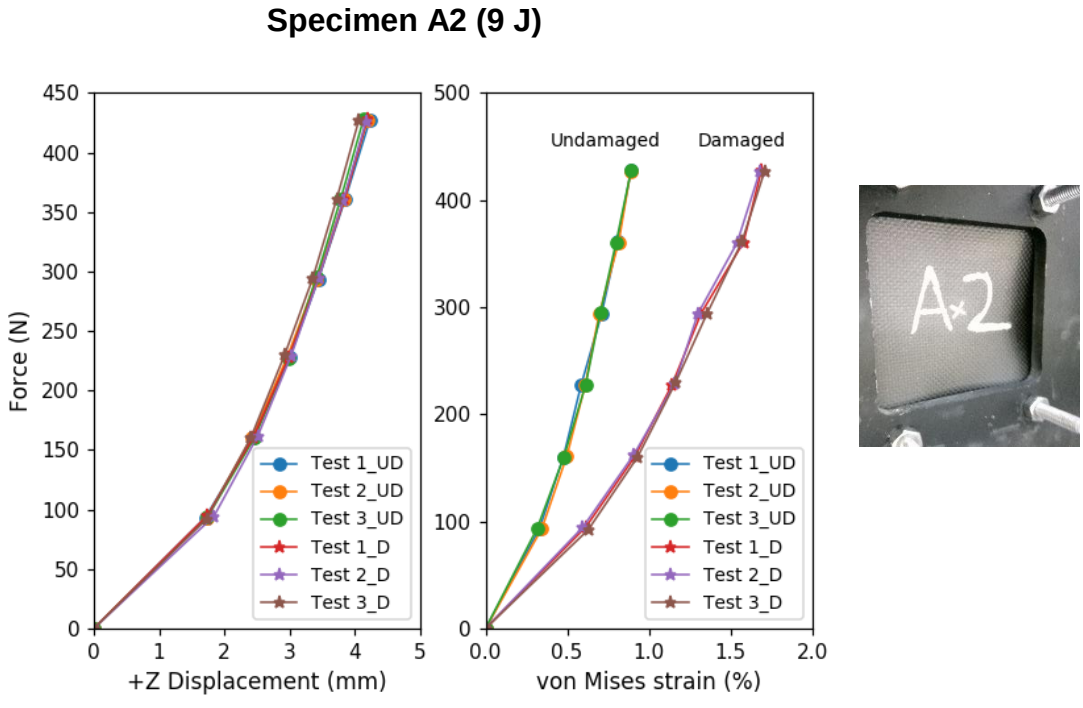

(a) (b)

Figure 90: Full field DIC results of specimen A2 which was subjected to 9 J of impact energy: (a) shows the force vs out-of-plane displacement curves and force vs von Mises strain curves, where "UD" stands for undamaged and "D" stands for damaged, (b) shows specimen A2 directly after impact

The presence of damage from the impact is evident on force vs von Mises curves, the difference in von Mises values increased with increasing load with no significant variation between repeated tests.

Figure 91 shows the von Mises strain field of specimen A2 prior and post the impact energy of 9 J. The strain field prior to the impact has a fairly circular shape close to the area where the load was applied (Figure 91(a)), the intensity of the field reduces moving away from the center. The field has an overall cross like shape which is a result of the constraints on the specimen (i.e. bolted at four corners). The shape of the strain field after impact is significantly different from that prior to the impact (Figure 91(b)), the field close to the center where the load was applied is no longer circular due the damage and the cross like shape in strain field has diminished due to the increased strain intensity at the center. The barely visible impact damage induced by an impact energy of 9 J was detectable from the force vs von Mises strain curves.

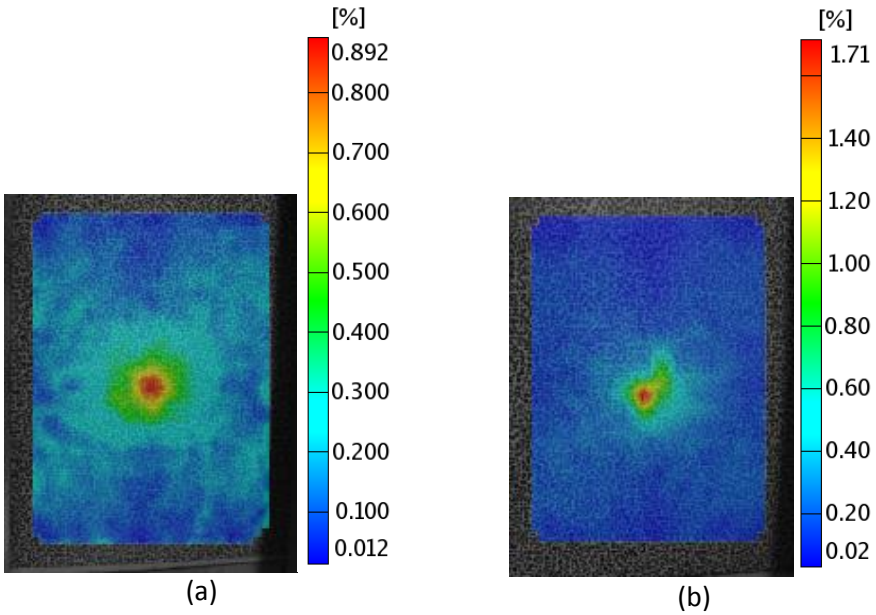

Figure 91: von Mises strain fields of specimen A2 for the final load of 427 N: (a) shows the strain field prior to 9 J of impact energy, (b) shows the strain field after the impact energy of 9 J

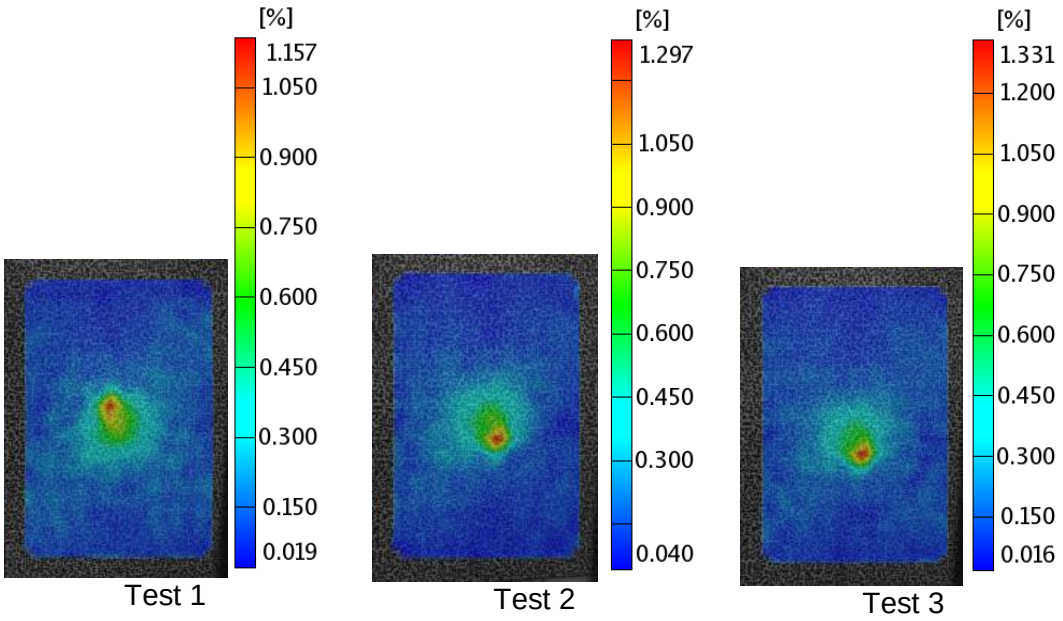

Figure 92: von Mises strain fields of three test of specimen B2 after 12 J of impact showing the load of 295 N applied at different points near the impacted area

Figure 92 shows the von Mises strain fields of three tests for the load of 295 N of specimen B2 which was subjected to 12 J of impact energy. The strain field are in agreement in terms of the shapes. Of interest in Figure 92 is that the peak strains occur at different location in the three tests where the point loads were applied. This demonstrates that so long as the load is applied near the impacted area (i.e. the center in this case) the loss in stiffness due to barely visible impact damage can still be detected.

5.5.3 Full field DIC of laminated composites subjected to off-centered impact

Figure 93 shows the force vs displacement curves and force vs von Mises strain curves of all the specimens that were subjected to off-center impact of various energies. All the test were conducted with the same trigger list of load for consistency. On the legend of the plots “UD” stands for undamaged and “D” stands for damaged.

The results show that apart from the established variation between tests there is no noticeable change on the force vs displacement curves and on the force vs von Mises strain curves for all off-center impact energies (i.e. 3 J, 6 J, 9 J, 12 J). The off-center impact points were marked at different locations on all the specimens and the loading was always applied at the center of the specimens. From the curves it is clear that full field DIC can detect barely visible impact damage only when the load is applied near the damage area.

Specimen B1 (3 J)

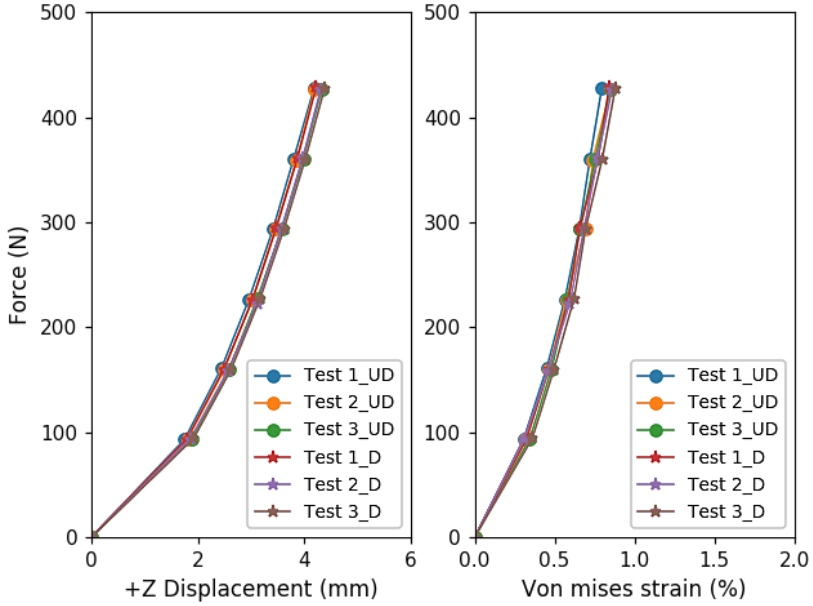

(a)

Specimen A4 (6 J)

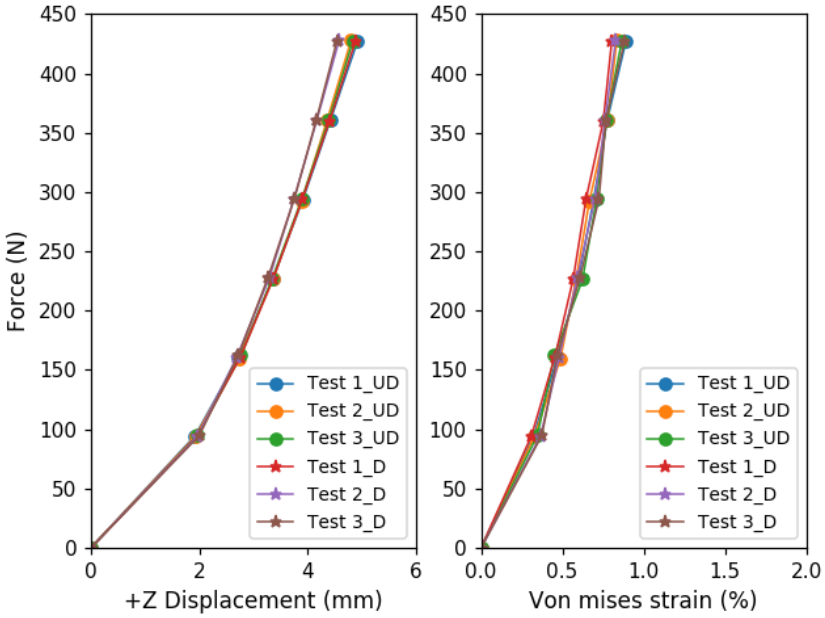

(b)

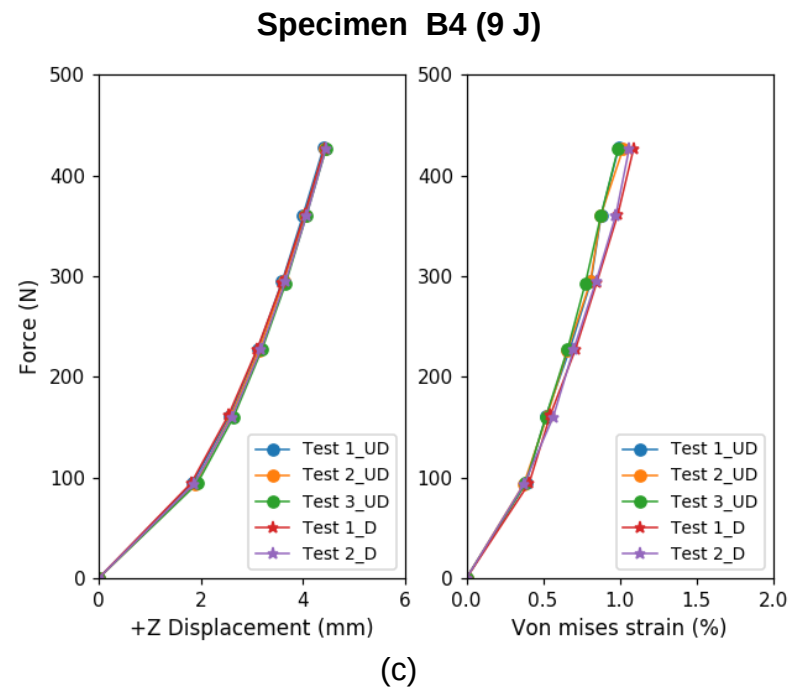

(c)

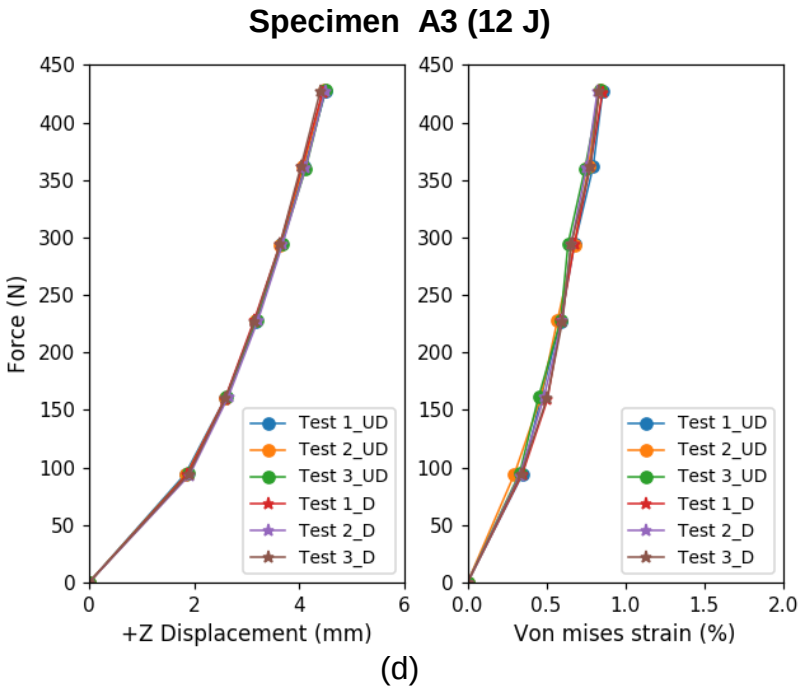

(d)

Figure 93: Full field DIC results of laminated composites subjected to off-center impact energies: (a) shows results of specimen B1 (3 J), (b) shows results of specimen A4 (6 J), (c) shows results of specimen B4 (9 J) and (d) shows results of specimen A3 (12 J). Where "UD" stands for undamaged and "D" stands for damaged

Chapter 6: Conclusions and recommendations

6.1 Conclusions

A review of the literature revealed how damage detection methods use the fact that defects in a composite material can interact with external stimuli applied to the material in order to excite it. This interaction tends to differ for different defects, depending on the type of excitation, some types of defects cannot be detected using certain methods. The applicability of the methods is governed by the type of damage mechanism and damage parameters such as size, depth and orientation.

This research evaluated modal analysis and full field DIC under static and dynamic loading as methods for detecting barely visible damage in laminated composites. The results from the various techniques revealed full field DIC under static loading conditions as the most suitable method for damage detection. The findings from the preliminary DIC investigation informed decisions implemented in the final investigation. The objective was to detect barely visible impact damage using full field DIC under static loading conditions (i.e. changes in out-of-plane displacements and von Mises strains caused by the damage).

The results showed that full field DIC under static loading conditions can be used to detect barely visible impact damage caused by energies larger than 3 J. The change in von Mises strain as a result of the damage becomes more prominent with increasing load. It was observed from the results, that in order to detect the damage the load has to be applied near the damage area. The results revealed that the deformation data is influenced by the constraints applied to the composite. The presence of damage causes the shape of the von Mises strain field to change near the impacted area.

Deformation data captured using full field DIC has often been used as a validation method for finite element analysis results. This research used full field DIC deformation data in a different manner which is based on the fact that damage of any kind on any component affect the stiffness of the part and reduces its ability to carry load under different loading conditions.

The work presented here can contribute to non-destructive testing in laminated composites. From most NDT methods the damage parameters such as shape, size and depth can be obtained. In cases where the damage parameters are of no consequence, the damage inspection method presented in this research can be beneficial by detecting the damage as loss of strength when the material is subjected to external loading.

6.2 Future work and recommendations

The use of full field DIC for damage detection of laminated composites under dynamic loading in section 4.4 could be improved by implementing instruments to measure the impact loading and force history, this could give more physical insight regarding the dynamic response of the composites in addition to the dynamic results in section 4.5 which show no change in peak deflection between the undamaged and damaged composites. The duration of the dynamic experiment lasted 3 seconds, a frame rate of 1500 fps used for the experiment may have missed stages of the actual maximum displacements upon the initial impact and the rebound as

shown in section 4.5, cameras with a higher frame rate of over 10000 fps could be used to capture the dynamic response in order to minimize the chance of missing the actual maximum out-of-plane displacements upon impact.

The use of full field DIC under static loading condition has proved suitable as a damage detection method for laminated composites by examining deformation data. It may be interesting to investigate whether full field DIC under static loading conditions can be used to detect the presence of cracks in laminated composite after sustaining impact forces.

References

Aramis. (2009). User Manual-Software.

Baker, A., Dutton, S., Kelly, D. (2004). *Composite Materials for Aircraft Structures*. *2nd edition*. Virginia: AIAA

Banks, H.T., Emeric, P.R. (1998). Detection of non-symmetrical damage in smart plate-like structures. *NASA/CR-1998-206931*

Carlsson, L., Adams, D., Byron, P. (2013). Basic Experimental Characterization of Polymer Matrix Composite Materials*. Polymer Reviews. 53*

Chang, C.Y., Chen, L.C., Lee, W.C., Ma, C.C. (2015). Measuring Full-Field Deformation and Vibration Using Digital Image Correlation. *Smart science*

Chen, F., Chen, X., Xie, X., Feng, X., Yang, L. (2013). Full field 3D measurement using multi-camera digital image correlation system. *Optics and Lasers in Engineering* **51** (2013) 1044–1052

Chrysafi. A.P., Athanasopoulos, N., Siakavellas, N.J. (2017). Damage detection on composite materials with active thermography and digital image processing. *International Journal of Thermal Sciences* **116** (2017) 242-253

Crall, M.D., Laney, S.G., Keller, M.W. (2019). Multimodal Damage Detection in Self-Sensing Fiber Reinforced Composites. *Advanced Functional Materials. 2019, 29, 1806634*

Crystal instruments manual. (2017). Basics of Modal Testing and Analysis.

Derenyi, E.E. (1996). Phogrammetry: the concepts. *Department of Geodesy and Geomatics Engineering*

Faria, A.W., Silve, R.A., Koroishi, E.H. (2017). Matrix Damage Detection in Laminated Composite Structures by Discrete and Continuous Wavelet Transforms Using Vibration Modes. *Journal of Aerospace Technology and Management. São José dos Campos, Vol.9, No 4, pp.431-441*

Foulk, J.A., Chao, Y.C., Akin, D.E., Dodd, R.B., Layton, P.A. (2006). Analysis of Flax and Cotton Fiber Fabric Blends and Recycled Polyethylene Composites. *Journal of Polymers and the Environment, Vol. 14, No. 1*

Gadhe, S.S., Navthar, R.R., (2016). Digital Image Correlation Technique for Strain Measurement of Aluminium Plate. *International Journal of Engineering Trends and Technology: 2231-5381*

Garney, G. (2006). *Defects found through non-destructive testing methods of fiber reinforced polymeric composites*. California State University: Fullerton

Ghobadi, A. (2017). Common types of damage in composites and their inspection. *World Journal of Mechanics* **7** (2017) 24-33

Gholizadeh, S. (2016). A review of non-destructive testing methods of composite materials. *Procedia Structural Integrity* **1** (2016) 050–057

Harris, B. (2003). *Fatigue in Composites. Science and Technology of the Fatigue Response of Fibre-Reinforced Plastics*. Woodhead Publishing: Sawston.

Image system motion analysis. (2016). TEMA DIC user guide.

Jareteg, C., Wärmefjord, K., Cromvik, C.,Söderberg, R., Lindkvist, L.,Carlson, J., Larsson, S., Edelvik, F. (2014). Geometry Assurance Integrating Process Variation with Simulation of Spring-In for Composite Parts and Assemblies. *Journal of Computing and Information Science in Engineering*

Jollivet, T., Peyrac, C., Lefebvre, F. (2013). Damage of composite material. *Procedia Engineering,* **66** (2013) 746-758

Kapadia, A. (2007). *Best practice guide Non Destructive Testing of composite materials.* National Composite Network

Kersemans, M., Verboven, E., Segers, J., Hedayatrasa, S., Van Paepegem, W. (2018). Non-Destructive Testing of Composites by Ultrasound, Local Defect Resonance and Thermography. *Proceedings* 2018, *2*, 554

Kessler, S.S., Spearing, S.M., Atalla, M.J., Cesnik, C.E.S., Soutis, C. (2002). Damage detection in composite materials using frequency response methods. *Composites: Part B* **33** (2002) 87-9

Lee, S.M. (1989). *Dictionary of Composite Material Technology.* Western hemisphere: Technomic Publishing Company incorporated

Li, W., Matthews, C.C., Yang, K., Odarczenko, M.T., White, S.R., Sottos, N.R. (2016). Autonomous Indication of Mechanical Damage in Polymeric Coatings. *Advanced Materials* **28** (2016) 2189–2194

Linder, W. (2003).*Digital photogrammetry theory and application.* New York: Springer

Lion precision. Eddy current displacement sensors, viewed 26 April 2019 <*http://www.lionprecision.com/eddy-current-sensors*>

Malhotra, A., Guild, F.J. (2014). Impact Damage to Composite Laminates: Effects of impact location. *Applied Composite Materials* **21** (2014) 165–177

Manes, A., Nunes, S., González-Jiménez, A., Amico, S., Giglio, M. (2018). Comparison of Non-Destructive Techniques for Impact Damage Area Assessment in Aramid/Epoxy Composites. *Proceedings* 2018, *2*, 437

Matthews, F.L., Rawlings, R.D. (1999).*Composite materials: Engineering and science*. New York: CRC press

Mehdikhani, M., Gorbatikh, L., Verpoest, I., Lomov, S. V. (2019). Voids in fiber-reinforced polymer composites: A review on their formation, characteristics, and effects on mechanical performance. *Journal of Composite Materials* **53** (2019) 1579–1669

Meirovitch, L. (1986). *Elements of vibration analysis*. *2nd ed*. New York: McGraw-Hill

Meyendorf, N.G.H., Nagy, P.B., Rokhlin, S. (2013). *Nondestructive Materials Characterization: With Applications to Aerospace Materials*: Springer Berlin Heidelberg.

Movahedi-Rad, A., Keller, T., Vassilopoulos, A.P. (2018). Effect of loading pattern on fatigue behaviour of laminated composites. *Multidisciplinary Digital Publishing Institute*

Murat, B.I.S., Rahman, A.A.A. (2017). Study of Impact Damage Behaviour in Woven Carbon Fiber Plates. *Procedia Engineering* **170** (2017) 47–54

Namala, K.K., Mahajan, P., Bhatnagar, N. (2014). Digital Image Correlation of Low-Velocity Impact on a Glass/Epoxy Composite. *International Journal for Computational Methods in Engineering Science and Mechanics* **15** (2014) 203–217

Park, J.H., Hwang, J.H., Lee, C.S., Hwang, W. (2001). Stacking sequence design of composite laminates for maximum strength using genetic algorithms. *Composite Structures, Volume 52, Issue 2, 2001, Pages 217-231*

Poggio, G.F., Poggio, T. (1984). The analysis of stereopsis. *Annual Review of Neuroscience* **7** (1984) 379-412

Prinsloo, T. (2011*).Damage Detection Methodology for Composite UAV Wings using Modal analysis and Probabilistic Concepts.* M (Eng). University of Pretoria

Rauter, N., Lammering, R. (2015). Impact Damage Detection in Composite Structures Considering Nonlinear Lamb Wave Propagation. *Mechanics of Advanced Materials and Structures, 22:1-2, 44-51*

Reifsnider. K.L., Talug. A. (1980). Analysis of fatigue damage in composite laminates. *International journal of fatique*

Revuelta. D., Miravete. A. (2002). Fatigue damage in composite materials. *International Applied Mechanics, Vol. 38, No. 2, 2002*

Sanchez-Saez, S., Barbero, E., Zaera, R., Navarro, C. (2005). Compression after impact of thin composite laminates*. Composites Science and Technology* **65** (2005) 1911–1919

Schenk, T. (2005).Introduction to photogrammetry. *Department of Civil and Environmental Engineering and Geodetic Science*

Shabeer, K.P., Murtaza, M. A. (2013). Optimization of Aircraft Wing with Composite Material. *International Journal of Innovative Research in Science, Engineering and Technology, vol. 2, no. 6, pp. 2471-2477.*

Siow, Y.P., Shim, V.P.W. (1997). An Experimental Study of Low Velocity Impact Damage in Woven Fibre Composites. *Journal of Composite Materials, vol. 32, no. 12, pp. 1178–1202, 1998.*

Spiegel, M.D. (2014). *Damage detection in composite materials using lead zirconate titanate.* (Msc). University of Alabama

Thionnet, A., Renard, J. (1994). Laminated composites under fatigue loading: a damage development law for transverse cracking. *Composites Science and Technology* **52** (1994) 173-181

Tuo, H., Lu, Z., Ma, X., Xing, J., Zhang, C. (2019). Damage and failure mechanism of thin composite laminates under low-velocity impact and compression-after-impact loading conditions. *Composites Part B* **163** (2019) 642–654

Vaziri, R., Quan, X., Olson, M.D. (1996). Impact analysis of laminated composite plates and shells by super finite elements. *International Journal of Impact Engineering,* Vol. 18, Nos 7-8, pp. 765-782

Wang, R., Zeng, S., Zheng, Y. *Polymer matrix composite and technology*. WoodHead publishing

Wen, J., Choy, F.K., Xia, Z. (2013). Wavelet Denoising in Electrical Resistance Based Damage Detection of Carbon Fiber Composite Materials*. Journal of Materials Science Research;Vol. 2, No. 1; 2013*

Won Nam, K., Park, j., Kim, I-Y., Kim, k-G. (2012). Application of Stereo-Imaging Technology to Medical Field. *Healthcare Informatics Research* **18** (2012):158-163

Appendices

The appendices show the out-of-plane displacements and von Mises strain fields of all the loads before and after the impact for all three tests of each specimen that was subjected to centered impact. The appendices can viewed on the google drive link:

https://drive.google.com/file/d/1f5YvCSfwXfXT2EurajSW1icMGj8HPKDS/view?usp=sharing